

Electronic Thesis and Dissertation Repository

3-24-2020 10:00 AM

Source Parameters of Induced Seismicity in North America

Joanna M. Holmgren
The University of Western Ontario

Supervisor
Atkinson, Gail M.
The University of Western Ontario
Ghofrani, Hadi
The University of Western Ontario

Graduate Program in Geophysics
A thesis submitted in partial fulfillment of the requirements for the degree in Doctor of
Philosophy
© Joanna M. Holmgren 2020

Follow this and additional works at: <https://ir.lib.uwo.ca/etd>



Part of the [Geophysics and Seismology Commons](#)

Recommended Citation

Holmgren, Joanna M., "Source Parameters of Induced Seismicity in North America" (2020). *Electronic Thesis and Dissertation Repository*. 6859.
<https://ir.lib.uwo.ca/etd/6859>

This Dissertation/Thesis is brought to you for free and open access by Scholarship@Western. It has been accepted for inclusion in Electronic Thesis and Dissertation Repository by an authorized administrator of Scholarship@Western. For more information, please contact wlsadmin@uwo.ca.

Abstract

Source parameters of earthquakes play a key role in the understanding of earthquake behavior and modelling of seismic hazard. They describe the size of earthquakes, including how much energy is generated during the rupture, and how the ground motion is distributed over different frequency bands and azimuths. The last decade's increase in induced seismicity caused by oil and gas production has led to an interest in understanding the underlying earthquake processes and how they can be modelled. This thesis is divided into three studies, each examining source parameters of induced earthquakes in North America.

In the first study, I show that for earthquakes in Central US the variability of ground-motion prediction equations (GMPEs), known as sigma, can be reduced by adjusting the basic input source parameters of location and magnitude. Sigma is an important seismic hazard parameter because it exerts significant control over the expected ground motions at return periods used in seismic design. Refinements in magnitude were shown to reduce sigma more than refinements in location. This reflects that between-event variability is not completely accounted for by magnitude in the GMPE, as it is also influenced by other source parameters such as stress drop.

In the second study, I examine stress drop and corner frequency in the Western Canada Sedimentary Basin (WCSB) using the Empirical Green's Function (EGF) method. Large azimuthal variations are found in the corner frequencies for earthquakes, which indicates rupture directivity, a phenomenon which can have implications for observed high-frequency ground motion. By modelling the directivity using a Haskell (1964) model, earthquake corner frequencies are retrieved despite the region's sparse seismic network.

Finally, in the third study, I show that the stress drops obtained from the previous WCSB EGF study can be used as proxies for the GMPE "stress parameter". I also test whether they provide equivalent measures of the high-frequency content of the earthquake source. I find that GMPE stress parameters tend to yield lower corner frequency values in the forward

rupture directivity direction when comparing individual earthquake records. This can be partly attributed to the trade-off between source and site effects in GMPE modeling.

Keywords

Induced seismicity, earthquake source parameters, stress drop, stress parameter, ground motion prediction equation, engineering seismology.

Summary for Lay Audience

The last decade has seen an increase in man-made earthquakes, referred to as induced seismicity, due to developments within the oil and gas industries (e.g., Rubinstein and Mahani, 2015; Atkinson et al., 2016). This has led to an increase in earthquake hazard in regions such as the Western Canada Sedimentary Basin (WCSB) in Canada and the Central US (Oklahoma, Texas). A key question for assessing the hazard is whether these induced earthquakes behave in the same way as natural earthquakes, and if they can be modelled using the same assumptions. This thesis takes a closer look at earthquake source parameters of induced seismicity in order to increase the knowledge of the underlying processes.

The thesis is divided into three parts, where the first part examines how the variability of ground-motion prediction equations (GMPEs) are affected by small changes in the source parameters magnitude and location. GMPEs are used by engineering seismologists to describe the expected ground motion levels in a region, and the variability of GMPEs will tell the user how much uncertainty there is around the expected level. The smaller the variability, the more precise are the estimations. The second part of the thesis focuses on one source parameter which determines the high-frequency content of ground motion. High-frequency ground motion is important to most types of ordinary structures, so understanding how the high-frequency content from induced earthquakes differs from that of natural earthquakes is key to assessing the hazard. Finally, the last part looks at the high-frequency ground motions using two different methods that are commonly used within the field of seismology, to see whether alternative methods give us the same information.

Co-Authorship Statement

The materials present in Chapters 2, 3, and 4 of this thesis have been previously published or submitted for publication to the peer-reviewed journals of *Seismological Research Letters* and *Bulletin of Seismological Society of America*. This thesis contains only the original results of research conducted by the candidate under supervision of Dr. Gail Atkinson and Dr. Hadi Ghofrani. The original contributions are summarized as follows:

Development of a zero-biased ground-motion prediction equation (GMPE) for Central US based on the Atkinson (2015) GMPE; Determination of sigma and its components from GMPE residuals; Compilation and data processing of time-series for selected earthquakes in Western Canada Sedimentary Basin (WCSB); Compilation of seismological parameters as well as peak ground motions and response spectral amplitudes (FAS and PSA) for earthquakes in WCSB; Determination of corner frequencies and stress drop for earthquakes in WCSB using the Empirical Green's Function (EGF) approach; Determination of directivity parameters for earthquakes in WCSB; Determination of a stress model for WCSB; Development of a regional-specific GMPE for WCSB; Determination of stress parameter for earthquakes in WCSB; Comparison between stress drops and stress parameters in WCSB.

Dr. Karen Assatourians and Dr. Mark Novakovic compiled the ground-motion database used in Chapter 2. Dr. Novakovic also produced the attenuation and geometric spreading terms (F_γ and F_Z) for the GMPE developed in Chapter 4 (Novakovic et al., 2019).

Dr. Atkinson is the co-author to all three articles presented in this thesis (Chapters 2, 3, and 4).

Dr. Ghofrani is the co-author of the articles in Chapters 3 and 4.

Acknowledgments

I would like to express my sincere gratitude to my supervisor Dr. Gail Atkinson for her continuous guidance and support during my PhD study. Her insightfulness, encouragement, and valuable expertise have been essential to finishing this thesis, and I am deeply grateful to how much I've grown as a researcher thanks to her during these four years in Canada.

I would also like extend my gratitude to my co-supervisor Dr. Hadi Ghofrani, whose constant support and expertise has seen me through many of the PhD hurdles. His attention to detail and extended knowledge has helped me think outside of the box several times.

I would like to thank my PhD thesis examiners Dr. David Eaton, Dr. Katsu Goda, Dr. Sheri Molnar, and Dr. Tim Newson for their helpful comments that have improved this thesis. I would also like to thank Dino Bindi, Rachel Abercrombie, Delphine Fitzenz, Thomas Pratt, and our other anonymous paper reviewers for their constructive feedback which helped improve the manuscripts presented as chapters in this thesis. I would like to extend my thanks to the Natural Science and Engineering Research Council of Canada, TransAlta, and Nanometrics, whose funding has made this work possible.

And last but not least, I would like to show my appreciation to my friends and family who have supported me throughout my PhD. Specifically to all the friends I've met during my stay in Canada, who have made this adventure a whole lot more eventful.

Table of Contents

Abstract	ii
Summary for Lay Audience	iv
Co-Authorship Statement.....	v
Acknowledgments.....	vi
Table of Contents	vii
List of Tables	x
List of Figures	xi
List of Appendices	xviii
List of Symbols	xix
Chapter 1	1
1 Introduction	1
1.1 Motivation of the study.....	1
1.2 Earthquake Source Parameters	3
1.2.1 Magnitude and Location	4
1.2.2 Stress Drop, $\Delta\sigma$	5
1.2.3 Rupture Directivity	8
1.3 Modelling Ground Motions	10
1.3.1 Fourier and Response Spectra.....	10
1.3.2 Brune Source Model	12
1.3.3 Ground-Motion Prediction Equations.....	14
1.4 Organization of Thesis	17
Chapter 2.....	19
2 Effect of Uncertainty in Source Parameters on Ground-Motion Variability for Potentially Induced Earthquakes in the Central United States.....	19
2.1 Introduction.....	19

2.2	CUS Ground-Motion Database.....	21
2.3	Zero-Biased GMPE.....	23
2.4	Ground-Motion Center.....	26
2.5	Results.....	27
2.6	Discussion and Conclusion.....	31
Chapter 3.....		36
3	Stress Drops and Directivity of Induced Earthquakes in Western Canada Sedimentary Basin.....	36
3.1	Introduction.....	36
3.2	Database for Study.....	38
3.3	Analysis Methods.....	39
3.3.1	Spectral Ratios.....	39
3.3.2	Directivity Analysis Based on Haskell Source Model.....	44
3.3.3	Moment Magnitude Computation.....	48
3.3.4	Stress-Drop Computation.....	49
3.4	Results.....	50
3.5	Discussion.....	58
3.6	Conclusion.....	66
Chapter 4.....		67
4	Reconciling Ground Motions and Stress Drops for Induced Earthquakes in the Western Canada Sedimentary Basin.....	67
4.1	Introduction.....	67
4.2	Database.....	70
4.3	Generic GMPE.....	72
4.4	Stress Parameter, $\Delta\sigma_{par}$	77
4.5	Results.....	79
4.5.1	GMPE Residuals and Directivity Effects.....	79

4.5.2 Stress Parameter vs Stress Drop Values	81
4.6 Discussion	83
4.7 Conclusion	87
Chapter 5.....	89
5 Conclusions and Future Studies.....	89
5.1 Summary and Conclusions	89
5.2 Suggestions for future study	93
Bibliography	94
Appendices.....	115
Electronic Supplement Description	120
Curriculum Vitae	122

List of Tables

Table 2.1. Coefficients of Equations (2.2) and (2.4) for each pseudospectral acceleration (PSA; 5% damped) frequency and peak ground acceleration (PGA) and peak ground velocity (PGV).	24
Table 3.1. Comparison between moment magnitudes obtained from displacement spectra and moment magnitudes from published moment tensor analyses.	57

List of Figures

Figure 1.1. Illustration of an earthquake’s source, path, and site components. The station (triangle) records the earthquake ground motions, providing a time series to be analyzed..... 3

Figure 1.2. A schematic illustration of rupture directivity and the resultant source pulses observed at different azimuths. The rupture initiation and rupture path are given as a star and arrow, respectively. The shaded grey area within the pulses signify the constant M_0 observed at all azimuths. 9

Figure 1.3. Comparison between Fourier amplitude spectrum (FAS) and pseudo-spectral acceleration (PSA). (Top) acceleration time series being analyzed. (Bottom, left) FAS of the time series. (Bottom, middle) SDOF transfer functions used in RVT to retrieve the response spectrum. (Bottom, right) response spectrum of the time series..... 11

Figure 1.4. Brune (solid black) and Boatwright (dashed black) source models plotted on top of an earthquake record’s displacement Fourier spectrum. The corner frequency and low-frequency level are emphasized in the figure. 13

Figure 1.5. Example of a GMPE (solid line) developed for M 3.2-3.4 earthquake records at PSA 5.0 Hz (circles) plotted against distance. (Left) The scatter from multiple earthquakes, with one earthquake highlighted (orange circles). (Right) Zoom-in on the highlighted earthquake’s records, visualizing the dB and dW terms..... 16

Figure 2.1. (Left) The stations (triangles) and earthquakes (circles; U.S. Geological Survey/Oklahoma Geological Survey [USGS/OGS] reported epicenters) used in this study to compute the zero-biased ground-motion prediction equation (GMPE) from the ground-motion database. The darker shaded stations and earthquakes are those used for the ground-motion center (GMC) sigma analysis. The size of circle scales with magnitude. The lighter shades vary between M 3.0 and 5.6, and the darker shades vary between M 3.0 and 4.3. (Right) Scatter plot of the data shown to the left, with the same shading. 22

Figure 2.2. (Top) Peak ground velocity (PGV) residuals for the vertical component plotted against hypocentral distance using (left) the Atkinson (2015; hereafter, A15) GMPE, (middle; A15 + D) a zero-biased GMPE, and (right; A15 + D + S) a zero-biased GMPE after removal

of stations terms. (Bottom) PGV residuals for the geometric mean of the horizontal components. 25

Figure 2.3. The total variability, between-event term, and within-event term for each iteration of the iterative grid search, for selected ground-motion parameters (pseudo-spectral acceleration [PSA] at 0.5, 1, 3.3, and 10 Hz, peak ground acceleration [PGA], and peak ground velocity [PGV]), for the vertical component, using all records within 70 km. The odd iterations are grid searches optimizing the locations, and the even iterations optimize the magnitudes. Iteration 4 is marked as the final iteration. 27

Figure 2.4. The total variability, between-event term, and within-event term for each iteration of the iterative grid search, for selected ground-motion parameters (PSA at 0.5, 1, 3.3, and 10 Hz, PGA, and PGV), for the vertical component, using only those records within a hypocentral distance of 10 km. The odd iterations are grid searches optimizing the locations, and the even iterations optimize the magnitudes. Iteration 4 is marked as the final iteration. 28

Figure 2.5. A histogram of the amount of change in (left) location and (middle) magnitude between the initial and optimized locations and magnitudes of the 38 study events. (Right) The change in magnitude and location for each event. 28

Figure 2.6. The initial (triangles) and final (circles) within-event residuals ϕ (top) and between-event residuals τ (bottom), for PGA (left) and PGV (right), for the vertical component. The data are divided into three bins, with the mean and standard deviation of each bin shown. 30

Figure 2.7. Left: Comparison between the initial (dashed lines) and final (solid lines) variabilities for total variability (circles), between-event (squares), and within-event (triangles) terms, for four PSA frequencies (0.5, 1.0, 3.3, and 10 Hz), PGA, PGV, along with the average for the six ground-motion parameters, considering all records within 70 km. (Top) Vertical component and (lower) geometric mean of horizontal components. Right: Same but considering only those records within a hypocentral distance of 10 km. 32

Figure 2.8. Comparison between the recorded PSA values for a single event versus distance for the initial locations (triangles) and the final locations (large circles), along with the zero-

biased GMPE, plotted using the initial M (dashed line) and the final M (solid line). The small circles display the final position of the data points if we also optimize the depth of the event.
 33

Figure 2.9. A comparison between the final GMC magnitude (moment magnitude) and the catalog magnitudes reported by USGS/OGS..... 34

Figure 3.1. Overview map of the Western Canada sedimentary basin (WCSB) and its two main formations Duvernay and Montney. The 87 target earthquakes (circles) between April 2014 and March 2019 and stations (triangles) are shown..... 38

Figure 3.2. Empirical Green’s Function (EGF) method outlined using target earthquake 69 and one of its EGF earthquakes as an example. (a) Waveform time series of the target (light line) and EGF (dark line) used in the cross correlation (corr). The bold line shows the 10 second time window used. A high-pass (hp) filter is applied to the top two seismograms with a corner of 0.8 Hz, and a band-pass (bp) filter with corners 1.0 and 2.0 Hz is applied to the seismograms before cross correlation. (b) Raw displacement spectra (S window) of the target and EGF. The bold horizontal line and the bold spectra lines represent frequency range over which signal-to-noise ratio (SNR) > 3. (c) Spectral ratio between the target and EGF, with the best-fit model plotted on top (dashed line); target and EGF corner frequencies are shown as vertical dashed lines. (d) Variance check of the best-fit model. (e) Relative source time function (RSTF) from deconvolution of the target from the EGF 41

Figure 3.3. A comparison of azimuthal variability of corner frequency between two target earthquakes. Each station mean is shown as a circle, with vertical error bars representing the corner-frequency uncertainty. Darker shaded circles are stations with more records. Event 81 shows no clear azimuthal variation in the station corner frequencies (circles) and was assigned a directivity index = 2. Event 83 displayed a factor of five difference between the largest and smallest corner frequencies, and was assigned a directivity index = 1..... 46

Figure 3.4. Overview of the directivity evaluation process (event 29). (a) After the station corner frequencies are converted to source rupture durations (circles), a best-fit Haskell model is determined. The horizontal line shows the true source duration. (b) Similar plot as (a), but now in terms of corner frequency. The horizontal line shows the rupture corner frequency, with

the uncertainty indicated by the width of a lighter shaded line behind. (c) Bootstrap analysis, with plus or minus standard deviation shown as two vertical, solid lines. (d) A polar plot of the station corner frequencies (circles), model (dashed line), and model rupture azimuth (solid line). 47

Figure 3.5. Corner-frequency results for target events with directivity index of (a) 0, (b) 1, and (c) 2. The complex targets are highlighted using a black circle. Error bars representing the standard error of the mean are shown as horizontal lines for each marker. Constant stress-drop lines outline 100, 10, 1, and 0.1 MPa, from top to bottom, computed using the Madariaga (1976) k -value and $\beta = 3200 \text{ m}\cdot\text{s}^{-1}$. Small circles in background show results from the Wu et al. (2018) study for comparison. 51

Figure 3.6. Example of a unilateral rupture earthquake (event 107). (a) Normalized RSTF and (b) normalized spectral ratios are shown varying with station azimuth. The azimuths are binned by intervals of 20° . The top stack shows all the individual records stacked. The average over each azimuthal interval is shown as a dark line with its standard error width indicated by a lighter shaded line behind. Dashed black lines are the fitted spectral ratios, with the resultant corner frequencies displayed on the right. 52

Figure 3.7. Example of a complex rupture earthquake (event 87), with the same figure description as Figure 3.6. 53

Figure 3.8. Spatial distribution of target earthquakes with observable rupture directivity (circles). The complex directivity events have darker shading. The rupture azimuth for each target is displayed as a solid line extending from the circle. (b) Zoom-in of the Fox Creek area, shown with a dashed rectangle in (a). (c) Double-couple nodal planes from Wang et al. (2018) for nine target earthquakes, along with the station azimuths (triangles surrounding the focal mechanisms). The rupture azimuths obtained in this study are shown with thicker solid lines; darker shading indicates complexity. All earthquakes involved primarily strike-slip faulting, except for event 4, which has thrust-fault focal mechanisms. 55

Figure 3.9. Stress-drop values versus moment magnitude. Circles are events with unknown directivity due to data sparseness or too much variability; squares are events with observed directivity; diamonds are events with no observed directivity. The complex targets are

highlighted with black circles. The Madariaga (1976) k -value and $\beta = 3200 \text{ m}\cdot\text{s}^{-1}$ are used for all earthquakes. Dashed line shows the stress parameter value obtained by Novakovic et al. (2018) for induced earthquakes in Oklahoma based on regression of ground-motion data, after converting their corner frequencies to this study’s model constants. 56

Figure 3.10. Target earthquake (event 51) with large stress drop of 370 MPa. (a) Corner frequency plotted against station azimuth with vertical error bars. Circles are darker if there are more EGF earthquakes for that station. (b) Normalized RSTFs and (c) spectral ratios are shown varying with station azimuth binned by intervals of 20° . Dashed black lines are the fitted spectral ratios, with the resultant corner frequencies displayed on the right. (d) Polar plot of the station coverage with distance, with the target earthquake as a star and the stations as triangles. The colors are the same as in (a), and the number of EGF earthquakes are given in the triangles. 62

Figure 3.11. The November 2018 Fort St. John earthquake (event 112). (a) Normalized RSTFs and (b) spectral ratios are shown varying with station azimuth. The azimuths are binned by intervals of 20° . The top stack shows all the individual records stacked. The average over each azimuthal interval is shown as a dark line with its standard error width indicated by a lighter shaded line behind. Dashed black lines are the fitted spectral ratios, with the resultant corner frequencies displayed on the right. 65

Figure 4.1. Database of study earthquakes and records. (a) Map of stations (triangles) and study earthquakes (light circles); those with resolvable directivity are shown as dark circles. Shaded region is the Western Canada Sedimentary Basin. (b) Record distribution by moment magnitude and distance. 71

Figure 4.2. Input stress parameter model $\Delta\sigma_{model}$ (dashed line) compared to the WCSB stress drop values from the EGF study of Holmgren et al. (2019) (circles). 73

Figure 4.3. (a) Anelastic attenuation coefficient values γ (solid grey line) and the proposed smoothed model (dashed black line) for the Western Canada Sedimentary Basin (WCSB), in comparison to γ values from Oklahoma (dark dotted) (Novakovic et al., 2018), Central Eastern North America (CENA, medium dotted) (Yenier et al., 2015b), and California (light dotted)

(Yenier et al., 2015b). (b) Quality factor as determined from γ using Equation (4.3) (same models); equation for the WCSB Q model is given. 74

Figure 4.4. Western Canada Sedimentary Basin (WCSB) quality factor (black solid line) compared to Q -values in literature for different regions: CP86 – Chávez and Priestley (1986), Great Basin USA; GM87 – Gupta and McLaughlin (1987), eastern US; AM92 – Atkinson and Mereu (1992), southeastern Canada; A04 – Atkinson (2004), eastern North America; BS11 – Boatwright and Seekins (2011), southeastern Canada; YA15a –Yenier and Atkinson (2015a), California; YA15b – Yenier and Atkinson (2015b), central-eastern North America. 75

Figure 4.5. Calibration factor (C , heavy black line) and individual station terms (FS , light lines) for the 50 stations in this study. The average all of the individual station terms (heavy grey line) is constrained to zero by definition and thus the calibration factor contains any average regional site response. The average posthole and station terms are shown in dark and light dashed lines, respectively. 76

Figure 4.6. Examples of fitting the GMPE (light solid line) to observed data (dark solid line) at Station SNUFA for two specific events (details shown in figure panels). The numbers in brackets show error range on parameters. 78

Figure 4.7. Final residuals for the WCSB GMPE for four oscillator frequencies: (a) 0.5 Hz; (b) 1.0 Hz; (c) 5.0 Hz; and (d) 10.0 Hz. The residuals are shaded based on magnitude, where darker circles are higher magnitude events. Squares show mean residuals and their standard deviation in log-spaced distance bins. 80

Figure 4.8. Within-event residuals (circles) for the 39 earthquakes with resolvable directivity effects. The residuals are sorted and plotted versus the relative angle with respect to the rupture direction, where 0° records are from stations in the forward rupture direction and 180° records are from stations in the backwards direction. Four oscillator frequencies are plotted: (a) 1.0 Hz, (b) 5.0 Hz, (c) 10.0 Hz, and (d) 20.0 Hz. The mean and standard deviations in azimuth bins are plotted as black squares and vertical horizontal bars. 81

Figure 4.9. (a) Earthquake stress parameters plotted against moment magnitude (circles). The EGF stress drops from Holmgren et al. (2019) are also shown (squares), along with the stress

model for WCSB GMPE ($\Delta\sigma$ model). (b) Ratios between EGF stress drops and GMPE stress parameters plotted against moment magnitude. (c) Ratios between $\Delta\sigma$ model and the event-specific GMPE stress parameters plotted against moment magnitude. All stress measures have been converted into bars and are defined using the Brune k -model..... 82

Figure 4.10. (a) Corner frequencies obtained through GMPE inversion (circles) and through the EGF method (squares), plotted against magnitude. Constant stress drop/parameter lines using Equation (4.6) are shown. Note that the values of the stress drop lines depend heavily on the convention used to link corner frequency to stress drop, as described in the text. (b) Ratios between the EGF and GMPE corner frequencies. 82

Figure 4.11. Comparison of f_c by record between the EGF method and the GMPE method. (a) Schematic view of the three schematic azimuth quadrants w.r.t. horizontal rupture direction: records within $0^\circ \pm 45^\circ$ are in the forward direction; records within $180^\circ \pm 45^\circ$ are in the backward direction; and remaining records are in the neutral direction. (b) Ratios of EGF f_c to GMPE f_c (circles) plotted as a function of horizontal angle away from rupture direction, shaded based on quadrant from (a). Histograms showing the ratio distributions can be seen on the right. 85

List of Appendices

Table A2.1. Initial and final variability terms for each PSA (5% damped) frequency and peak ground acceleration (PGA) and peak ground velocity (PGV), for all records within 70 and 10 km, for the vertical component.

Table A2.2. Initial and final variability terms for each PSA (5% damped) frequency and peak ground acceleration (PGA) and peak ground velocity (PGV), for all records within 70 and 10 km, for the geometric mean of the horizontal components.

Figure A3.1. Magnitude computation example of target event #114 **M** 3.81 2018-11-30 02:15:01 and four of its stations within 100 km. The left column shows HHE components, and the right shows HHN components. Signal (solid line), noise (light dashed line), and low-frequency best fit of Equation (3.5) (dark dashed line) are shown for each station and component. The bold spectra lines represent frequency range over which $SNR > 3$.

Table A4.1. The generic GMPE components.

List of Symbols

β	S-wave velocity ($\text{m}\cdot\text{s}^{-1}$ or $\text{km}\cdot\text{s}^{-1}$).
γ	Sharpness constant in the Brune (1970) and Boatwright (1980) models, where $\gamma_{Brune} = 1$ and $\gamma_{Boatwright} = 2$.
κ	Kappa, high-frequency attenuation parameter (s).
ρ	Density at the source ($\text{g}\cdot\text{cm}^{-3}$).
σ	Sigma, representing the total aleatory variability of GMPEs.
$\Delta\sigma_{drop}$	Stress drop (bars or MPa), a high-frequency source parameter determined using a Brune source model in the Fourier domain.
$\Delta\sigma_{par}$	Stress parameter (bars or MPa), a high-frequency source parameter determine using a GMPE in the response domain.
τ	Between-event or inter-event term of σ , describing the earthquake-to-earthquake variability of GMPEs.
Ω_0	Low-frequency plateau in the Brune (1970) source model ($\text{cm}\cdot\text{s}$).
μ	Shear modulus (Pa).
ϕ	Within-event or intra-event term of σ , describing the record-to-record variability of GMPEs.
A	Earthquake fault area (m^2).
C	GMPE Calibration factor.
CC	Cross-correlation coefficient.

CUS	Central United States, covering Oklahoma, Texas, Arkansas, and Kansas. It is the center of the US petroleum exploration from the Anadarko basin (e.g., Higley et al., 2011).
\bar{D}	Average earthquake slip (m)
EGF	Empirical Green's Function.
f	Frequency in Hertz (Hz).
f_c	Corner frequency from the Brune source spectrum (Hz).
f_0	Natural frequency of an oscillator (Hz).
GMC	Ground-motion center, the location and magnitude that results in the smallest residuals between observed ground motions and a GMPE.
GMPE	Ground-motion prediction equation, also known as ground motion model (GMM).
h_{eff}	Effective depth parameter used in the GMPE (km or m).
k	Constant relating the rupture radius r and the corner frequency f_c (e.g. Brune, 1970; Sato and Hirasawa, 1973; Madariaga, 1976)
R_{eff}	Effective point-source distance used in the GMPE (km or m).
R_{hypo}	Hypocentral distance, the distance from the rupture's focal point to the site (km or m).
r	Rupture radius (m or km)
M	Moment magnitude, based on seismic moment M_0 (Kanamori and Hanks, 1979).

M_0	Seismic moment, a measure of the size of an earthquake and related to its fault area and average slip. Measured in dyne·cm or N·m, where dyne·cm = 10^{-7} N·m.
PGV	Peak ground velocity ($\text{m}\cdot\text{s}^{-1}$ or $\text{cm}\cdot\text{s}^{-1}$) of the velocity time series.
PGA	Peak ground acceleration ($\text{m}\cdot\text{s}^{-2}$ or $\text{cm}\cdot\text{s}^{-2}$) of the acceleration time series.
PSA	Pseudo-spectral acceleration ($\text{m}\cdot\text{s}^{-2}$ or $\text{cm}\cdot\text{s}^{-2}$), defined as the maximum displacement $\times (2\pi f_0)^2$ of a single-degree-of-freedom oscillator of a specific natural frequency and damping.
$Q(f)$	Frequency dependent Quality factor.
S-wave	Shear waves generated by earthquakes.
SNR	Signal-to-noise ratio between a time series' earthquake signal and
WCSB	Western Canada Sedimentary Basin, a region in Alberta and north-western British Columbia in Canada. The basin consists of a simple northeasterly tapering wedge of sedimentary rocks more than 6 km thick, extending southwest from the Canadian Shield into the Cordilleran foreland thrust belt (Porter et al., 1982). It is the center of Canada's petroleum exploration and production (Rivard et al., 2014).
Y	Ground-motion intensity measure used in a GMPE. Usually taken as $\log_{10}(Y)$ or $\ln(Y)$.

Chapter 1

1 Introduction

1.1 Motivation of the study

Earthquakes caused by oil and gas production have been of much scientific interest over the last decade. Although the process of hydraulic fracturing has been in use since the late 1940s, the introduction of efficient horizontal drilling techniques to extract hydrocarbons from previously uneconomic reservoirs led to a steep escalation in the number of gas and oil wells (Montgomery and Smith, 2010; Rubinstein et al., 2015). The increased injection activities from hydraulic fracturing and disposal of co-produced wastewater led to an increase in the rates of earthquakes in regions that were previously seismically quiescent. There are cases of induced seismicity caused by fluid injection from many parts of the world (Foulger et al., 2018); examples include China (Lei et al., 2013, 2017, 2019), Europe (Dahm et al., 2007; Wilson et al., 2015; Grigoli et al., 2017), and North America (Ellsworth, 2013; Bao and Eaton, 2016; Petersen et al., 2016; Schultz et al., 2017; Eaton, 2018). One of the leading questions regarding induced seismicity has been whether their ground motions are substantially different from those of natural, tectonic earthquakes.

Earthquakes due to hydraulic fracturing are believed to occur on pre-existing faults, especially those favorably-oriented with respect to the regional maximum stress (e.g. Alt and Zoback, 2017; Kettlety et al., 2020). There are three main proposed triggering mechanisms: (e.g. Mcgarr et al., 1994; Schultz et al., 2017): (1) direct hydraulic contact between the well and a pre-existing fault, which leads to an increase in pore pressure along the fault and lowers its effective strength; (2) the injected fluids alter the load and stress conditions in the surrounding rock, affecting faults not in direct contact with the well and possibly driving them towards failure; and (3) the injected fluids lead to an increased pore pressure in the surrounding rock, which diffuses over time and triggers faults at further distances (Brown et al., 2017). The hydraulic fracturing procedures differ between oil and gas companies, as well as the rock conditions in the different regions where it is carried

out. This makes it more difficult for researchers to figure out which wells are more likely induce earthquakes. Atkinson et al. (2016) estimated that only 0.3% of hydraulic fracturing wells were associated with magnitude 3 and above earthquakes in Western Canada Sedimentary Basin (WCSB). As an attempt at earthquake mitigation, many regions have a traffic light protocol in place (e.g. Bosman et al., 2016; Kao et al., 2018; Shipman et al., 2018), in which mitigation measures should be taken at an amber light threshold (often set at magnitude 2) and the well is shut down under red light conditions (often set of magnitude 4 in the WCSB, but much lower in many other regions). Even with the protocol in place, there are numerous of cases of red-light events (e.g. Wang et al., 2017; Mahani et al., 2019). This makes it even more important to understand the earthquakes that have been recorded. It is particularly important when it comes to ground motion models used in seismic hazard analysis because a key component of modelling ground motion is an understanding of the underlying source processes.

The main objective of this thesis is to investigate source parameters of induced seismicity and examine how they affect ground-motion prediction equations (GMPEs) and their variability. I look at the source parameters from both the engineering seismology perspective, where the focus is application to hazard, and the earthquake seismology perspective, where the focus is more theoretical. First, I study source parameters and investigate how small perturbations can affect the GMPE uncertainty. Moving on, I determine source parameters related to the high-frequency content of earthquakes, examining how precisely they can be estimated considering the sparse regional seismic network. Finally, source parameter effects are studied within the context of developing a region-specific GMPE for induced seismicity in WCSB.

1.2 Earthquake Source Parameters

High-frequency ground motion from an earthquake is traditionally modelled as a combination of three components: (1) an earthquake source process that generates the ground motion; (2) attenuation and scattering of the ground motion as it travels through the subsurface; and (3) amplification or reduction of the ground motion due to the shallow subsurface properties at a site. These three components, commonly known as the source, path, and site terms, see Figure 1.1, are typically modeled using a stochastic seismological model (e.g., Boore, 2003). This thesis focuses on analyzing four types of earthquake source parameters: location, magnitude, stress drop, and rupture directivity, which will be described in the following subsections.

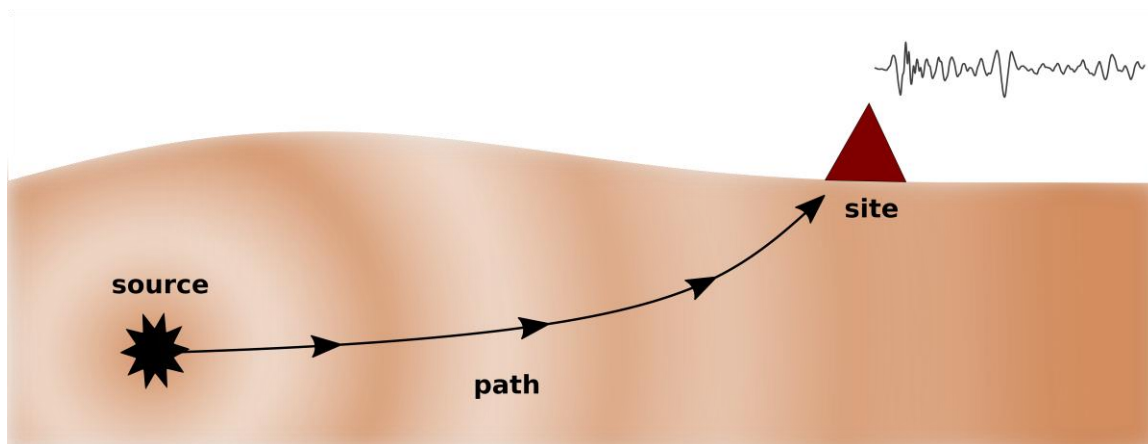


Figure 1.1. Illustration of an earthquake’s source, path, and site components. The station (triangle) records the earthquake ground motions, providing a time series to be analyzed.

1.2.1 Magnitude and Location

The two most utilized source parameters within ground motion modelling are magnitude and location. Earthquake magnitude is a key parameter in describing its size, and is one of the first source parameters defined after an earthquake occurs. Nowadays, magnitude can be estimated using a range of different scales defined in the literature (e.g., Kanamori, 1983). Richter (1935) developed the first widely used scale, known as the local magnitude (M_L), which was based on the largest amplitude of the recorded wave on a Wood-Anderson instrument and the epicentral distance. However a limitation of the Richter scale and other similar scales based on the amplitudes of certain wave types is that the radiated energy saturates, which leads to magnitude underestimation for larger earthquakes (Hanks and Kanamori, 1979; Howell, 1981). To avoid this issue, Kanamori (1977) and Hanks and Kanamori (1979) proposed a moment magnitude (\mathbf{M}) scale based on the seismic moment (M_0), which has become the standard used today:

$$\mathbf{M} = \frac{2}{3} \log_{10} M_0 - 10.7 , \quad (1.1)$$

in which \mathbf{M} is unitless, and M_0 is measured in dyne·cm, or 10^{-7} N·m in SI units. The advantage with M_0 is that it does not saturate because it is a fundamental physical quantity directly related to the physical size of the earthquake. Seismic moment is defined based on the area of the earthquake fault, A , and the average slip, \bar{D} :

$$M_0 = \mu \bar{D} A , \quad (1.2)$$

M_0 can be derived using various seismological methods, e.g. moment tensors and source spectra analysis. I will expand further on the source spectra analysis in Section 1.3.2.

An earthquake's location is a spatial measure of its origin, and typically expressed in terms of latitude and longitude and focal depth; I use the location to calculate the source-to-site distance for all earthquake recordings. If the rupture dimensions are small enough with respect to the distance to the site, the rupture can be modeled as a point source (e.g., Madariaga, 1989). In this case, the distance is either referred to as the hypocentral or epicentral distance, where the hypocenter is the focal point of the rupture and the epicenter is the point on the surface directly above the hypocenter. On the other hand, if the rupture

dimensions are large compared to the source-to-site distance, the point source assumption does not hold. In this case, the distance is measured as the closest distance from the site to the fault or to the fault's surface projection (Joyner and Boore, 1981). As a rule of thumb, **M** 3 earthquakes typically involve ruptures around 100 meters, while **M** 4 earthquake ruptures are around 1 km. Thus, to estimate the source-to-site distance for a close site, one would assume the point source approximation for **M** <4 earthquakes, unless recorded at very close distances. In Chapters 2, 3, and 4, I assume the earthquakes are point sources and use the epicentral and hypocentral distance metrics.

1.2.2 Stress Drop, $\Delta\sigma$

One limitation with magnitude is that it only reflects the size of the earthquake, and not the dynamic effect of the slip relative to the fault area. Stress drop ($\Delta\sigma$), on the other hand, is a source parameter that describes the amount of high-frequency energy released during an earthquake, which will be different depending on the slip rate and fault area; quicker earthquake release, or release over a smaller area, leads to higher stress drop. However, $\Delta\sigma$ is also a parameter plagued by many definitions and many conventions for its determination (e.g., Atkinson and Beresnev, 1997). It takes on multiple roles in seismology: for example, it has been used to describe the amplitude of high-frequency ground motions (Boore, 1983); distinguish between tectonic settings (Allmann and Shearer, 2009; Boyd et al., 2017); and draw inferences regarding earthquake scaling and self-similarity (Abercrombie, 1995; Oth et al., 2010).

Initially, stress drop was a static measure describing the average stress release of an earthquake rupture. It was defined as the difference between the average shear stress acting on the fault before rupture (σ_0) and the average shear stress after rupture (σ_1) (e.g., Kanamori, 1977):

$$\Delta\sigma = \sigma_0 - \sigma_1 \quad (1.3)$$

This can be expressed numerically by assuming Hooke's Law, where the change in stress is related to the change in strain (e.g., Lay and Wallace, 1995):

$$\Delta\sigma = C\mu\left(\frac{\bar{D}}{\tilde{L}}\right), \quad (1.4)$$

in which μ is the shear modulus, C is a constant, \bar{D} is the average slip, and \tilde{L} is a characteristic rupture dimension. Both C and \tilde{L} are dependent on the assumed fault geometry. One of the most commonly used versions of Equation (1.4) is the Eshelby (1957) circular crack model, in which \tilde{L} is assumed to be the rupture radius r and M_0 comes from Equation (1.2):

$$\Delta\sigma = \frac{7}{16}M_0\frac{1}{r^3}. \quad (1.5)$$

One major drawback with stress drop as defined by Equations (1.4) and (1.5) is that information about the fault's rupture area is needed. This is not always available, especially for smaller or deeper earthquakes. To avoid this issue, Brune (1970, 1971) chose to link the far-field seismic energy of body waves to fault dimensions. He used the Aki (1967) "omega-square" source model (see Section 1.3.2) and related the rupture radius to the corner frequency (f_c) of the displacement spectrum:

$$r = \frac{k\beta}{f_c}, \quad (1.6)$$

in which β is the S-wave velocity in $\text{km}\cdot\text{s}^{-1}$, and k is a constant. However, this stress drop does not necessarily equal the static stress drop (e.g., Brune, 1970; Savage and Wood, 1971; Abercrombie and Rice, 2005). The far-field displacement spectrum only picks up large ground motions until the earthquake rupture stops, which is at the frictional stress (σ_f). Thus, if there is an overshoot where the fault relaxes after the rupture has occurred, the final stress will be lower than the frictional stress ($\sigma_1 < \sigma_f$), and thus the stress drop obtained from the far-field spectrum will be smaller than the actual static stress drop. Nevertheless, this definition of stress drop is the most commonly used, and is referred to as the "dynamic stress drop" or "Brune stress drop". When clarification is needed

throughout this thesis, it will be denoted as $\Delta\sigma_{drop}$. There are various k -models for Equation (1.6) in the literature (Brune, 1970, 1971; Sato and Hirasawa, 1973; Madariaga, 1976; Kaneko and Shearer, 2014), which all lead to different stress drop values. Implications of this will be discussed in Chapter 3.

In the early 1980's, stress drop became a parameter of interest in the seismology engineering community when Hanks (1979) and Hanks and McGuire (1981) used it to describe the high-frequency amplitudes of observed ground motions. Their definition of stress drop is commonly referred to as the stress parameter (which we will denote as $\Delta\sigma_{par}$). Similar to $\Delta\sigma_{drop}$, multiple conventions have been developed to determine $\Delta\sigma_{par}$. Initially, the stress parameter was related to the root-mean-square measure of the acceleration spectrum (a_{rms}) (Hanks, 1979; Baltay et al., 2013). Thereafter, it has been used as a high-frequency parameter in stochastic modelling, determined by fitting seismological models to earthquake response spectra (Boore, 2003; Boore et al., 2010). The stress parameter is also regularly used in the development of ground-motion prediction equations (GMPEs, more detail in Section 1.3.3) as an additional tool to describe the high-frequency earthquake source characteristics (e.g., Boore, 1983; Toro and McGuire, 1987; Atkinson and Boore, 1997; Campbell, 2003; Atkinson and Boore, 2006). Chapter 4 goes into more detail on stress parameter and how it relates to the traditional Brune stress drop.

There are numerous studies that have examined patterns in stress drops. Natural earthquakes can have a wide range, usually within 0.1–100 MPa (e.g., Abercrombie, 1995). The large variations could be due to natural variability but may also reflect other factors, for example, bandwidth limitations (Hardebeck and Aron, 2009; Oth et al., 2010; Abercrombie, 2015) and/or model assumptions (Cotton et al., 2013; Kaneko and Shearer, 2015; McGuire and Kaneko, 2018). Many researchers have studied stress drop differences between tectonic and induced earthquakes; there are studies that have found similar ranges (e.g. Tomic et al., 2009; Huang et al., 2016, 2017; Zhang et al., 2016; Ruhl et al., 2017), and studies that have found different ranges (Abercrombie and Leary, 1993; Hough and Page, 2015; Hua et al., 2015; Boyd et al., 2017). Depth dependence has also been investigated, where some detect increased stress drops with increasing depth (Allmann et al., 2009; Rodríguez-Pérez and Singh, 2016; Trugman and Shearer, 2017; Baltay et al.,

2019) and others do not (Abercrombie, Bannister, et al., 2017; Ruhl et al., 2017; Wu et al., 2018). For induced seismicity, the depth dependency on stress could explain why some studies find discrepancies between tectonic and the typically shallow induced earthquakes (Yenier and Atkinson, 2015b; Novakovic et al., 2018; Long, 2019).

1.2.3 Rupture Directivity

When an earthquake propagates along its fault, a source phenomenon known as rupture directivity can be observed (Haskell, 1964). Directivity distorts the symmetry of the radiation pattern and can have a significant influence on the distribution of ground-motion hazard (Boatwright and Boore, 1982). For strong-motion studies, where the low-frequency ground motion of earthquakes are the focus, directivity is commonly observed as a near-source effect that becomes stronger at lower frequencies (<1 Hz) (Somerville et al., 1997; Spudich and Chiou, 2008). However, directivity effects have also been documented over a wide range of frequencies for moderate earthquakes (M 3.5 to 5.5) in California (Seekins and Boatwright, 2010). In this thesis, I focus on how directivity affects the high-frequency content (>5 Hz) of ground motion recorded out to 200 km.

Directivity results from the interaction of the slip direction with the rupture propagation direction, resulting in ground-motion amplitudes that depend on the source-to-site azimuth (Spudich et al., 2008). The simplest case of directivity is a unilateral rupture, where the rupture initiates at one end of the fault and terminates at the other end, only propagating in one direction. In such a case, stations located in the same direction as the rupture propagation will observe shorter durations with higher amplitudes, and stations in the opposite direction will observe longer durations with lower amplitudes, see Figure 1.2 for a schematic view. Because earthquake duration is inversely related to corner frequency, the forward rupture direction will observe more high-frequency content than the backward rupture direction. In more complex cases, such as bilateral ruptures, the rupture propagates in different directions, typically rupturing multiple fault segments.

The effects of directivity have been well documented over the years (e.g., Benioff, 1955; Velasco et al., 1994; Izutani, 2005; Park and Ishii, 2015; Hatch et al., 2018; Lui and Huang, 2019). Large earthquakes are usually the focus, but several studies found directivity effects for smaller earthquakes as well (Boatwright, 2007; Taira et al., 2015; Abercrombie, Poli, et al., 2017). Similarly for injection-induced seismicity, directivity has been observed for earthquakes from moderate size (Lui et al., 2019) to microearthquake size (Folesky et al., 2016). This is explored further in Chapters 3 and 4.

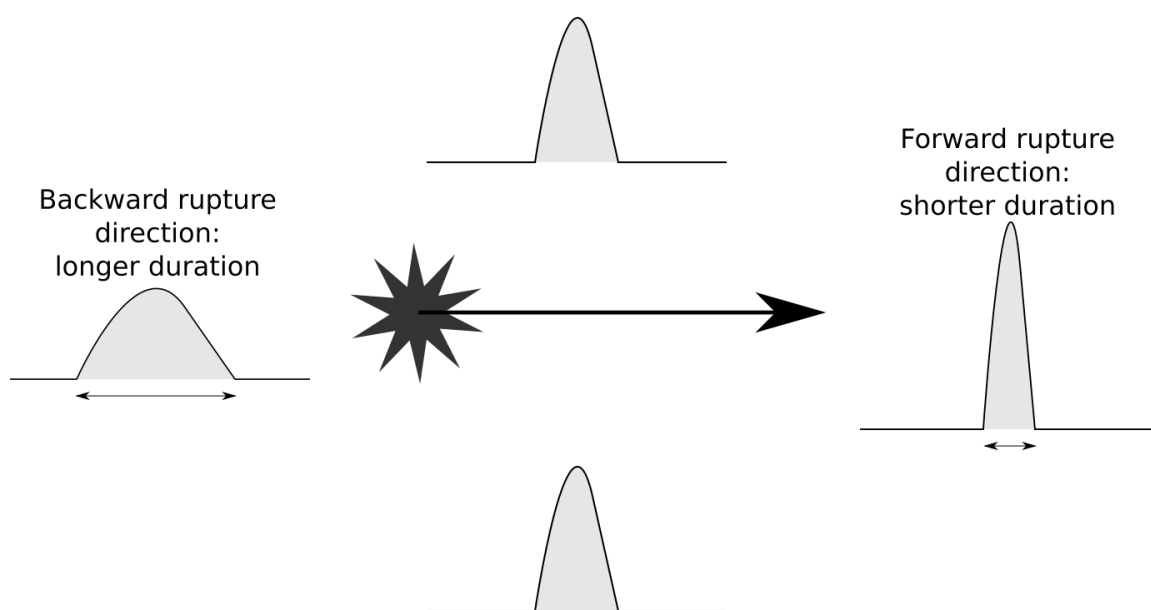


Figure 1.2. A schematic illustration of rupture directivity and the resultant source pulses observed at different azimuths. The rupture initiation and rupture path are given as a star and arrow, respectively. The shaded grey area within the pulses signify the constant M_0 observed at all azimuths.

1.3 Modelling Ground Motions

When an earthquake occurs, its ground motions travel through the subsurface and will be recorded as time series at various seismic stations throughout the region. There are multiple techniques developed to process, study, and model the time series. Seismologists tend to analyze the time series' Fourier spectrum, whereas engineering seismologists look at response spectra and other measures of ground motion intensity. In this section, I will describe Fourier and response spectra, and discuss two earthquake models that I will focus on in Chapters 2, 3, and 4.

1.3.1 Fourier and Response Spectra

To study an earthquake in the frequency domain, one can either look at the earthquake's ground motion content directly using Fourier spectra, or assess how the motions would affect structures according to their fundamental period, using response spectra. Fourier amplitude spectra (FAS) are computed by applying the Fast Fourier Transform (FFT) to convert a time series from the time domain to frequency domain. In simpler terms, the FFT displays the amplitude of sinusoidal signals within the motion as a function of frequency. The Fourier domain has certain advantages over time domain. For example, in Chapter 3 we will see that time series deconvolution is simplified to the equivalent spectral division in the Fourier domain.

Engineers are interested in how structures respond to a ground motion. Structures can be modeled using single-degree-of-freedom (SDOF) damped oscillators with a given natural frequency (f_0) (Benioff, 1934; Biot, 1941; Nigam and Jennings, 1969). Each oscillator's motion ($x(t)$) is estimated by solving the equation of motion for a damped harmonic oscillator:

$$\ddot{x}(t) + 2\xi\omega_0\dot{x}(t) + \omega_0^2x(t) = -\ddot{x}_g(t) , \quad (1.7)$$

in which ξ is the oscillator's damping ratio, ω_0 is the oscillator's natural angular frequency ($\omega_0 = 2\pi f_0$), and $\ddot{x}_g(t)$ is the earthquake's acceleration time series. By calculating maximum response for each oscillator's x and plotting it against the oscillator's f_0 , a

displacement response spectrum (SD) can be constructed. Typically the spectra are estimated for 5% damped pseudo-spectral acceleration (PSA), which is $SD \times (2\pi f_0)^2$. Nigam and Jennings (1969) derived a numerical solution to Equation (1.7), which is commonly used to estimate response spectra of earthquakes (e.g., Abrahamson and Somerville, 1996; Boore et al., 2012; Atkinson, Assatourians, et al., 2015). Another common method used to compute response spectra in ground motion modeling is random vibration theory (RVT), which is less computationally intensive than the Nigam and Jennings method (Vanmarcke and Lai, 1980; Boore, 2003). Instead of working with time series directly, RVT uses extreme value statistics and Parseval's theorem to relate the FAS to peak motions at different oscillator frequencies (e.g., Bora et al., 2016; Van Houtte, Larkin, et al., 2018).

FAS and PSA are not linearly related, and thus adjustments need to be made when moving between them (e.g., Bora et al., 2016). The difference is easily illustrated using RVT. Figure 1.3 shows an example time series and its resultant FAS and PSA. In the RVT analysis, one of the steps includes multiplying the FAS by a SDOF transfer function, which is dependent on the oscillator frequency f_0 . Five sample f_0 transfer functions are shown in

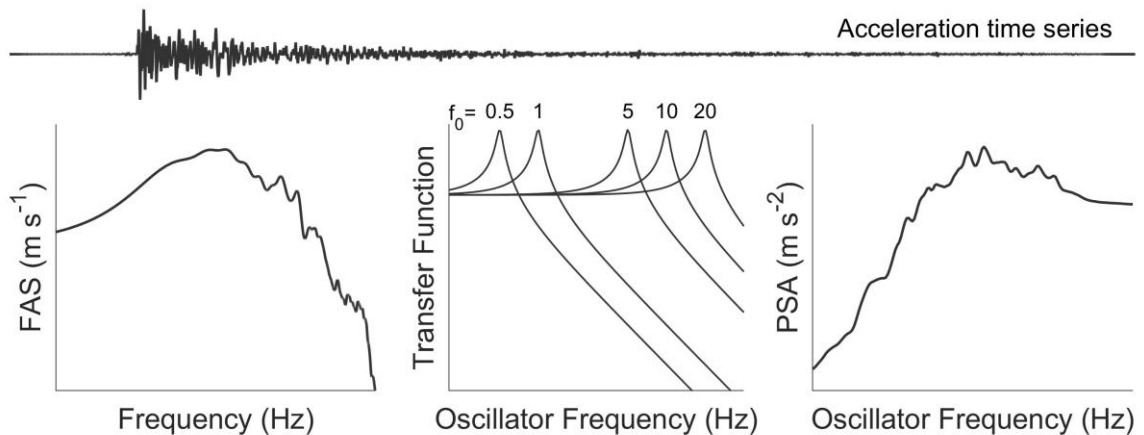


Figure 1.3. Comparison between Fourier amplitude spectrum (FAS) and pseudo-spectral acceleration (PSA). (Top) acceleration time series being analyzed. (Bottom, left) FAS of the time series. (Bottom, middle) SDOF transfer functions used in RVT to retrieve the response spectrum. (Bottom, right) response spectrum of the time series.

the middle image of Figure 1.3, and as can be seen, each transfer function is dependent on the lower frequencies. In other words, the high frequency content in a response spectrum is controlled by both high and low frequency content in the equivalent Fourier spectrum. Chapter 4 compares the source parameters $\Delta\sigma_{drop}$ and $\Delta\sigma_{par}$ to explore these differences.

1.3.2 Brune Source Model

In 1967, Aki set out to describe the source FAS with as few parameters as possible. He developed the “omega-square” (ω^2) source model, in which the far-field amplitude decreases inversely with the squared frequency beyond the corner frequency (f_c). Below f_c , the amplitude is flat at a level that is proportional to M_0 . Brune (1970, 1971) then assumed a circular rupture and used the ω^2 model to relate f_c to the rupture radius r (Equation 1.6). The equation for the so-called Brune source model of the far-field displacement spectrum $\Omega(f)$, including path and site components, has the form:

$$\Omega(f) = \frac{\Omega_0}{\left[1 + \left(\frac{f}{f_c}\right)^{\gamma n}\right]^{\frac{1}{\gamma}}} e^{-\frac{\pi f R}{\beta Q(f)}} e^{-\pi f \kappa} , \quad (1.8)$$

in which f is frequency (Hz), Ω_0 is the low-level plateau ($\text{cm}\cdot\text{s}$), γ is the shape constant, n is the high-frequency fall-off ($n = 2$ for the ω^2 model), R is the earthquake’s source-to-site distance (cm), β is the seismic S-wave’s velocity at the source ($\text{cm}\cdot\text{s}^{-1}$), $Q(f)$ is the frequency dependent quality factor typically used as a path effect, and κ describes the high frequency spectral decay of ground motion. Many use the Brune (1970) version of Equation (1.8), in which $\gamma = 1$. Boatwright (1980) found that earthquakes had a sharper transition between the constant low-frequency plateau and high-frequency fall-off, and instead defined $\gamma = 2$. Figure 1.4 schematically compares the Brune and Boatwright models. Ω_0 is related to the seismic moment M_0 through (Brune, 1970):

$$M_0 = \frac{4\pi\rho\beta^3 R\Omega_0}{FU_{\Phi\Theta}} , \quad (1.9)$$

in which ρ is the density at the source ($\text{g}\cdot\text{cm}^{-3}$), β is the S-wave velocity at the source, R is the hypocentral distance, F is the free surface parameter ($F = 2$), and $U_{\phi\theta}$ is the mean radiation pattern for the or S-wave ($U_{\phi\theta} = 0.63$) (Aki and Richards, 1980).

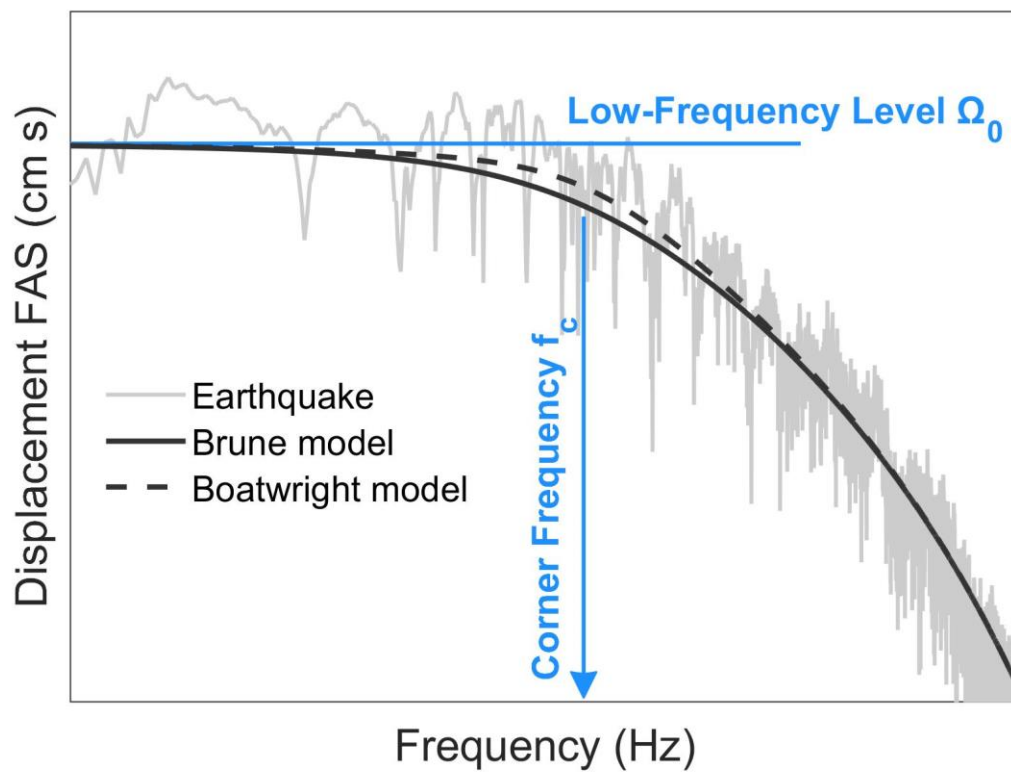


Figure 1.4. Brune (solid black) and Boatwright (dashed black) source models plotted on top of an earthquake record's displacement Fourier spectrum. The corner frequency and low-frequency level are emphasized in the figure.

1.3.3 Ground-Motion Prediction Equations

In engineering seismology, earthquake ground motions are usually modelled in the response spectrum domain. These models are known as ground-motion prediction equations (GMPEs) or ground motion models (GMMs). Usually they estimate the expected ground motion amplitudes - typically 5%-damped PSA, along with peak ground acceleration (PGA) and peak ground velocity (PGV) - for a given magnitude, distance, site condition, and other explanatory variables.

GMPEs have many different functional forms (e.g., Toro et al., 1987; Youngs et al., 1995; Campbell, 2003; Boore et al., 2014; Atkinson, 2015; Yenier et al., 2015b; Douglas, 2017). The basic form can be described by (Boore, 2003):

$$Y(M_0, R, f) = E(M_0, f)P(R, f)G(f)I(f) \quad (1.10)$$

where Y is the ground motion intensity measure (e.g. PSA, PGA, or PGV), E is the earthquake event term describing the source effect, P is the path term, G is the site term, and I is the instrument response or a filter accounting for a type of motion. The number of independent variables differs between GMPEs. Common variables include earthquake magnitude, focal mechanism, stress parameter, a distance metric, and some site parameter (e.g., Campbell, 1985). GMPEs are used extensively in probabilistic seismic hazard analysis (PSHA) and Shakemap applications, where Shakemaps show the intensity of shaking throughout a region following significant earthquakes.

GMPEs can be derived using various approaches. In regions with abundant records of earthquakes, the models are typically developed empirically by applying different regression models to the ground-motion data (e.g., Abrahamson and Silva, 1997; Abrahamson et al., 2014; Ambraseys et al., 2005; Bindi et al., 2007; Boore et al., 2014; Campbell and Bozorgnia, 2014; Atkinson, 2015). For regions with sparse records the stochastic approach is more common, where data are stochastically simulated based on ground-motion models (e.g., Boore, 1983, 2003; Boore and Atkinson, 1987; Boore and Joyner, 1991; Atkinson and Boore, 1997; Edwards and Fäh, 2013; Bora et al., 2014; Drouet and Cotton, 2015), which are then calibrated with the sparse available data. The third

method used to develop GMPEs is a combination of empirical and simulation, known as the hybrid approach, where GMPEs from earthquake rich regions are adapted to more sparse regions (e.g., Campbell, 2003; Atkinson, 2008; Pezeshk et al., 2011; Zafarani et al., 2017). In this thesis, two different types of GMPEs will be used. Chapter 2 focuses on the empirical Atkinson (2015) GMPE for small-to-moderate events, and Chapter 4 focuses on the stochastic-generic GMPE developed by Yenier and Atkinson (2015a; Yenier et al., 2015b).

There are two main types of uncertainties in GMPEs: aleatory and epistemic uncertainty (e.g., Strasser et al., 2009). Aleatory uncertainty describes the scatter of earthquake observations about a zero-biased median and is due to the natural (or unmodeled) randomness of earthquake processes. Epistemic uncertainty describes uncertainty in the median due to incomplete knowledge of the model parameters and databases. Epistemic uncertainty encompasses, for example, the differences in GMPEs produced for the same region by different researchers. The distinction between epistemic and aleatory uncertainty is sometimes ambiguous, as more sophisticated, knowledge-rich models might (or might not) lead to reduced aleatory variability, and thus there may be some degree of epistemic uncertainty that is cast into aleatory uncertainty. The total aleatory uncertainty is referred to as sigma (σ , note: not to be confused with stress drop $\Delta\sigma$), and is assessed by computing the standard deviation of the residuals between the observed ground motion and the GMPE in logarithmic space.

In turn, sigma can be divided into two components: the between-event term (also known as the inter-event term, τ) and the within-event term (also known as the intra-event term, ϕ) (Joyner et al., 1981; Abrahamson, 1988; Youngs et al., 1995; Al Atik et al., 2010):

$$\sigma = \sqrt{\tau^2 + \phi^2} . \quad (1.11)$$

The between-event component describes the earthquake-to-earthquake variability, related to the earthquake source effects not accounted for in the model. The within-event component describes the record-to-record variability, and is related to path and site effects not accounted for in the model. Generally, the between-event component tends to be smaller than the within-event component (Joyner et al., 1981; Brillinger and Preisler, 1984;

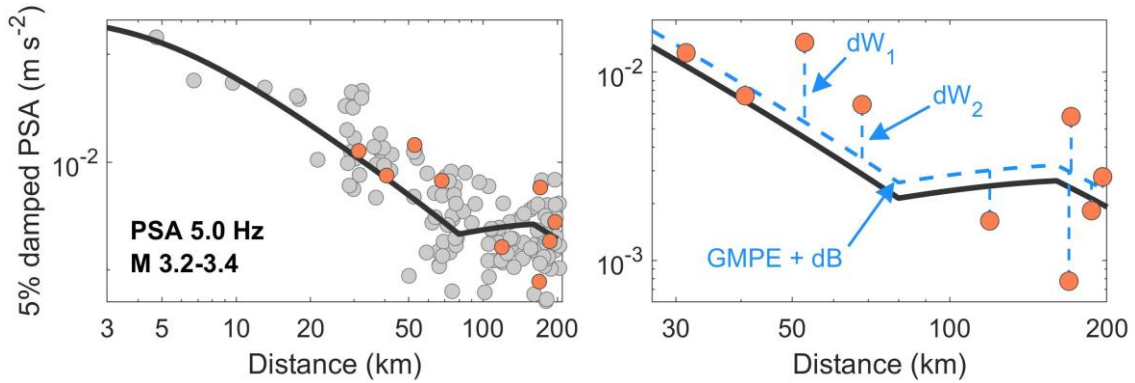


Figure 1.5. Example of a GMPE (solid line) developed for M 3.2-3.4 earthquake records at PSA 5.0 Hz (circles) plotted against distance. (Left) The scatter from multiple earthquakes, with one earthquake highlighted (orange circles). (Right) Zoom-in on the highlighted earthquake's records, visualizing the dB and dW terms.

Strasser et al., 2009). The sigma, between-, and within-event components are commonly expressed in logarithmic units, either using the base of 10 or the natural logarithm. Based on common values from published GMPEs, the between-event component tends to lie between 0.05-0.27 log10 units, and the within-event component between 0.10-0.40 log10 units (e.g. Douglas, 2017). Figure 1.5 visualizes the variability of ground motions with respect to a GMPE. The left image shows 10 earthquakes with M 3.2-3.4 and their PSA 5.0 Hz amplitudes plotted against distance. As can be seen, even though the ground motion records follow the general shape of the GMPE, there is still a scatter due to the randomness of earthquakes. To look at the variability further, one earthquake's records have been highlighted. The right image shows a zoom-in on the highlighted earthquake. The average difference between the GMPE and an earthquake's records is denoted dB , while the individual differences between the earthquake average (i.e., $GMPE + dB$) and the record is denoted dW_i , where i is the record number. The between-event is simply the standard deviation of all earthquake dB values, while the within-event is the standard deviation of all record dW values. The dB and dW terms can be reduced by improving the source parameters. Essentially, by changing the location of an earthquake, the records' distances will change and therefore affect dW_i . On the other hand, by changing the magnitude of an

earthquake, the overall level of the GMPE will change and therefore affect dB . This is explored in Chapter 2.

It should be noted that the source is not the only contributor to uncertainty – path and site can also play large roles. There are various ways to model both, which leads to differences in the resultant GMPEs (encompassed in the epistemic uncertainty). For example, site effects may include pronounced amplification or deamplification, and may exhibit non-linear behavior for larger earthquakes. For this thesis, I focus on the source as there are many unresolved questions concerning how the differences in source mechanisms between natural and induced events may impact ground motions.

1.4 Organization of Thesis

This thesis is presented in five chapters. Chapter 1 introduces the motivation behind the thesis, as well as relevant background material for the studied source parameters and different approaches to model them.

Chapter 2 explores the variability of induced earthquakes in central United States, focusing on how small perturbations of source parameters can affect the modelled ground motions and sigma. Using a zero-biased GMPE, I am able to show that by letting the GMPE choose the optimum location and magnitude for each earthquake, the sigma and its components decrease significantly. This implies that the uncertainties of source parameters are being double counted to some degree in probabilistic seismic hazard analyses (PSHA).

In Chapter 3, I analyze corner frequencies and stress drops of induced earthquakes in WCSB, Canada, using the Empirical Green's Function (EGF) method. By investigating the corner frequencies and how they vary with station azimuth, I find that the region exhibits clear directivity patterns. Due to the sparse station coverage, I use the Haskell (1964) directivity model instead of the traditional EGF method to compute the final corner frequencies and stress drops for these earthquakes.

Chapter 4 examines how the stress drops from Chapter 3 can be utilized in GMPEs as a proxy for stress parameter. I start off by defining a region-specific GMPE for WCSB, investigating its variability with respect to directivity. I then use the GMPE to compute stress parameters for each earthquake, in order to compare these to the original stress drop estimates from Chapter 3. I find that stress drop is much more efficient at detecting high-frequency content, especially for earthquakes displaying directivity. The final chapter lists the thesis' overall conclusions and novel contributions, as well as suggestions for future work.

Chapter 2

2 Effect of Uncertainty in Source Parameters on Ground-Motion Variability for Potentially Induced Earthquakes in the Central United States¹

In this chapter, I explore the effects of small perturbations in earthquake magnitude and location on the variability of ground-motion prediction equations (GMPEs).

2.1 Introduction

The variability in earthquake ground-motion amplitudes about the median values of GMPEs, commonly referred to as sigma (σ), plays an important role in seismic hazard assessment. As sigma increases, so does the likelihood of strong-ground motion, due to the interplay between the ground-motion distribution and the Gutenberg-Richter distribution (Bommer and Abrahamson, 2006; Strasser et al., 2009). The Central United States (CUS) is a region that has experienced a marked increase in seismicity during the last decade, and the seismic hazards associated with the seismicity are of significant concern (Hough et al., 2015; Petersen et al., 2016, 2017). An important component of assessing the hazard from this activity is gaining an understanding of the impact of uncertainty and variability in ground motions.

To model the median ground-motion amplitudes in a region, ground-motion prediction equations (GMPEs) are commonly developed as functions of source and site variables. As mentioned in Section 1.3.3, sigma is the total aleatory uncertainty; the standard deviation associated with the GMPE, reflecting the scatter of the amplitudes about the median predicted values. In order to minimize the effect of the epistemic uncertainty

¹ A version of this chapter has been published. Holmgren, J. M. and G. M. Atkinson (2018). “Effect of Uncertainty in Source Parameters on Ground-Motion Variability for Potentially Induced Earthquakes in the Central United States”, *Seismological Research Letters*, **89**(2A), 702-711.

of the GMPE, we consider a GMPE that is zero-biased for a particular dataset. Thus we can focus our attention on the aleatory uncertainty associated with the model and its driving factors. In particular, we divide sigma into its two components, the between-event term (τ) and the within-event term (ϕ), and examine how they are affected by small perturbations in the source parameters (magnitude and location).

Due to its importance in hazard assessment, there have been many studies dealing with sigma and how it might be reduced, including better consideration of site classification (e.g., Bindi et al., 2006; Derras et al., 2016), incorporation of repeatable residual trends into GMPEs (Baltay et al., 2017), the use of single-station values of sigma (e.g., Atkinson, 2006), attempts to avoid double-counting of uncertainties (e.g., Atkinson, 2013), and developing non-ergodic/partially non-ergodic GMPEs to account for geographical variations (Kotha et al., 2016; Landwehr et al., 2016). A few authors have obtained lower sigma values by including the parameters' uncertainty in the GMPEs through various uncertainty propagation procedures: Rhoades (1997) decreased the between-event variability by including the uncertainty in magnitude; Moss (2011) reduced sigma by 5-10% by including uncertainties in site classifications; and Kuehn and Abrahamson (2017) reduced sigma by 1-13% by including both magnitude and site classification uncertainties. In this paper, we focus on how variations in earthquake magnitude and location affect the variability in ground-motion modeling, reflecting the uncertainty in source parameters. This follows work by Abrahamson and Silva (2007), who found that by removing magnitude uncertainty from the between-event component of sigma, variability was reduced at long periods. Likewise, they found that by removing distance and site condition uncertainties from the within-event component, there were further reductions in sigma.

We consider the uncertainty in ground-motion amplitudes for well-recorded earthquakes from potentially-induced earthquakes in the CUS, and how it might be reduced by optimizing the magnitude and location of events. We first define a zero-biased GMPE from a ground-motion database, and then determine to what extent we can minimize sigma. By computing both the between- and within-event components of sigma, we can assess whether a change in magnitude or location has a larger impact on sigma. We emphasize that the purpose of the study is to explore sigma. The zero-biased GMPE is developed just

as a foundation for this assessment, and is not being proposed as a regional GMPE for other purposes. Likewise, we are not proposing to use GMPEs as a means of re-assigning catalogue magnitudes and locations. However, the extent to which sigma can be reduced by optimizing magnitude and location is informative as to the overall uncertainty in these parameters, within the ground-motion context.

2.2 CUS Ground-Motion Database

A ground-motion database comprising earthquakes in the CUS was used in this study. A description of the processing procedures and the database can be found in Assatourians and Atkinson (2010) and Atkinson and Assatourians (2017), and a description of the initial moment magnitude (**M**) calculations is presented in Novakovic and Atkinson (2015). The locations of the earthquakes are obtained from the catalogues of the U.S. Geological Survey (USGS) and the Oklahoma Geological Survey (OGS). The final database was compiled by Novakovic (personal communication, 2017). Within a hypocentral distance of 300 km, there are 38,784 ground-motion records from 995 earthquakes of M3.0-5.6 during the years 2010-2017, as shown in Figure 2.1. These records were used to examine the ground motions and develop a zero-biased GMPE (described in the following). The site conditions are generally NEHRP (National Earthquake Hazards Reduction Program) class B and C in the CUS region, reflecting rock to soft rock sites (Yong et al., 2016).

Thirty-eight events from the database were selected for sigma analysis at closer distances. These were chosen based on the criteria of having at least four records within a hypocentral distance of 10 km. These are the best-recorded events, which should be most sensitive to changes in both magnitude and location; they are highlighted in Figure 2.1. For these events, we consider only those observations within 70 km, to avoid complexities in attenuation due to crustal structure effects that become pronounced at larger distances.

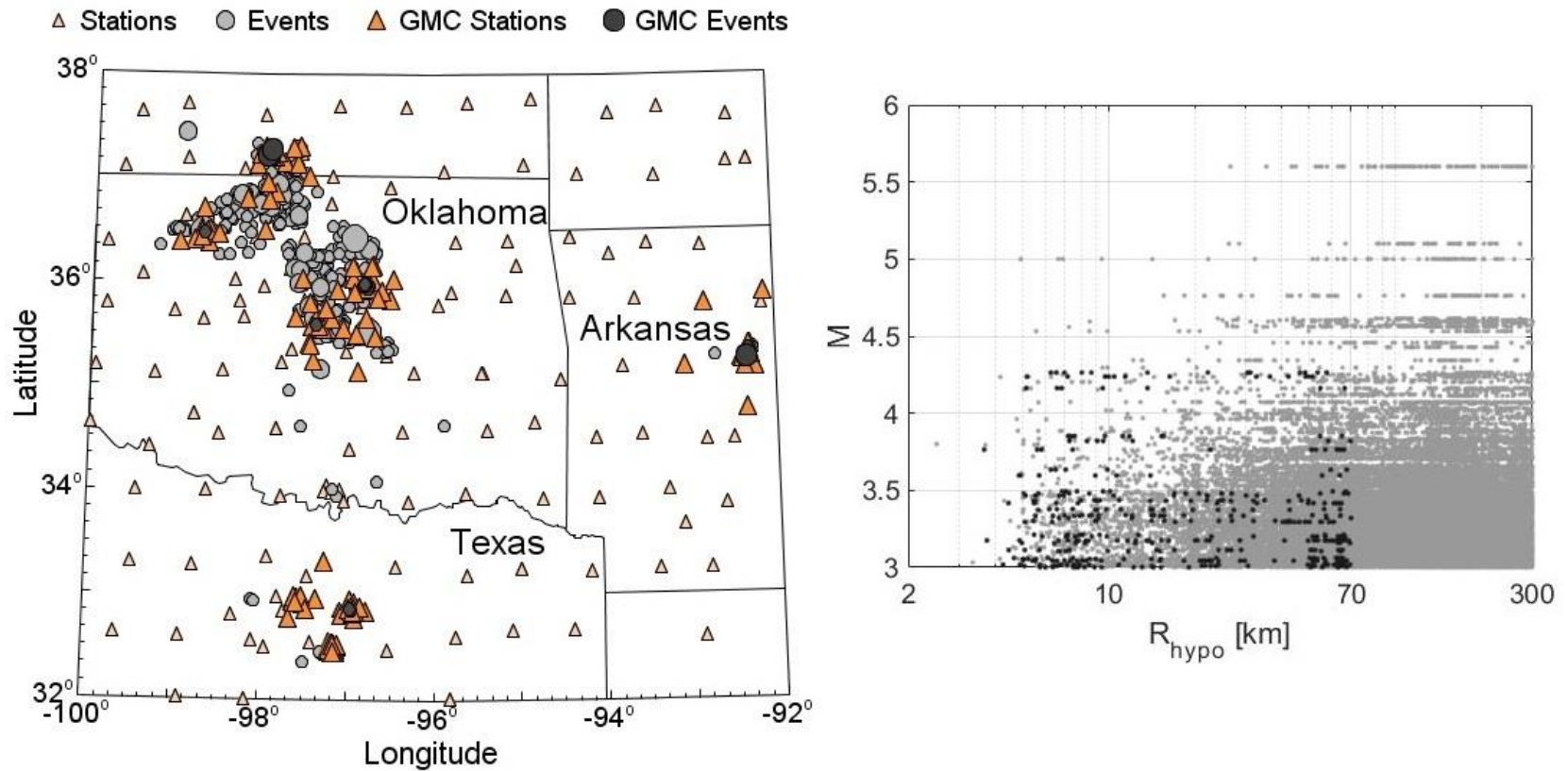


Figure 2.1. (Left) The stations (triangles) and earthquakes (circles; U.S. Geological Survey/Oklahoma Geological Survey [USGS/OGS] reported epicenters) used in this study to compute the zero-biased ground-motion prediction equation (GMPE) from the ground-motion database. The darker shaded stations and earthquakes are those used for the ground-motion center (GMC) sigma analysis. The size of circle scales with magnitude. The lighter shades vary between M 3.0 and 5.6, and the darker shades vary between M 3.0 and 4.3. (Right) Scatter plot of the data shown to the left, with the same shading.

2.3 Zero-Biased GMPE

The first step of examining sigma is to define a zero-biased median GMPE for the earthquakes in the region (e.g., Baltay et al., 2017), which can be used as a foundation for the assessment of aleatory variability. For this purpose, we use the larger database shown in Figure 2.1. We use the GMPE developed by Atkinson (2015; hereafter, A15) for small-to-moderate events, as a function of hypocentral distance, as a convenient starting point. The A15 GMPE is an empirical GMPE derived from the Next Generation Attenuation (NGA) West2 database of ground motions recorded for events of **M** 3-6 at hypocentral distances less than 40 km. Both Atkinson and Assatourians (2017) and Gupta et al. (2017) showed that the A15 GMPE can be used to describe median induced-earthquake amplitudes in the CUS to distances of 50 to 70 km. We improve upon the A15 GMPE for this application by using the referenced-empirical approach (Atkinson, 2008) to adjust the A15 GMPE to ensure zero bias. The referenced-empirical approach is based on fitting a simple function in distance to the residuals of a reference GMPE (in this case A15) to achieve zero bias.

Using the larger database shown in Figure 2.1, the residuals of the observations for 955 earthquakes were computed with respect to the predictions of the A15 GMPE (horizontal component, for NEHRP B/C conditions). The vertical component was used initially to lessen the impact of site effects. To more completely deal with site response, we calculate a station term for each station (at each frequency) as the average residual for the station, and subtract that term. Although this is done initially for the vertical component, we also calculate the corresponding station terms for the horizontal components so that the sigma reduction can be evaluated for both components. We focused on 5% damped pseudo-spectral acceleration (PSA) response spectra at 0.5, 1.0, 3.3, and 10.0 Hz, as well as peak ground acceleration (PGA) and peak ground velocity (PGV). The residuals e between the observed ground motions Y_{obs} and the predicted motions Y_{pre} can be expressed as:

$$e = \log_{10} Y_{obs} - \log_{10} Y_{pre} \quad (2.1)$$

Y_{pre} was initially computed from the A15 GMPE:

$$\log_{10} Y_{pre} = c_0 + c_1 \mathbf{M} + c_2 \mathbf{M}^2 + c_3 \log_{10} R_{eff} \quad (2.2)$$

in which Y_{pre} is the ground-motion parameter, c_0 - c_3 are frequency dependent coefficients given in A15 and Table 2.1, and R_{eff} is an effective point-source distance:

$$R_{eff} = \sqrt{R_{hypo}^2 + h_{eff}^2} \quad (2.3)$$

in which R_{hypo} is the hypocentral distance and h_{eff} is an effective depth parameter given by the A15 alternative $h_{eff} = \max(1, 10^{(-0.28+0.19\mathbf{M})})$. The events have an average depth of 5.3 km, according to the USGS/OGS catalogue, with an average error in depth of ± 5.8 km. For simplicity, we therefore set the hypocentral depth to 5 km for all earthquakes.

As shown in Figure 2.2 for the vertical PGV component, we observed that the initial residuals computed from the A15 GMPE have negative trends at close distances; this was observed for the six ground-motion parameters studied. To center the residuals and obtain a zero-biased GMPE, a quadratic correction term based on the residuals using Equation (2.2) was added:

$$D = d_1 + d_2 \log_{10} R_{eff} + d_3 (\log_{10} R_{eff})^2 \quad (2.4)$$

Table 2.1. Coefficients of Equations (2.2) and (2.4) for each pseudospectral acceleration (PSA; 5% damped) frequency and peak ground acceleration (PGA) and peak ground velocity (PGV).

PSA at frequency	c_0	c_1	c_2	c_3	d_1	d_2	d_3
0.5	-4.462	1.485	-0.03715	-1.361	-1.485	1.309	-0.256
1.0	-4.081	1.742	-0.07381	-1.481	-1.256	0.909	-0.118
3.3	-2.794	1.852	-0.10780	-1.608	-1.122	0.577	0.000
10.0	-1.954	1.830	-0.11850	-1.774	-0.683	0.459	0.000
PGA	-2.376	1.818	-0.11530	-1.752	-0.321	0.435	-0.046
PGV	-4.151	1.762	-0.09509	-1.669	-0.602	0.406	0.000

in which d_1-d_3 are frequency dependent coefficients, given in Table 2.1. Then, station correction terms were calculated for each station having at least three records (stations with fewer records were removed). This gives a final functional form of the zero-biased GMPE:

$$\log_{10} Y_{pre} = c_0 + c_1 \mathbf{M} + c_2 \mathbf{M}^2 + c_3 \log_{10} R_{eff} + D + S \quad (2.5)$$

in which S is the station correction term and the other terms are as defined in Equations (2.2) and (2.4). Figure 2.2 shows how the PGV residuals improved with the modifications made for both the vertical and horizontal components. For the horizontal component, we tested whether a zero-biased GMPE could be obtained just by removing the station terms, but found that this removed only some of the trends; a distance correction is also required. It should be noted that Equation (2.5) is not a proposed GMPE to be used in CUS, it is simply the A15 GMPE manipulated to provide a zero-bias foundation from which we can explore sigma.

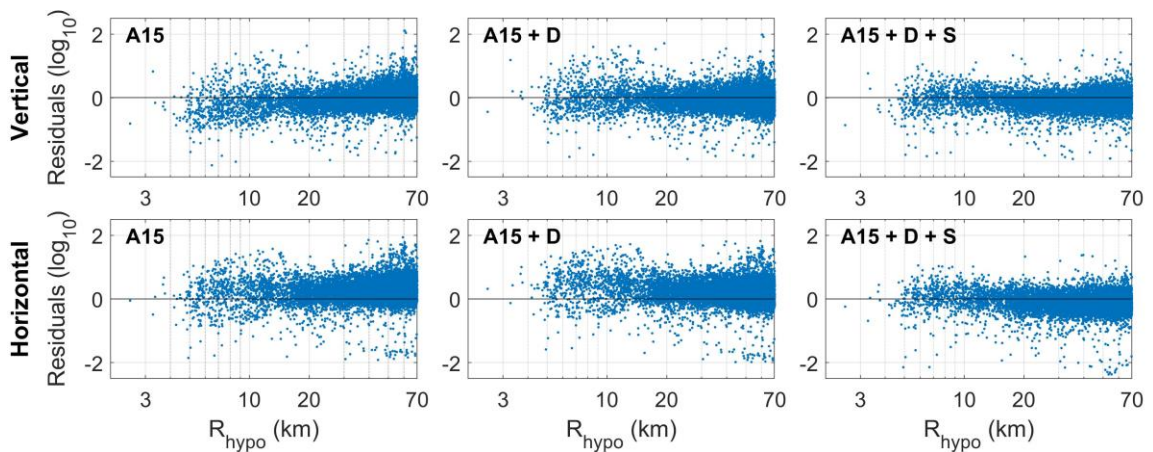


Figure 2.2. (Top) Peak ground velocity (PGV) residuals for the vertical component plotted against hypocentral distance using (left) the Atkinson (2015; hereafter, A15) GMPE, (middle; A15 + D) a zero-biased GMPE, and (right; A15 + D + S) a zero-biased GMPE after removal of stations terms. (Bottom) PGV residuals for the geometric mean of the horizontal components.

2.4 Ground-Motion Center

Using the zero-biased GMPE (Equation 2.5) as the median prediction, we examine to what extent we can reduce the residual variability (σ) by changing earthquake magnitude and location. We base the assessment on the data from 38 well-recorded earthquakes as previously described. To minimize σ , we find the ground-motion center (GMC) for each event. Following concepts originally introduced by Kanamori (1993), we define the GMC as the location and moment magnitude that results in the lowest standard deviation of residuals with respect to the zero-biased GMPE (Equation 2.5), using the vertical component. We re-iterate that we are not proposing the GMC as an optimal tool to locate earthquakes or to determine their magnitude; the GMC is simply the preferred epicenter and magnitude from the perspective of the GMPE, and may deviate from the true epicenter and magnitude of the earthquake. Any reductions found in σ due to change in magnitude and location are assumed to reflect contributions of uncertainties in all source effects that affect amplitudes, including moment, stress drop, and focal mechanism.

The GMC is calculated using an iterative grid-search technique, alternating between searching for the optimum epicenter (odd iterations) and searching for the optimum magnitude (even iterations). The starting point for the iterations is the location given in the USGS/OGS catalogs, with the initial moment magnitudes calculated using the algorithm of Novakovic and Atkinson (2015). The grid steps used were 0.5 km and 0.01 M , with a maximum considered deviation of 10 km from the previous epicenter or 0.5 M from the previous magnitude per iteration. The GMC is first calculated for each of the six different ground-motion parameters (PSA at 0.5, 1.0, 3.3, and 10 Hz, PGA, and PGV). The final GMC at each iteration is then taken as the average location and magnitude over these six parameters. The grid search is stopped when the total σ of all the events converges. To examine the variability at close distances, the value of σ for records within a hypocentral distance of 10 km is also calculated. In addition to the total σ , the between-event term τ and the within-event term ϕ (see Section 1.3.3) are calculated at each iteration to see which is affected more:

$$\sigma = \sqrt{\phi^2 + \tau^2} \quad (2.6)$$

2.5 Results

Figures 2.3 and 2.4 show the development of the total sigma at each iteration for all records ($R_{hypo} \leq 70$ km) and for $R_{hypo} \leq 10$ km, respectively, for the vertical component. The final iteration was set to iteration 4, because sigma has converged by this point for all events. The between-event term decreased more than the within-event term. In terms of variance components (which are additive in obtaining the total variability), there was an 84% reduction in the between-event variance, and a 25% reduction in within-event variance, considering all records on the vertical component. The total variance was reduced by 61% on average (corresponding to a reduction in total sigma from 0.39 log10 units to 0.24 log10 units). Similar trends can also be seen in the variabilities for the subset of events within 10 km. Tables A2.1 and A2.2 list the variability components for all parameters, for both subsets, for both the vertical and horizontal components, respectively.

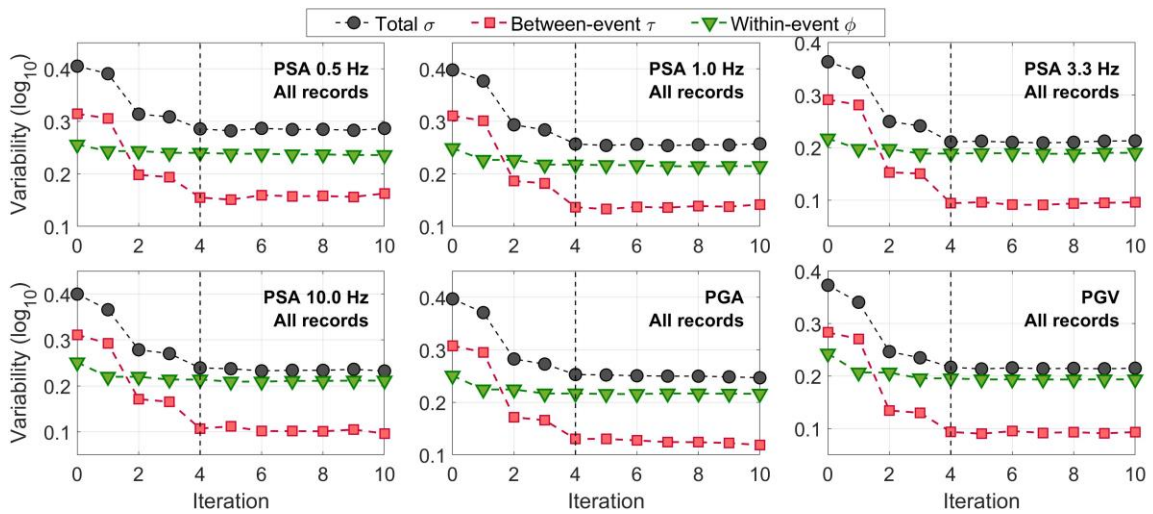


Figure 2.3. The total variability, between-event term, and within-event term for each iteration of the iterative grid search, for selected ground-motion parameters (pseudo-spectral acceleration [PSA] at 0.5, 1, 3.3, and 10 Hz, peak ground acceleration [PGA], and peak ground velocity [PGV]), for the vertical component, using all records within 70 km. The odd iterations are grid searches optimizing the locations, and the even iterations optimize the magnitudes. Iteration 4 is marked as the final iteration.

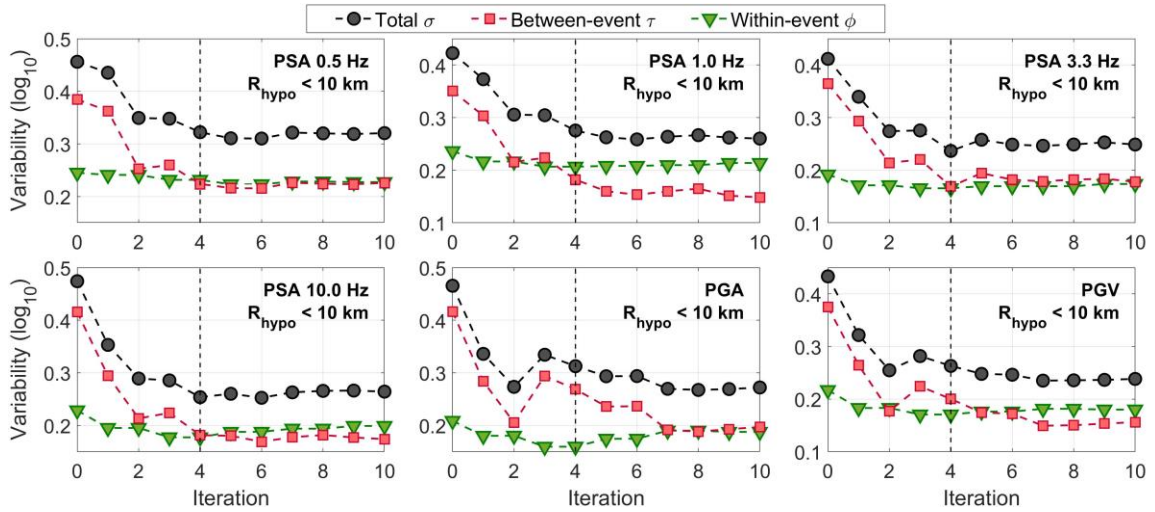


Figure 2.4. The total variability, between-event term, and within-event term for each iteration of the iterative grid search, for selected ground-motion parameters (PSA at 0.5, 1, 3.3, and 10 Hz, PGA, and PGV), for the vertical component, using only those records within a hypocentral distance of 10 km. The odd iterations are grid searches optimizing the locations, and the even iterations optimize the magnitudes. Iteration 4 is marked as the final iteration.

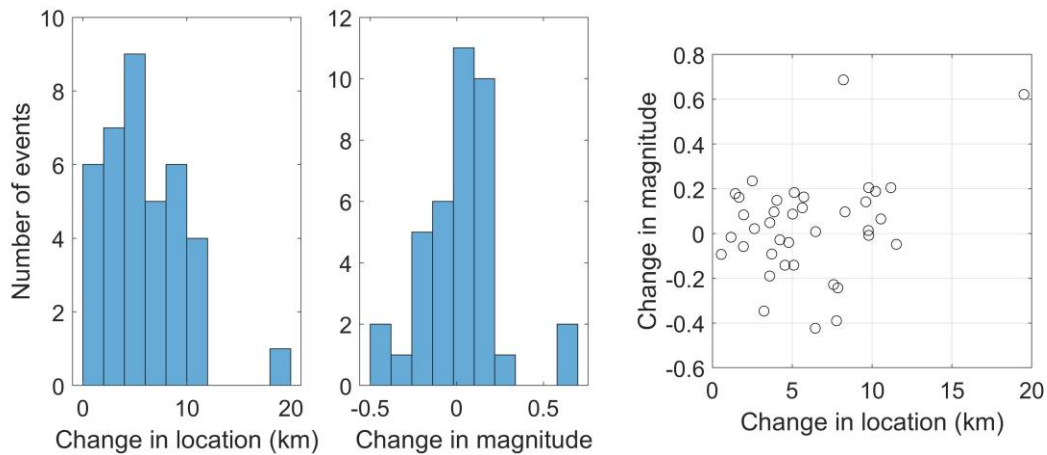


Figure 2.5. A histogram of the amount of change in (left) location and (middle) magnitude between the initial and optimized locations and magnitudes of the 38 study events. (Right) The change in magnitude and location for each event.

Figure 2.5 shows a histogram illustrating the change in location (left) and magnitude (middle) for the 38 earthquakes (at iteration 4). The GMC epicenter locations moved on average ~ 6 km, with one event relocating 19.5 km away. The change in magnitude varied between -0.4 and $+0.7$ from event to event, but the average change in magnitude was nil. The change in magnitude is plotted against the change in location in the right image of Figure 2.5. There is a small trade-off between magnitude and location, which we explored by adding perturbations to the initial magnitudes and locations (changing the initial magnitudes by a random error up to ± 1 units and moving the initial locations up to 0.5 km), and also by swapping the order of iterations. We concluded that the final values of magnitude are insensitive to the initial event locations. The final event locations are also robust, unless there are anomalies in the ground-motion decay pattern (such as a lack of clear ground-motion decay with distance), in which case the final location can vary within a few kilometers.

The initial and final within-event residuals and between-event residuals are plotted as a function of hypocentral distance and magnitude, respectively, for PGA and PGV in Figure 2.6, showing the effects on the vertical component. Results are similar for the horizontal component. The GMPE model is unbiased for both the initial and final residuals. It is clearly seen that the final standard deviation decreases significantly over all distance ranges and all magnitudes.

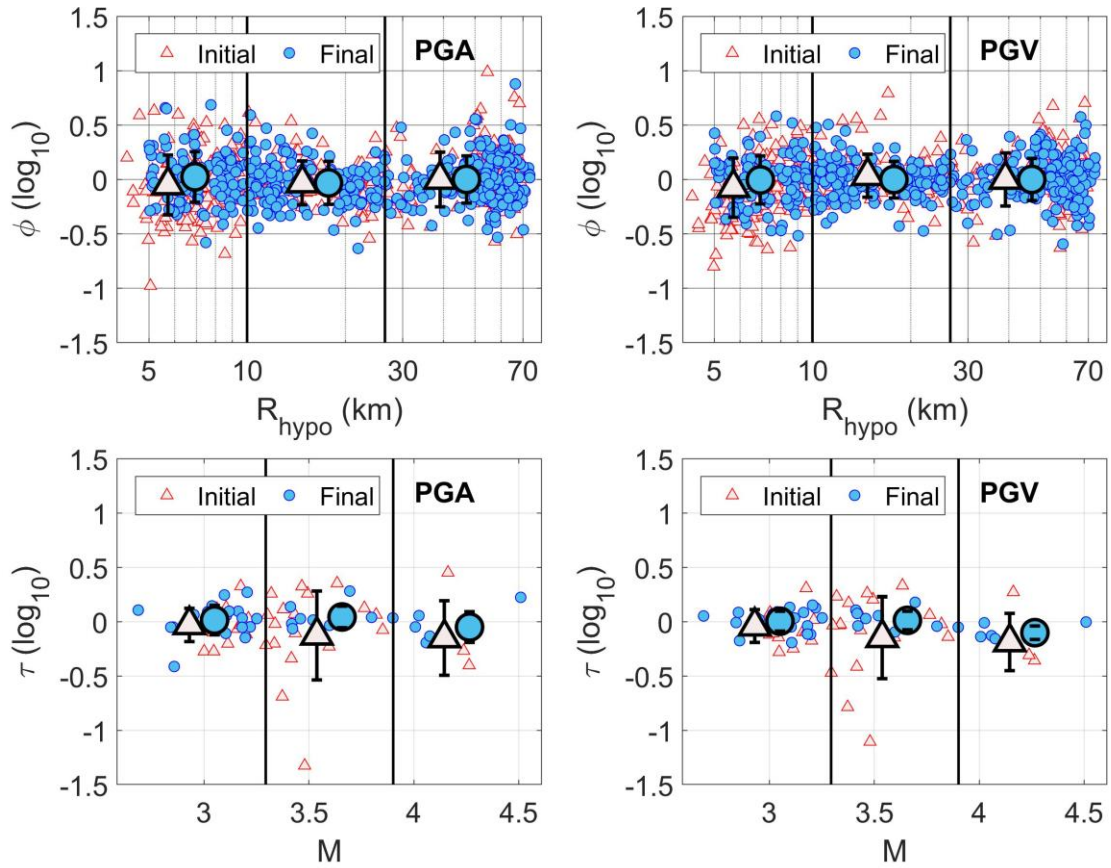


Figure 2.6. The initial (triangles) and final (circles) within-event residuals ϕ (top) and between-event residuals τ (bottom), for PGA (left) and PGV (right), for the vertical component. The data are divided into three bins, with the mean and standard deviation of each bin shown.

2.6 Discussion and Conclusion

Figure 2.7 shows the initial and final variabilities of the six ground-motion parameters as well as the average variabilities, for all records, and for records within 10 km, respectively, for both the vertical and horizontal components. Using the GMC magnitude and location of the earthquakes, the total sigma for all records reduced on average from 0.39 log10 units to 0.24 units on the vertical (or from 0.38 to 0.28 log10 units on the horizontal) – a very significant reduction from a seismic hazard perspective. This implies that much of the calculated GMPE variability may be attributed to uncertainty in source parameters with respect to the values preferred from a ground-motion perspective.

For both the vertical and horizontal components, the final values of the between-event terms for records within 10 km were larger than the corresponding values for all records, probably because the GMC was optimized based on all records out to 70 km. The records were weighted equally, and thus a GMC could be picked that favored the larger distance records if they outnumbered the closer records. This is reflected in the final between-event terms. The within-event term, however, is smaller for the close-distance range (<10 km) in comparison with that calculated for all records, after optimizing the GMC. This reflects the fact that a change in location will have a larger impact at closer distances than at larger distances. Figure 2.8 illustrates how the sigma reductions work, for an individual event. The GMC magnitude shifts the GMPE down to the optimal level for the event, effectively decreasing the between-event term by a significant amount, especially at larger distances. The refinement in location reduces the variability to some extent, but still leaves significant scatter of the residuals around the zero level; thus the reduction in the within-event term is not so significant. Another consideration when it comes to the within-event term, at close distances, concerns the impact of the assumed fixed depth of 5 km. Figure 2.8 also shows the variability that could be achieved by refining the focal depth of the event. For this example, a depth of 6.5 km would reduce the final variability by only a marginal amount. We obtained similar results for the other 37 events; optimizing the focal depth reduces the final values of sigma on average by only 0.005 log10 units.

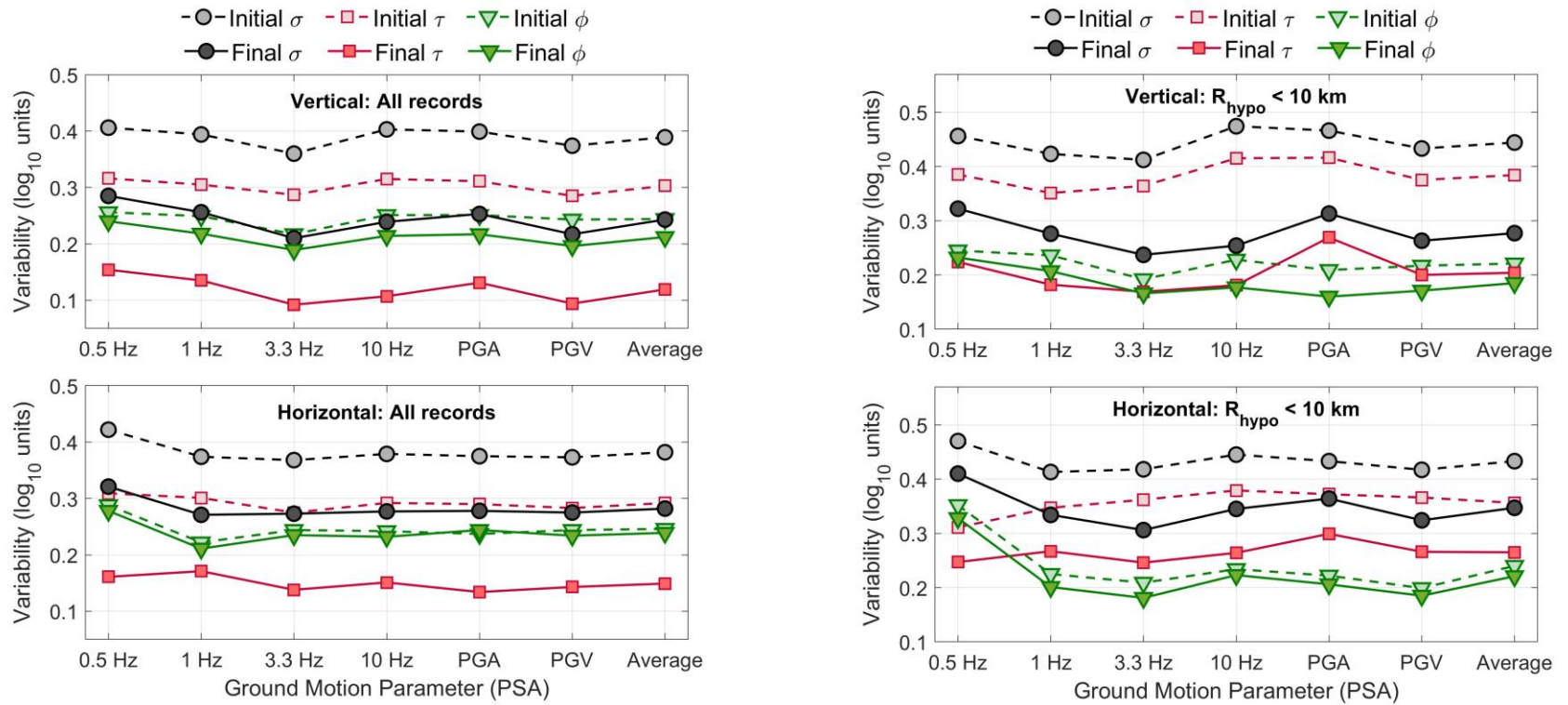


Figure 2.7. Left: Comparison between the initial (dashed lines) and final (solid lines) variabilities for total variability (circles), between-event (squares), and within-event (triangles) terms, for four PSA frequencies (0.5, 1.0, 3.3, and 10 Hz), PGA, PGV, along with the average for the six ground-motion parameters, considering all records within 70 km. (Top) Vertical component and (lower) geometric mean of horizontal components. Right: Same but considering only those records within a hypocentral distance of 10 km.

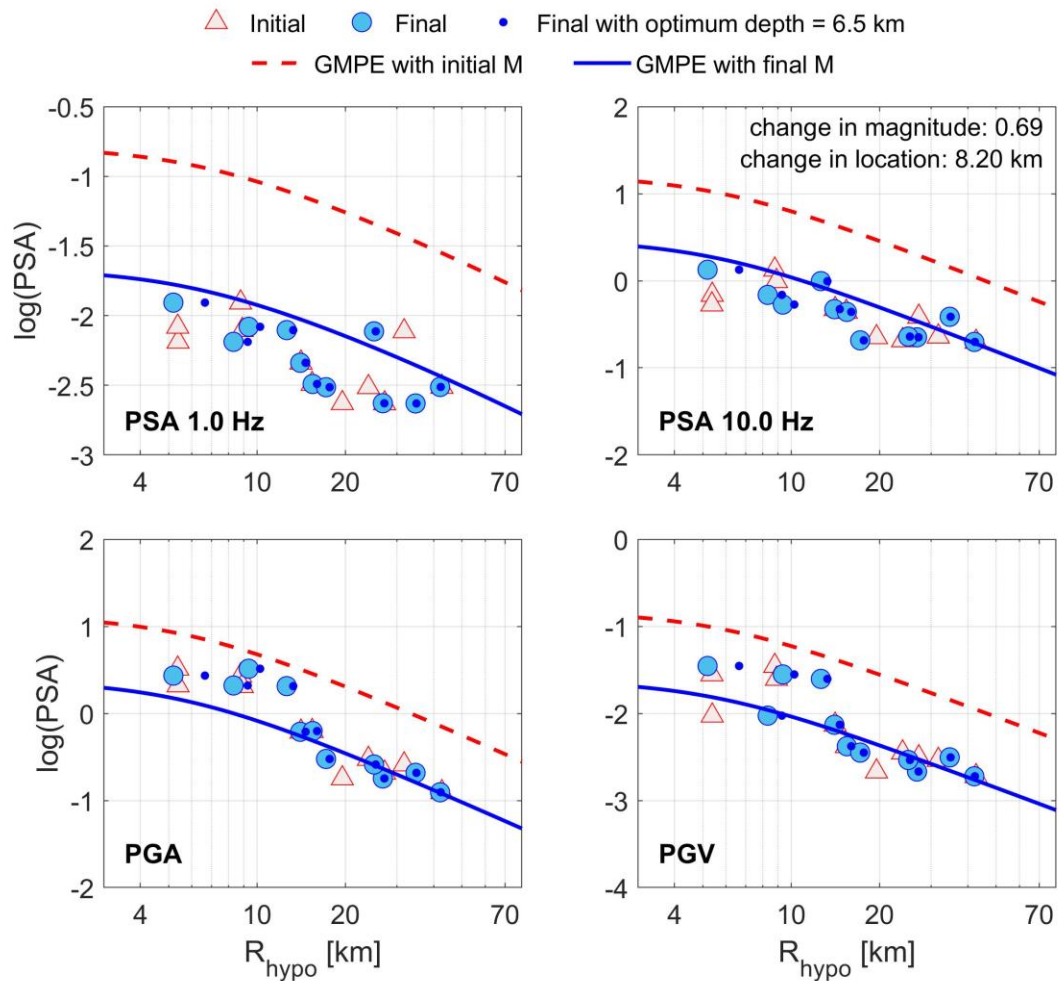


Figure 2.8. Comparison between the recorded PSA values for a single event versus distance for the initial locations (triangles) and the final locations (large circles), along with the zero-biased GMPE, plotted using the initial M (dashed line) and the final M (solid line). The small circles display the final position of the data points if we also optimize the depth of the event.

It has been noted in previous studies that the within-event component of variability tends to be larger than the between-event component (e.g., Bindi et al., 2006; Strasser et al., 2009). Our initial values for the between-event component were rather large (see Figures 2.3 and 2.4), but after iteration, the between-event component is much reduced, and becomes lower than the within-event component, in accordance with other studies. This may suggest significant uncertainty in the initial magnitude estimates, and/or may

reflect the influence of other source effects (such as stress drop) on ground-motion amplitudes.

On average, the GMC was located about 6 km from the epicenter given in the USGS and OGS catalogs, with most GMCs being within 10 km of the epicenter (see Figure 2.5). In contrast, the horizontal location errors given by USGS/OGS for these events are on average 2.3 km. The final GMC magnitudes were within 0.2 units of the initial estimates of moment magnitude for most events, with a few exceptions. In Figure 2.9, we compare the final GMC moment magnitude values with the catalog magnitudes given by the USGS/OGS. The USGS/OGS magnitudes tend to be larger than the GMC moment magnitudes. This could be because the USGS/OGS magnitudes are reported on a variety of magnitude scales, including moment, surface wave, body wave, and local magnitude scales, not all of which may be well calibrated for the event set; the influence of other source parameters on magnitude could also be a factor.

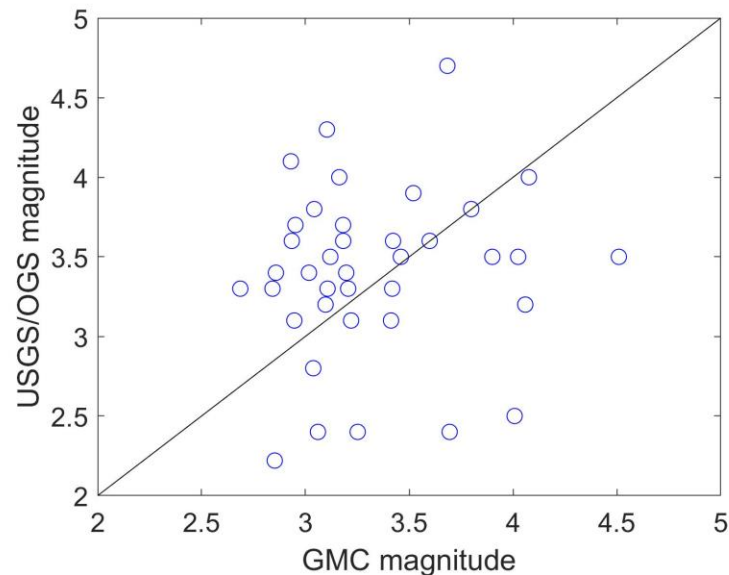


Figure 2.9. A comparison between the final GMC magnitude (moment magnitude) and the catalog magnitudes reported by USGS/OGS.

We conclude that the average residual variability for induced events, for records within 70 km in the CUS, for the vertical component, is 0.21 log₁₀ units for the within-event term and 0.12 log₁₀ units for the between-event term, resulting in 0.24 log₁₀ units for the total sigma variability (corresponding values for the horizontal component are 0.24 and 0.15, for a total sigma of 0.28). To the extent that uncertainties in source parameters are already accounted for elsewhere in a PSHA, they should not be double counted in the aleatory variability in GMPEs. Thus, when defining a sigma model to associate with induced-seismicity GMPEs for use in PSHA, we can remove the contributions that come from source parameters (provided they are already reflected in the epistemic uncertainty model) and avoid double-counting uncertainties. This could be done using the logic tree approach when constructing a PSHA, where the uncertainties of magnitude and location can be specified.

Chapter 3

3 Stress Drops and Directivity of Induced Earthquakes in Western Canada Sedimentary Basin²

In Chapter 3, corner frequencies and stress drops are computed for induced earthquakes in Canada, using the Empirical Green's Function method.

3.1 Introduction

In the Western Canada sedimentary basin (WCSB), the annual number of earthquakes with moment magnitude (**M**) larger than 3 roughly tripled after 2009 (Atkinson et al., 2016), coincident with a sharp increase in oil and gas production. In the WCSB, injection-induced earthquakes are primarily caused by hydraulic fracturing, though there are also cases of wastewater-disposal-induced earthquakes (Schultz et al., 2014). To date, the largest induced earthquakes recorded in the WCSB are two events of **M** 4.6 near Fort St. John (Mahani et al., 2017, 2019). The largest natural earthquakes recorded in the area have had magnitudes between **M** 4.0 and 5.4 (Ristau et al., 2007; Wang et al., 2018). With the increase in earthquakes, a concern has been raised regarding the ground motions from these events and their impact on seismic hazard (Atkinson, Ghofrani, et al., 2015; Atkinson et al., 2017). One approach to gain knowledge of the seismic hazard is to study earthquake source parameters to better understand the underlying processes and their implications for ground-motion generation, specifically the high-frequency parameters stress drop and corner frequency.

As mentioned in Section 1.2.2, stress drop was initially considered primarily as a measure of the total stress release during an earthquake, referred to as the static stress drop, and defined in terms of physical parameters such as the length of the fault and the amount

² A version of this chapter has been published. Holmgren, J. M., G. M. Atkinson and H. Ghofrani (2019). "Stress Drops and Directivity of Induced Earthquakes in the Western Canada Sedimentary Basin", *Bulletin of the Seismological Society of America*, **109**(5), 1635-1652.

of slip. Brune (1970) showed that the corner frequency of the far-field displacement spectrum is related to a length scale that defines the fault size and used this as the basis for his definition of stress. Throughout the rest of this article, we reference Brune's definition of stress drop (including a subsequent modification by Boatwright, 1980). Multiple studies have been conducted comparing stress drop values of tectonic and induced earthquakes. Some find that there are differences (Abercrombie et al., 1993; Hua et al., 2013; Hough, 2014), whereas others find no clear distinction (Tomic et al., 2009; Huang et al., 2016; Ruhl et al., 2017). In ground-motion studies, it has been found that the stress parameter increases with focal depth (Yenier et al., 2015a; Atkinson et al., 2017); induced earthquakes tend to have shallow depths and are thus associated with relatively low stress parameters compared to deeper tectonic events.

Another source parameter that affects the high-frequency content of ground motion is rupture directivity (see Section 1.2.3). Typically, earthquakes exhibiting directivity effects will produce azimuthal variations in the high-frequency content observed at stations (e.g., Spudich et al., 2008). Specifically, the forward rupture direction will yield more high-frequency ground motions than the backward direction. It is common practice to model both large and small earthquakes as circular sources, assuming that the seismic waves propagate symmetrically, with any azimuthal variations averaging out in the determination of source parameters (e.g., Abercrombie, 2014). However, if the region has sparse station coverage, this assumption may not be valid, and stress-drop determinations could be biased by azimuthal effects (e.g., Shearer et al., 2019).

The objective of this study is to compute corner frequencies and stress drops of induced earthquakes in the WCSB. To do this, we use the Empirical Green's Function (EGF) method to isolate source properties of the earthquakes from propagation and site effects. In addition, we investigate rupture directivity characteristics of the earthquakes and their implications. We find stress drops of induced earthquakes in WCSB lie in the same range as corresponding values for tectonic earthquakes. Furthermore, we observe rupture directivity in more than one-third of the events, with some events showing signs of complex rupture processes.

3.2 Database for Study

We search for potential target earthquakes of magnitude (moment or local) above 3 in the WCSB to study using the EGF approach, considering all such events that occurred between April 2013 and March 2019, as listed in three regional catalogs: the Composite Alberta Seismicity Catalogue (<https://www.inducedseismicity.ca/catalogues>, last accessed April 2019), the Geological Survey of Canada catalog (Visser et al., 2017), and the Alberta

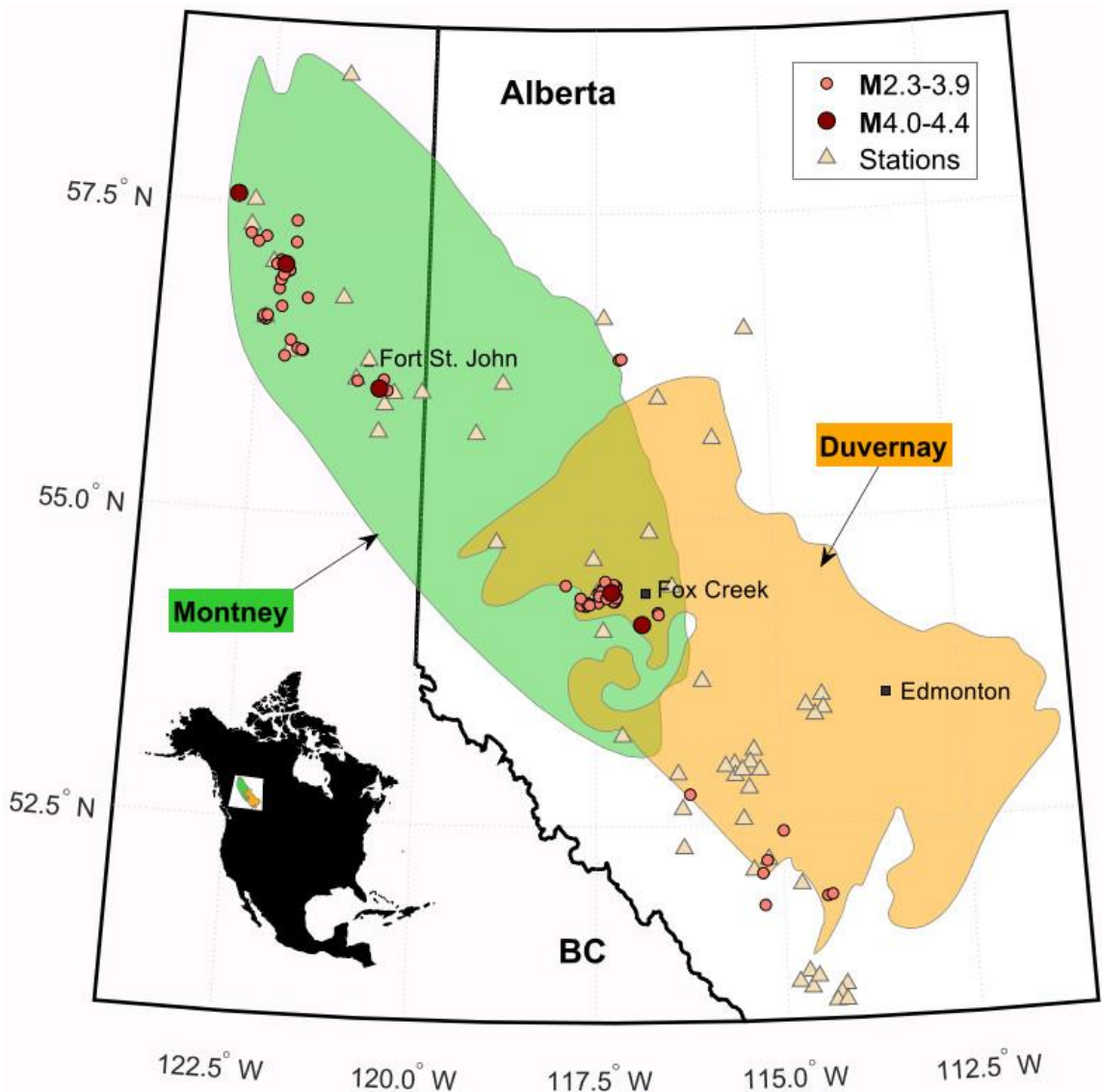


Figure 3.1. Overview map of the Western Canada sedimentary basin (WCSB) and its two main formations Duvernay and Montney. The 87 target earthquakes (circles) between April 2014 and March 2019 and stations (triangles) are shown.

Geological Survey catalog (Stern et al., 2018). We filter our selection considering recording stations that were active and available through Incorporated Research Institutions for Seismology at the time of the earthquakes. Figure 3.1 shows the spatial distribution of the earthquakes and stations. We include data from broadband stations from regional networks, having a sampling rate of 100 Hz. Because the station distribution tends to be sparse in WCSB, especially at the beginning of the search period, we select stations out to distances of 200 km. For the earthquake to be considered as a potential target event for EGF determination, we require at least one station within 80 km. With these criteria, we identify 131 potential target earthquakes that might be investigated using the EGF method described in the Analysis Methods Section.

3.3 Analysis Methods

3.3.1 Spectral Ratios

A technique commonly used to isolate source effects without requiring prior knowledge of the path and site effects is the EGF method, where a smaller earthquake acts as an EGF for a larger earthquake, commonly called the target earthquake (Bakun and Bufe, 1975; Hartzell, 1978; Mueller, 1985; Mori and Frankel, 1990; Abercrombie et al., 2005; Boyd et al., 2017; Wu and Chapman, 2017; Van Houtte and Denolle, 2018). In order for a smaller earthquake to classify as an EGF event, it needs to be collocated to and have similar focal mechanism as the target; the degree to which these criteria are met is usually judged by cross correlation of waveforms. Furthermore, the EGF's magnitude should be sufficiently small compared to that of the target to avoid contamination of the target corner frequency with that of the EGF. If these criteria are met, it can be assumed that the EGF seismogram is approximately a delta function passed through the same path and site transfer function as the target (Mori et al., 1990; Lanza et al., 1999). Therefore, by taking the deconvolution between the target and the EGF, the path and site components are effectively removed, and the source characteristics of the target earthquake can be examined. There are a few different approaches used in the literature, for example, using body waves (Abercrombie, Bannister et al., 2017; Ruhl et al., 2017), coda waves (Mayeda et al., 2007; Wu et al., 2017, 2018), or looking at the source time function (STF) (Mori et al., 1990; Harrington and

Brodsky, 2009). In this study, we follow the approach of Abercrombie (2015) and Abercrombie, Bannister, et al. (2017).

We start by finding EGF events for each identified WCSB target earthquake. Because the seismicity catalogs are incomplete at low magnitudes, we use cross correlation of continuous time series to detect EGF events. For each target earthquake, 10 s of the S wave at the closest station is cross- the same station. We used just the closest station in our event correlated with ± 2 months of continuous waveform data at search because the process of downloading and analyzing months of continuous signal is resource intensive. We only use the S-wave portions of the horizontal components because the EGF earthquakes were too small to have clear P-wave arrivals (i.e., above background noise) for most stations. All time series are bandpassed between 1 and 2 Hz using a two pole, two passes, Butterworth filter, before cross correlation. Our narrow bandwidth of 1-2Hz is chosen to ensure that we are examining signal above the frequency range of the background noise but below the corner frequency of the target event. We avoid use of the higher frequencies, for which the cross correlation tends to degrade (Abercrombie, 2015; Abercrombie, Bannister, et al., 2017). We use the band-pass filtered time series only for the cross-correlation step; unfiltered time series are used in the rest of the analysis. Any time-series segment that has a correlation coefficient (CC) larger than 0.80 and also has signal-to-noise ratio (SNR) > 3 over a bandwidth minimum of 5 Hz, starting at ≤ 1 Hz, is retained as an EGF. Out of the initial 131 potential targets, 116 were found to have > 2 EGF earthquakes (on one or more stations) and were retained for further analysis. These earthquakes are listed in Table S3.1, available in the electronic supplement.

After downloading the target and EGF waveforms at all stations within 200 km, we compute the spectral ratios between target and EGF pairs to investigate the target's source properties. Before spectral ratios are computed, we first ensure that the EGFs fulfill several criteria. Figure 3.2 outlines the procedure. To confirm that the EGF's focal mechanism is similar to the target and that they are collocated, we use cross correlation at each station. Similar to the EGF-detection method, we band-pass filter the waveforms between 1 and 2 Hz using 10 s time windows (Figure 3.2a). We choose 10 s to enhance the signal content

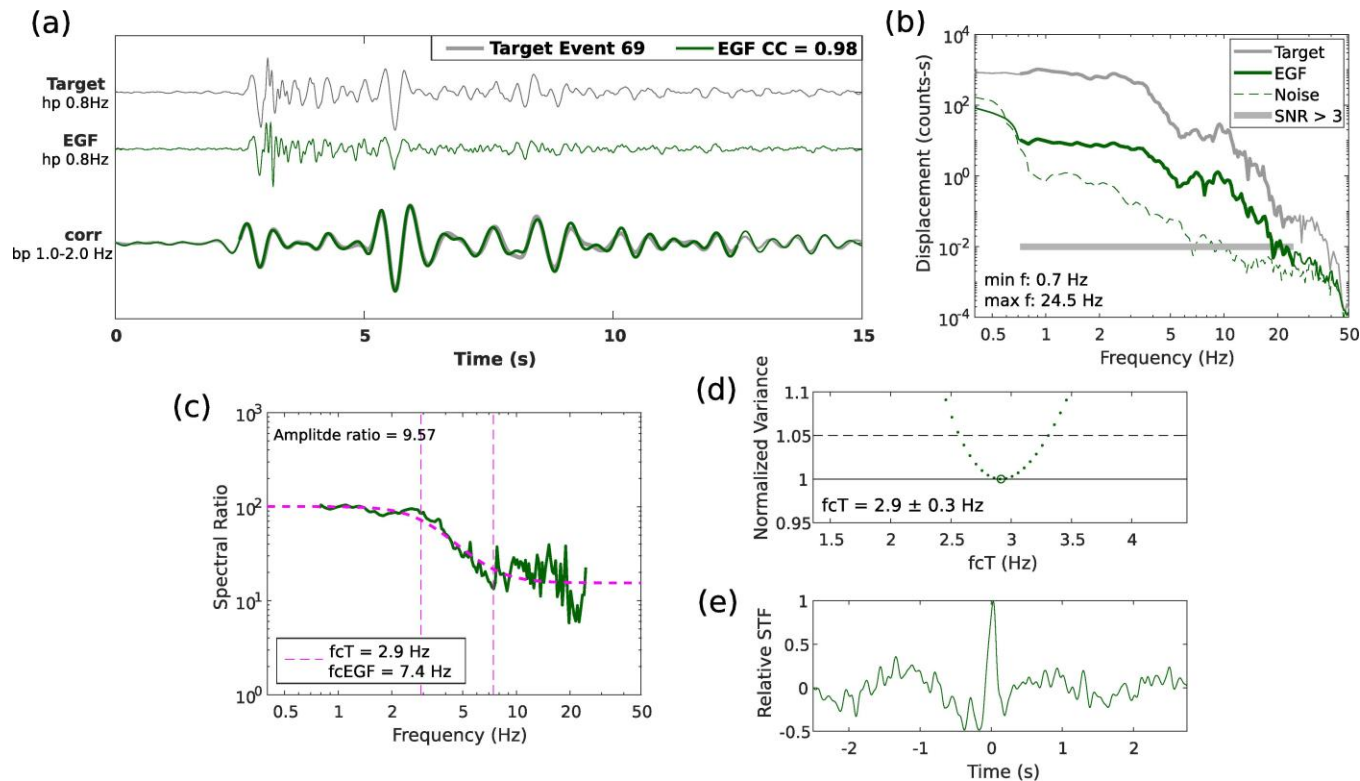


Figure 3.2. Empirical Green’s Function (EGF) method outlined using target earthquake 69 and one of its EGF earthquakes as an example. (a) Waveform time series of the target (light line) and EGF (dark line) used in the cross correlation (corr). The bold line shows the 10 second time window used. A high-pass (hp) filter is applied to the top two seismograms with a corner of 0.8 Hz, and a band-pass (bp) filter with corners 1.0 and 2.0 Hz is applied to the seismograms before cross correlation. (b) Raw displacement spectra (S window) of the target and EGF. The bold horizontal line and the bold spectra lines represent frequency range over which signal-to-noise ratio (SNR) > 3. (c) Spectral ratio between the target and EGF, with the best-fit model plotted on top (dashed line); target and EGF corner frequencies are shown as vertical dashed lines. (d) Variance check of the best-fit model. (e) Relative source time function (RSTF) from deconvolution of the target from the EGF

and to ensure that the whole S wave is captured at the farthest stations (200 km). Abercrombie (2015) reported that EGFs with CC below 0.7 may bias results. However, we found that there was no significant difference in the results when using $CC \geq 0.65$ versus $CC \geq 0.70$ as the minimum correlation criterion, perhaps because of our initial EGF screening requiring $CC \geq 0.8$ at the closest station. In general, most values of the correlation coefficients for EGF events over all stations are about 0.9.

Next, we use the Prieto et al. (2009) multitaper approach to obtain the Fourier amplitude spectra of event pairs that pass the correlation criterion. We use all waveforms having double the frequency bandwidth from the initial EGF search the lowest available frequency must be ≤ 1 Hz (Figure 3.2b). We $SNR \geq 3$ over a minimum frequency band of 10 Hz, where to ensure better quality signals. To avoid data resolution issues and bandwidth limitations, we set the minimum and maximum frequencies to 0.5 and 40 Hz, respectively. Over the bandwidth fulfilling the SNR criterion, we take the spectral ratio between the target and EGF (Figure 3.2c). To ensure that the EGF is of good quality, the spectral ratio must satisfy the following quality controls: (1) the amplitude ratio between the lower and upper frequency portions should be greater than 3 to ensure the shape is adequate for fitting (Ruhl et al., 2017); and (2) the spectral ratio should not be less than 5.6 at frequencies less than 2 Hz, equivalent to a magnitude difference of 0.5 between the target and EGF, to ensure that the EGF is small enough relative to the target to act as a delta function. Some authors required magnitude differences between the target and EGF of at least 1.0 in their studies (e.g., Hartzell, 1978; Huang et al., 2017; Hatch et al., 2018). Others required similar or smaller magnitude differences in comparison to that of this study: e.g. 0.6 (Folesky et al., 2016; Wu et al., 2018); 0.5 (Uchide and Imanishi, 2016; Ruhl et al., 2017); and 0.3 (Clerc et al., 2016). The purpose of the magnitude criteria is to ensure that there is a sufficient difference between the target and EGF earthquakes' corner frequencies, and between their low-frequency amplitude levels. Ideally, the larger the magnitude difference is, the better the resolution will be. On the other hand, the SNR worsens for small earthquakes. Thus, for each dataset a compromise is usually sought to maximize the magnitude difference while keeping enough EGFs for the analysis. Because the WCSB earthquakes tend to have small magnitudes and we are using regional stations out to 200

km, we chose to use 0.5 as the minimum magnitude difference criterion to ensure we have an adequate number of EGFs for the smaller target earthquakes. For study events of $M < 3.5$, roughly 30% of the EGFs (~ 2250 earthquakes) have magnitude differences between 0.5 and 1.0.

Our final quality check of the target–EGF pair is individual spectral fitting. We model the earthquakes as circular ruptures that follow a single-corner source spectrum model, as developed by Brune (1970) following the Aki (1967) omega-square model, and further modified by Boatwright (1980):

$$\Omega(f) = \frac{\Omega_0}{\left[1 + \left(\frac{f}{f_c}\right)^{\gamma n}\right]^{\frac{1}{\gamma}}}, \quad (3.1)$$

in which Ω_0 is the low-frequency plateau below the corner frequency f_c , n is the high-frequency fall-off rate ($n = 2$), and γ is the sharpness of the corner in the source spectra, in which $\gamma = 1$ in the Brune model and $\gamma = 2$ in the Boatwright model. Usually, the sharpness is chosen by determining which value fits the data best (Abercrombie, 2014; Abercrombie, Bannister, et al., 2017; Wu et al., 2018). Huang et al. (2016) compared the two models and found that although the Boatwright model leads to smaller stress-drop uncertainties, it tends to produce lower corner frequencies due to frequency bandwidth limitations. Shearer et al. (2019) found that the Boatwright model tends to fit individual spectra better compared to the Brune model. We selected Boatwright’s model because it has a sharper transition between the low-frequency and high-frequency portions of the model, which fit our spectral ratios better. By taking the spectral ratio between the target and EGF earthquakes, we obtain:

$$\frac{\Omega_T}{\Omega_{EGF}} = \frac{\Omega_{0,T}}{\Omega_{0,EGF}} \left[\frac{1 + \left(\frac{f}{f_{c,EGF}}\right)^{\gamma n}}{1 + \left(\frac{f}{f_{c,T}}\right)^{\gamma n}} \right]^{\frac{1}{\gamma}}, \quad (3.2)$$

in which the subscripts T and EGF represent the target and EGF earthquakes, respectively.

We fit each individual spectral ratio pair to Equation (3.2) using nonlinear least-squares. To check the variance of the fit, we follow the approach of Viegas et al. (2010), where a grid search is performed over $\pm 0.5f_{c,T}$ with $f_{c,EGF}$ and the ratio $\Omega_{0,T}/\Omega_{0,EGF}$ as free parameters. We evaluate the L2 norm at each grid point and compute the variance. We retain the spectral ratio if $f_{c,T}$ is a global minimum and the variance increases as we move away from the solution, such that it exceeds 5% within the $\pm 0.5f_{c,T}$ range (Figure 3.2d).

We also compute the relative source time functions (RSTF) of each target-EGF pair to investigate complexity and directivity effects, using the water-level method to stabilize the deconvolution (Mueller, 1985; Folesky et al., 2016) (Figure 3.2e). Theoretically, a circular source earthquake will have an RSTF that is a simple pulse. If there is rupture directivity, the pulse's duration will be shorter in the forward rupture direction, and longer in the backward direction (Haskell, 1964). Similarly, if the earthquake has complex characteristics, the RSTF will not exhibit a simple pulse shape, but can, for example, be two pulses superimposed (Park et al., 2015).

Our final $f_{c,T}$ for each target is obtained using one of two approaches: (1) stacking and fitting, or (2) directivity analysis (see next section). If there is no evidence of directivity, we follow the first method. In this case, we first normalize the spectral ratios that pass the quality control by the term $\Omega_{0,T}/\Omega_{0,EGF}$ from Equation (3.2), and then stack them by taking the geometrical mean for each frequency bin. The stacked spectral ratio is fit to Equation (3.2) to compute a final $f_{c,T}$ estimate. For the uncertainty analysis, we use a bootstrap resampling technique (Efron, 1979). We resample 70% of the normalized spectral ratios 200 times, restack them, and perform the inversion again. The standard deviation of the resulting $f_{c,T}$ measurements is taken as the error estimate.

3.3.2 Directivity Analysis Based on Haskell Source Model

Over one-third of the target earthquakes have clear variations of station $f_{c,T}$ with azimuth. This was observed both in the corner frequencies and in the RSTF durations. Typically, directivity effects cancel out if individual spectral ratios are stacked over a wide azimuthal range (Abercrombie, 2014). However, because our stations do not provide sufficient

azimuthal coverage, we account for the observed azimuthal variations using a Haskell unilateral source model (Haskell, 1964). We investigate how the mean $f_{c,T}$ for each station varies over azimuth, and we assign a directivity index as follows:

0. Unknown directivity: there are too few azimuthal observations or too much variation between the station $f_{c,T}$ observations to assess directivity.
1. Directivity is observed.
2. No directivity is observed.

Figure 3.3 shows examples of the last two cases. If the target event is assigned a directivity index of either 0 or 2, the final corner frequency is computed through traditional stacking and fitting as described in Section 3.3.1. In order for a target earthquake to be assigned an index of 1 to indicate directivity, there had to be clear $f_{c,T}$ variations in at least two of the four azimuth quadrants, observed on a minimum of three stations. We then compute the final $f_{c,T}$ by inverting a Haskell source model:

$$\tau_i = \tau \left(1 - \frac{V_r}{c} \cos \theta_i \right), \quad (3.3)$$

in which τ is the true duration of the STF, τ_i is the STF duration observed at the i th station, V_r is the rupture velocity, c is the wave velocity, and θ is the angle between the radiated body waves and the i th station. Because we only use S waves and assume V_r is 90% of the S -wave velocity, the term $V_r/c = 0.9$. Following Park and Ishii (2015), we expand the $\cos \theta$ term to also include the rupture dip and take-off angle:

$$\cos \theta = \sin \gamma \sin \gamma_i + \cos \gamma \cos \gamma_i \cos(\phi - \phi_i), \quad (3.4)$$

in which (γ, ϕ) represents the dip and azimuth of the rupture's path along the fault, and (γ_i, ϕ_i) represents the takeoff directions of the earthquake ray from a point on the fault to the site. For simplicity, we assume the take-off angle $\gamma_i = 5^\circ$ for all station observations, because our velocity models and depth uncertainties do not allow us to better define these values. It should be noted that fixing the take-off angle and rupture velocity will likely introduce trade-offs between the rupture dip and the rupture velocity. However this is not critical for our purposes, as the rupture dip is used as a free parameter for model-fitting

purposes, allowing us to resolve the horizontal component of the rupture direction. The trade-off between rupture dip and velocity would be more important if we wished to determine both the horizontal and vertical components of the rupture direction.

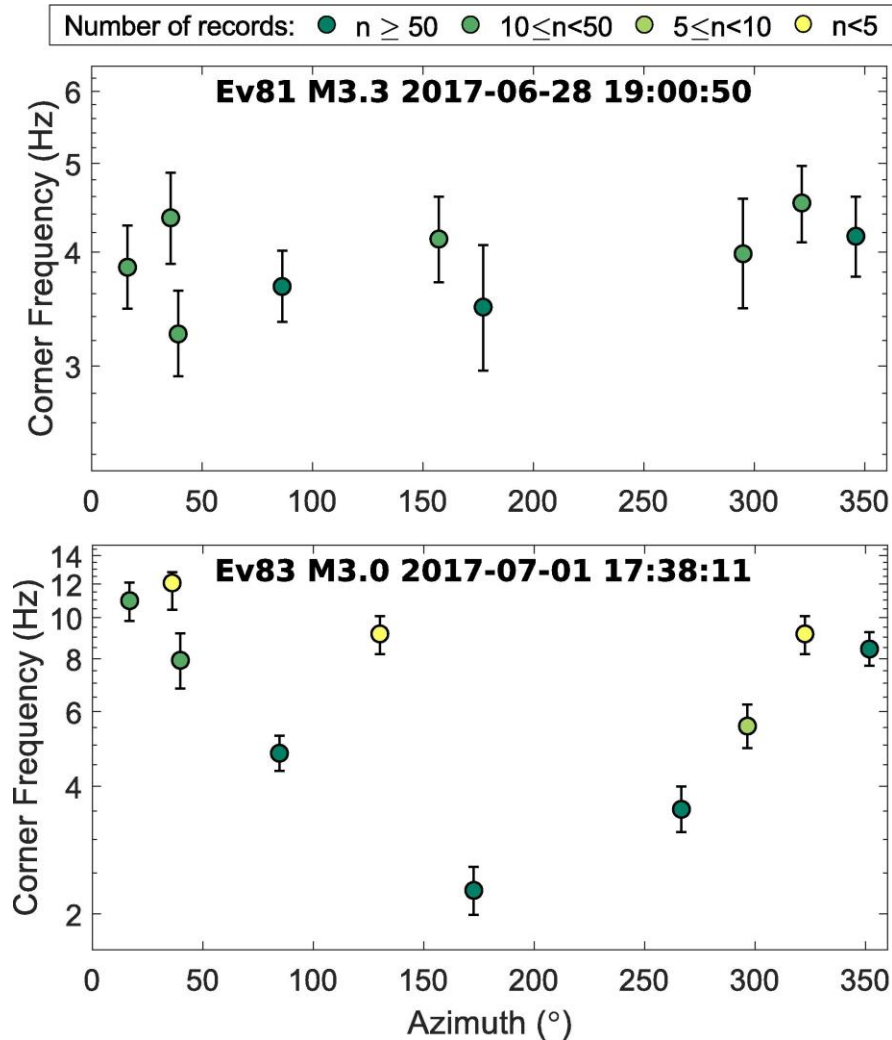


Figure 3.3. A comparison of azimuthal variability of corner frequency between two target earthquakes. Each station mean is shown as a circle, with vertical error bars representing the corner-frequency uncertainty. Darker shaded circles are stations with more records. Event 81 shows no clear azimuthal variation in the station corner frequencies (circles) and was assigned a directivity index = 2. Event 83 displayed a factor of five difference between the largest and smallest corner frequencies, and was assigned a directivity index = 1.

Figure 3.4 outlines our process for quantifying the potential directivity effect. To utilize Equations (3.3) and (3.4), we convert our station corner frequencies to rupture durations using the relationship $\tau = 1/f_c$ (Boore, 1983; Archuleta and Ji, 2016; Van Houtte and Denolle, 2018), then use nonlinear least squares to fit our observations to the model (Figure 3.4a). We apply weights to the stations depending on how many target–EGF pairs are available, with the stations with more observations being assigned greater weight. To estimate the uncertainty in $f_{c,T}$, we use bootstrapping to resample 70% of our target-EGF pairs 200 times; the standard deviation of the mean $f_{c,T}$ is taken as the error estimate (Figure 3.4c). This process also results in determination of the rupture azimuth (Figure 3.4d).

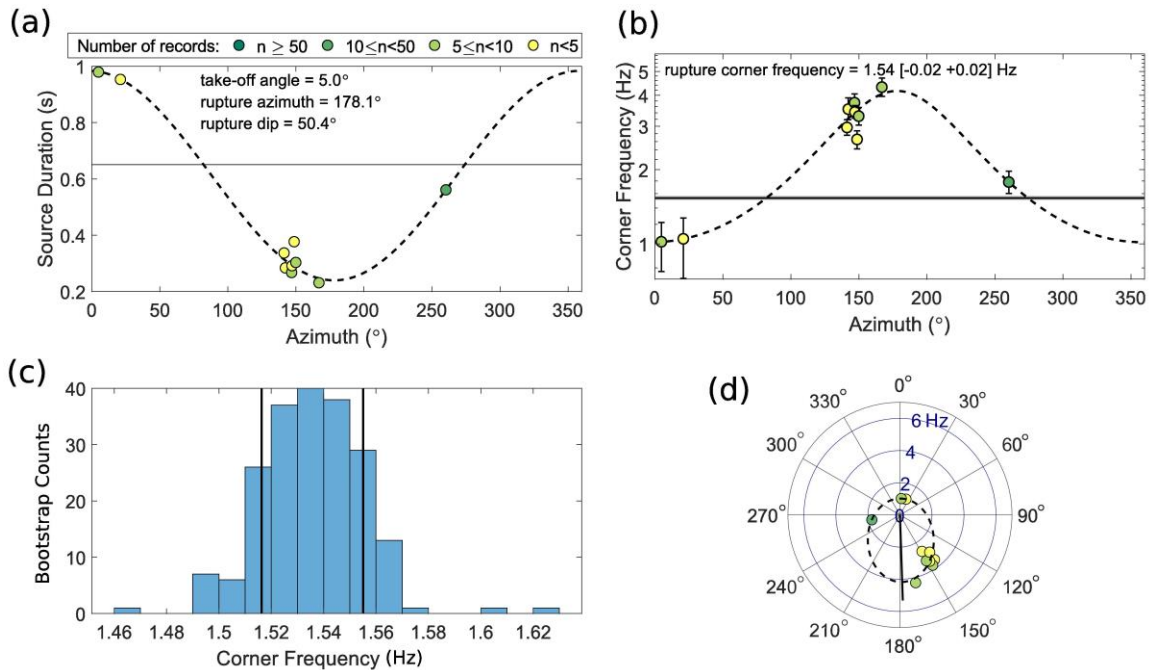


Figure 3.4. Overview of the directivity evaluation process (event 29). (a) After the station corner frequencies are converted to source rupture durations (circles), a best-fit Haskell model is determined. The horizontal line shows the true source duration. (b) Similar plot as (a), but now in terms of corner frequency. The horizontal line shows the rupture corner frequency, with the uncertainty indicated by the width of a lighter shaded line behind. (c) Bootstrap analysis, with plus or minus standard deviation shown as two vertical, solid lines. (d) A polar plot of the station corner frequencies (circles), model (dashed line), and model rupture azimuth (solid line).

3.3.3 Moment Magnitude Computation

The magnitudes listed in catalogs include both moment and local magnitudes as computed by three different agencies (see Section 3.2). To unify the magnitudes, we computed the moment magnitudes from the displacement spectra. We correct the displacement spectra of the target events for instrument response, then use Equation (3.1), including a path attenuation term expressed using the quality factor Q (Brune, 1970; Boatwright, 1980):

$$\Omega(f) = \frac{\Omega_0 e^{-\frac{\pi f t}{Q}}}{\left[1 + \left(\frac{f}{f_{c,T}}\right)^{\gamma n}\right]^{\frac{1}{\gamma}}}, \quad (3.5)$$

in which t is the travel time. We assume the Boatwright form of the source model with $\gamma = 2$ and $n = 2$. We fix the corner frequency using the results from the spectral ratio step, where $f_{c,T}$ is the mean corner frequency observed at each station. For simplicity we use a frequency-independent anelastic attenuation and set $Q = 1000$, which is a typical regional value in the frequency range of interest (Clerc et al., 2016). We apply Equation (3.5) at low frequencies to retrieve the displacement low-frequency spectral plateau Ω_0 , for each station using nonlinear least-squares.

Finally, we compute the seismic moment M_0 , using the Brune (1970) relation:

$$M_0 = \frac{4\pi\rho\beta^3 G(r)\Omega_0}{FU_{\phi\theta}}, \quad (3.6)$$

in which M_0 is in N·m. For the constants in Equation (3.6), F is the free-surface amplification parameter ($F = 2$, assuming 0° incidence angle) (Boore, 1986), and $U_{\phi\theta}$ is the mean radiation pattern ($U_{\phi\theta} = 0.63$ for S waves) (Aki et al., 1980). We assume a constant hypocentral depth of 4 km, for which the S-wave velocity $\beta = 3200 \text{ m}\cdot\text{s}^{-1}$ and density $\rho = 2600 \text{ kg}\cdot\text{m}^{-3}$ (Chen et al., 2015; Wang et al., 2018). This is in agreement with the typical depth of 3-4 km for induced events in the region (e.g., Zhang et al., 2016; Mahani et al., 2017; Schultz et al., 2017; Eaton et al., 2018; Wang et al., 2018). For the geometric spreading term $G(r)$, we use a bilinear model (Yenier et al., 2015a):

$$G(r) = \begin{cases} r^{1.3} & r \leq 50 \text{ km} \\ 50^{1.3} \times \left(\frac{r}{50}\right)^{0.5} & r > 50 \text{ km} \end{cases}, \quad (3.7)$$

in which r is taken as the epicentral distance. We include stations with $r \leq 100$ km to compute the magnitude to minimize attenuation effects. To calculate the final magnitude for a target earthquake, we take the mean of moment magnitudes computed over all stations \mathbf{M}_{sta} , which is computed from the seismic moment as (Hanks et al., 1979):

$$\mathbf{M}_{sta} = \frac{2}{3} \log M_0 - 6.03. \quad (3.8)$$

To quantify the sensitivity of \mathbf{M} to the assumed Q , we also perform the inversion of Equation (3.5) using $Q = 500$ and 1500 . The lower Q -value would increase \mathbf{M} by about 0.05, whereas the higher Q -value would decrease it by about 0.01 units. The sensitivity to Q is small in comparison to the average interstation \mathbf{M}_{sta} standard deviation of 0.13, which ranges from 0.01 to 0.34. Moreover, the effects of Q are small relative to those of the assumed geometric spreading model. Figure A3.1 shows typical interstation variation of \mathbf{M}_{sta} for a target earthquake.

3.3.4 Stress-Drop Computation

We compute the stress-drop values using the Eshelby (1957) ellipsoidal source model modified for a circular crack:

$$\Delta\sigma = \frac{7}{16} \frac{M_0}{r^3} \times 10^{-6}, \quad (3.9)$$

in which $\Delta\sigma$ is in MPa, M_0 is in N·m, and r is the fault radius in meters. We assume a circular crack to compute the value of r from the corner frequency of the radiated S -wave spectrum (Brune, 1970):

$$r = \frac{k\beta}{f_{c,r}} \quad (3.10)$$

in which $\beta = 3200 \text{ m}\cdot\text{s}^{-1}$ (assuming 4 km depth) and the value of k depends on the theoretical source model used to relate the corner frequency to the rupture radius. Several earthquake source models have been proposed in the literature (e.g., Brune, 1970; Sato et al., 1973; Madariaga, 1976; Kaneko et al., 2014). In this study, we adopted Madariaga's (1976) value of $k = 0.21$ for S-waves, assuming a rupture speed of $V_r = 0.9\beta$. However, it should be noted that the calculated stress-drop values will differ significantly depending on which model is used. For example, using the Brune (1970) $k = 0.37$ for S waves would result in a stress drop ~ 5.5 smaller than the value computed using Madariaga's value of k . Hence, stress drops should only be compared between studies that use the same source model conventions and equations.

3.4 Results

Of the 116 considered target earthquakes, 87 had at least five target–EGF pairs that passed all the quality controls (see Table S3.1). Figure 3.5 shows the corner frequencies obtained, divided into the directivity categories. Of the final 87 target events, 37 had too few data or too much variation to determine an azimuthal station $f_{c,T}$ trend (directivity index = 0), 37 targets showed clear variation with azimuth (directivity index = 1), and 13 had no apparent azimuthal variation (directivity index = 2). The scatter in corner frequencies versus seismic moment is in agreement with that reported in a similar study for events in Oklahoma (Wu et al., 2018). The subgroup with no apparent directivity tends to plot nearer the high end of the range of stress-drop values (Figure 3.5c). The subgroup with unknown directivity has the largest scatter (Figure 3.5a); for this case, we assumed that there was no directivity for purposes of determining the average corner frequency. For earthquakes having rupture directivity, the largest station $f_{c,T}$ was on average four times larger than the smallest station $f_{c,T}$, and in one extreme case almost eight times larger. This means there is much greater uncertainty in the stress drop for the events with unknown directivity, and this is reflected in the scatter of estimates. If we have measurements only from the forward or backward directions of the fault, we could be miscalculating the corner frequency by a factor of 2 on average, leading to stress-drop errors of a factor of 8. Hence, stress-drop estimates are especially unreliable if determined from stations with a limited azimuthal range.

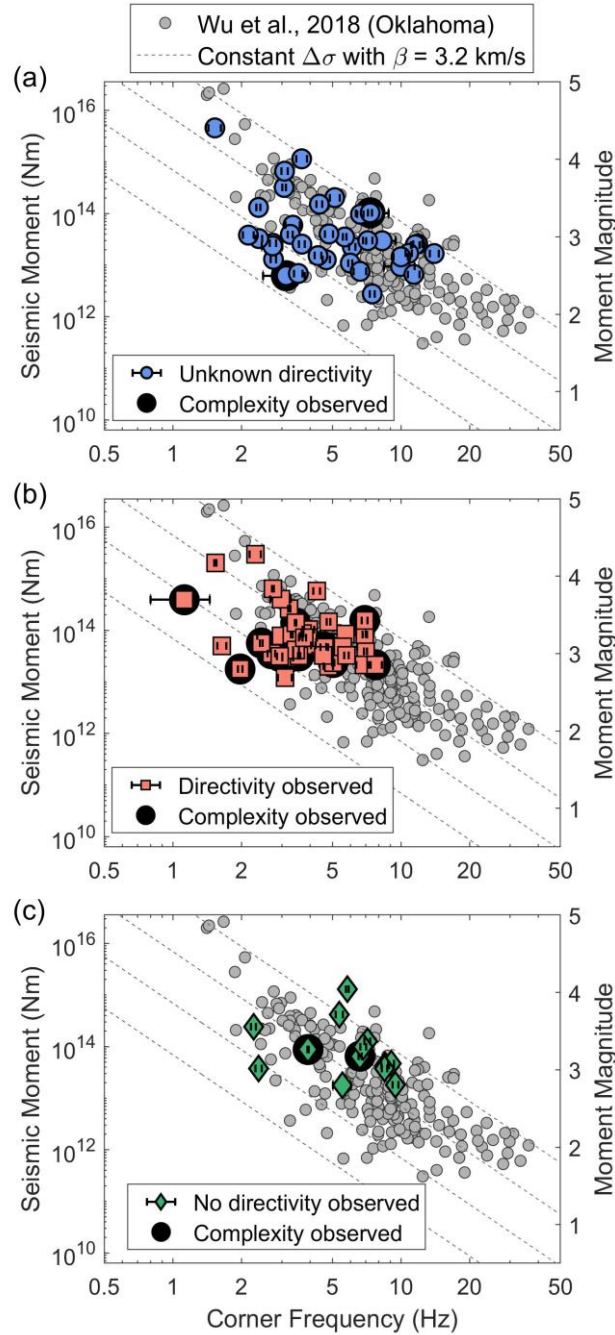


Figure 3.5. Corner-frequency results for target events with directivity index of (a) 0, (b) 1, and (c) 2. The complex targets are highlighted using a black circle. Error bars representing the standard error of the mean are shown as horizontal lines for each marker. Constant stress-drop lines outline 100, 10, 1, and 0.1 MPa, from top to bottom, computed using the Madariaga (1976) k -value and $\beta = 3200 \text{ m}\cdot\text{s}^{-1}$. Small circles in background show results from the Wu et al. (2018) study for comparison.

We identified 19 target events displaying source complexity, as evidenced by deviations from a typical omega-square model in either the stacked RSTF or spectral ratios. These are highlighted in Figure 3.5. A comparison of the characteristics of a simple event with unilateral rupture and a complex event is shown in Figures 3.6 and 3.7. The unilateral event (Figure 3.6) displays variation in RSTF duration with azimuth, whereas the complex event (Figure 3.7) exhibits a double pulse at certain azimuths, which could be interpreted as two subevents within the rupture. The complex event also shows clear deviation from the spectral ratio model (Equation 3.2).

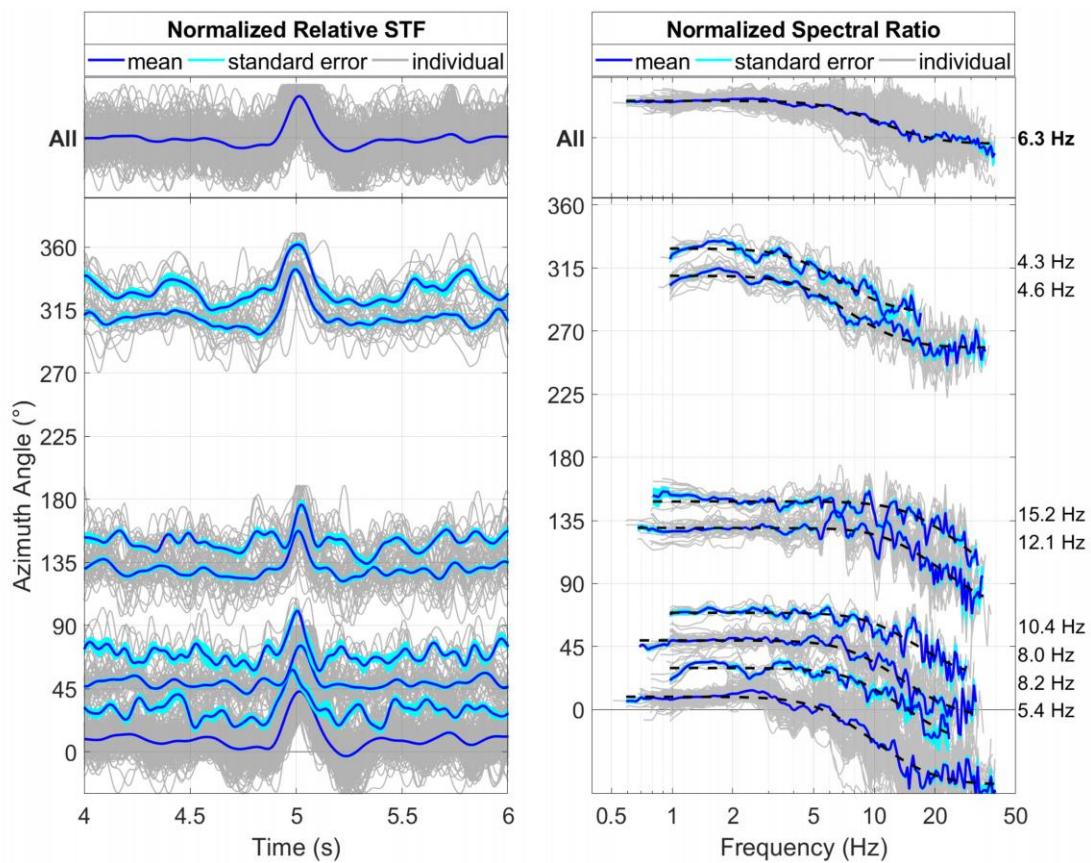


Figure 3.6. Example of a unilateral rupture earthquake (event 107). (a) Normalized RSTF and (b) normalized spectral ratios are shown varying with station azimuth. The azimuths are binned by intervals of 20° . The top stack shows all the individual records stacked. The average over each azimuthal interval is shown as a dark line with its standard error width indicated by a lighter shaded line behind. Dashed black lines are the fitted spectral ratios, with the resultant corner frequencies displayed on the right.

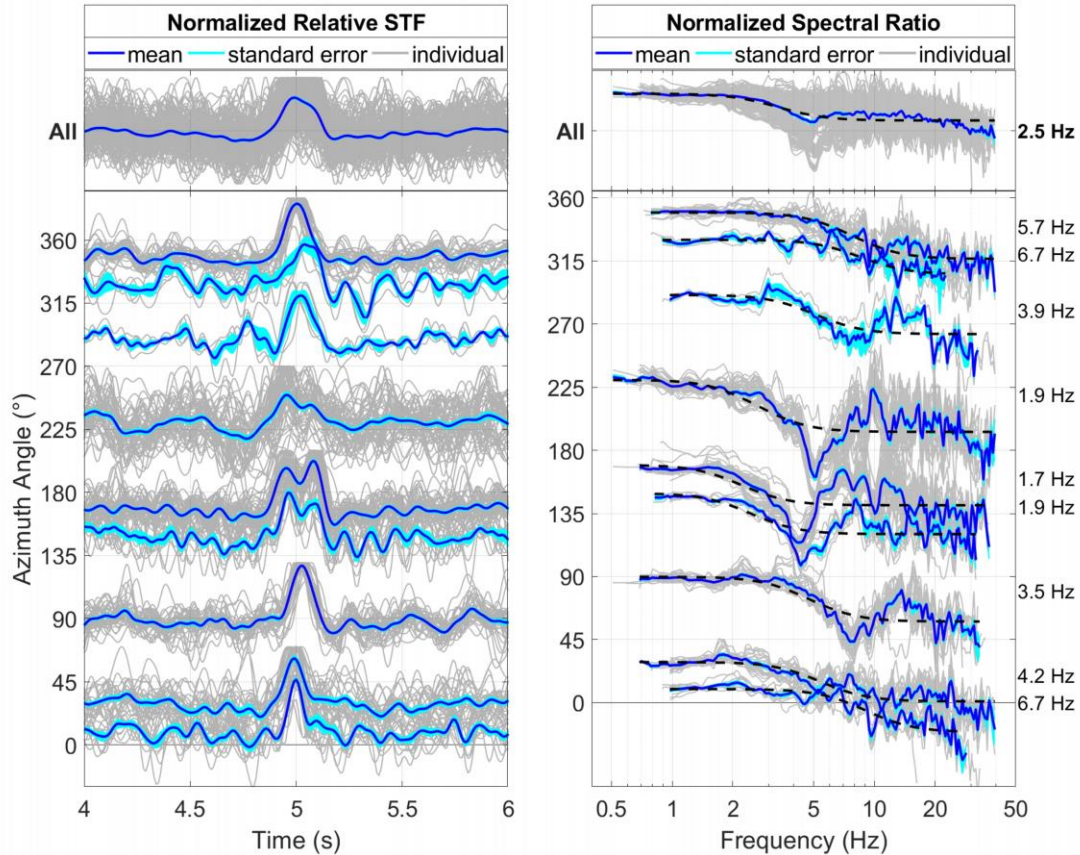


Figure 3.7. Example of a complex rupture earthquake (event 87), with the same figure description as Figure 3.6.

Our directivity analysis yielded rupture direction azimuths for 37 of the target earthquakes. An overview of the spatial distribution of these earthquakes and their rupture directions is shown in Figure 3.8. The events primarily display north and south directivity, indicating that faults striking approximately north–south are prevalent in the region, notably near Fox Creek, where most of our target earthquakes are located (Figure 3.8b). Considering a maximum compressive horizontal stress (S_{Hmax}) oriented northeast–southwest in the region (Reiter et al., 2014), and a preferred fault orientation of $S_{Hmax} \pm 30^\circ$ for reactivation, assuming typical frictional values (Anderson, 1905; Sibson, 1985), faults oriented approximately north–south would be near the optimally oriented range in the current regional stress field and thus more likely to rupture. Schultz et al. (2017) used moment-tensor inversions to study earthquakes in the Fox Creek area and found primarily strike-slip focal mechanisms with north–south strike directions. Nine of our target events

were also studied in the Wang et al. (2018) full moment-tensor analysis and the resultant nodal planes for the double-couple (DC) components are provided for comparison in Figure 3.8c. Most of their study events had primarily strike-slip focal mechanisms, with the exception of the thrust earthquake (event 4). Only one event (event 15) shows a rupture direction that deviates from one of the fault planes significantly. Zhang et al. (2019) reported a deviation from the regional stress field with a local S_{Hmax} of N60.4° E near Fox Creek, based on moment-tensor inversion of induced earthquakes recorded on a local borehole array surrounding a hydraulic fracture well. Interestingly, their $M > 1.5$ study events also ruptured on approximately north-south-oriented faults, even though this is outside the optimal orientation range with respect to the local S_{Hmax} . For activation of north-south-oriented faults, they estimated a required pressure increase of $\sim 12 \pm 4$ MPa and linked the likely pressure source to the nearby fluid injections. Thus, although approximately north-south faults are optimally oriented with respect to the regional stress field, they might not necessarily be optimally oriented with respect to some of the local stress fields. The Zhang et al. (2019) study highlights the possible underlying role of pore pressure increase when it comes to larger induced earthquakes, and how even non-optimally oriented faults can rupture under the right conditions.

When combined with focal mechanisms, directivity is an effective diagnostic to distinguish the fault plane from the auxiliary plane. However, some of our events displayed no obvious azimuthal variation in corner frequency. This could be due to several reasons. Some events may have been a better approximation of an ideal point source than others, in terms of their radiated waves. For example, if the rupture propagated uniformly from the hypocenter in all directions of observation (or nearly so), there would be no apparent directivity effects. Moreover, if the rupture is composed of multiple subevents rupturing in opposite directions, variations with azimuth might not be obvious, because waves from the subevents might interfere destructively with one another (Park et al., 2015; Folesky et al., 2016).

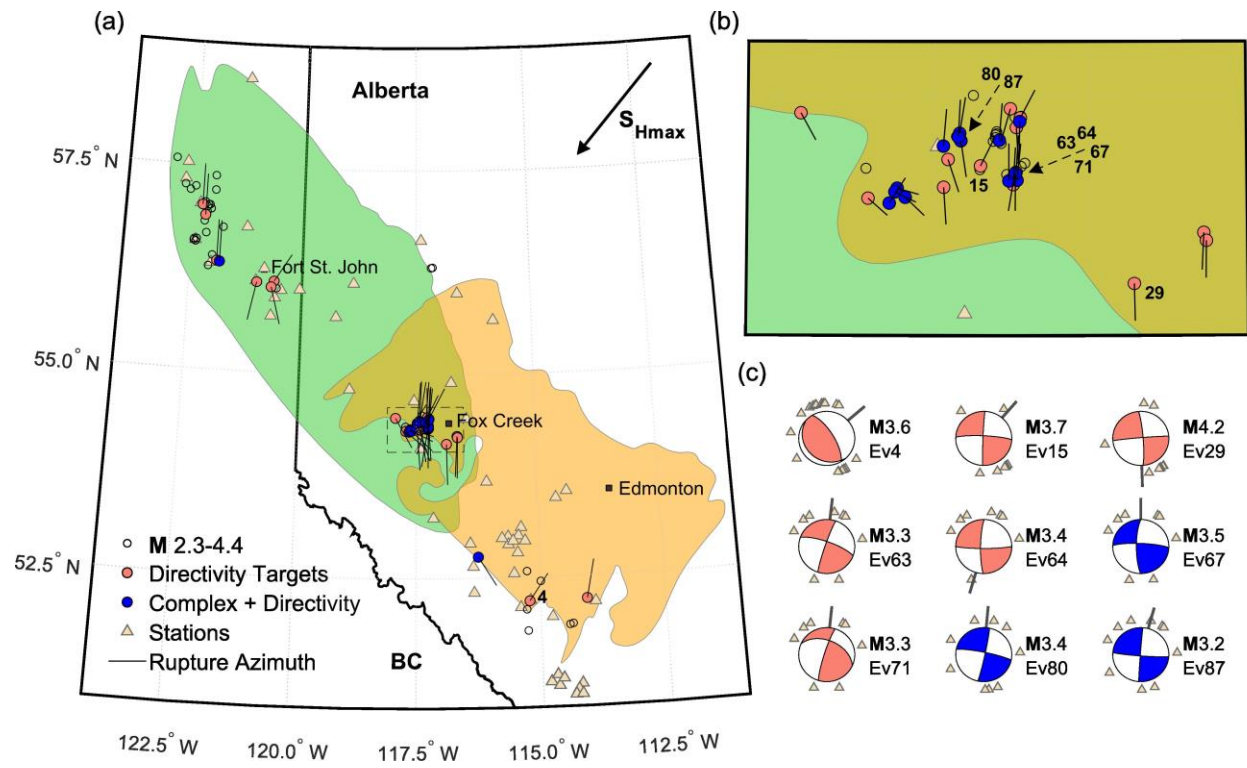


Figure 3.8. Spatial distribution of target earthquakes with observable rupture directivity (circles). The complex directivity events have darker shading. The rupture azimuth for each target is displayed as a solid line extending from the circle. (b) Zoom-in of the Fox Creek area, shown with a dashed rectangle in (a). (c) Double-couple nodal planes from Wang et al. (2018) for nine target earthquakes, along with the station azimuths (triangles surrounding the focal mechanisms). The rupture azimuths obtained in this study are shown with thicker solid lines; darker shading indicates complexity. All earthquakes involved primarily strike-slip faulting, except for event 4, which has thrust-fault focal mechanisms.

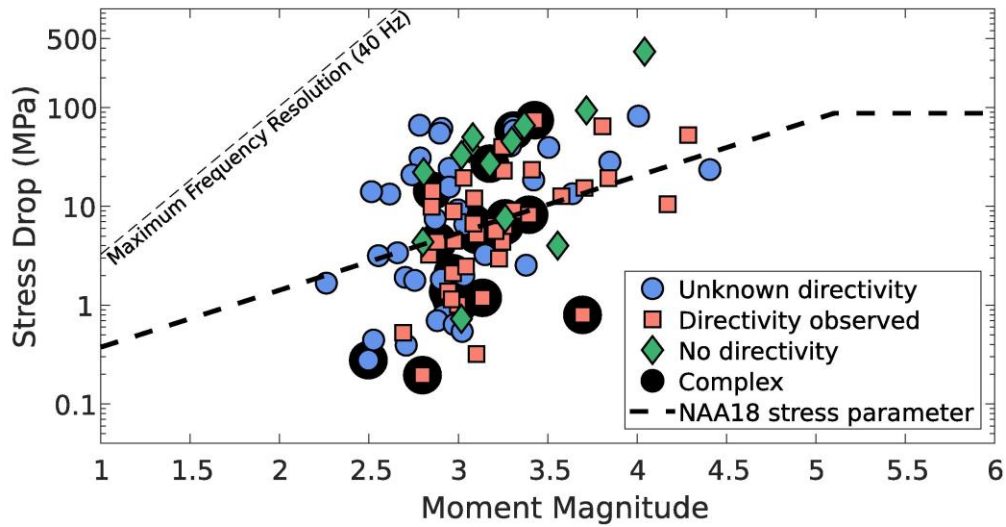


Figure 3.9. Stress-drop values versus moment magnitude. Circles are events with unknown directivity due to data sparseness or too much variability; squares are events with observed directivity; diamonds are events with no observed directivity. The complex targets are highlighted with black circles. The Madariaga (1976) k -value and $\beta = 3200 \text{ m}\cdot\text{s}^{-1}$ are used for all earthquakes. Dashed line shows the stress parameter value obtained by Novakovic et al. (2018) for induced earthquakes in Oklahoma based on regression of ground-motion data, after converting their corner frequencies to this study’s model constants.

Figure 3.9 displays the estimated stress-drop values as a function of magnitude, with different markers for each directivity subgroup. Calculation of moment magnitudes for the target events resulted in a range from M 2.3 to 4.4. For events with known M from moment-tensor solutions, we found good agreement between estimates (see Table 3.1). Combined, WCSB stress drops were on average 7.5 ± 0.5 MPa, varying mostly between 0.2 and 98 MPa, with one extreme event at 370 MPa (see the Discussion Section for more on this earthquake). Within subgroups, the average stress drop was 6.8 ± 1.1 MPa for the unknown directivity targets (directivity index = 0), 5.7 ± 1.0 MPa for the targets with directivity (directivity index = 1), and 22.5 ± 1.1 MPa for the targets with no observed directivity (directivity index = 2). Folesky et al. (2016) found magnitude dependence in rupture directivity for geothermal induced earthquakes, where directivity was only seen for events larger than $M_L \sim 1$. In our case, we observed directivity in all magnitudes, though

our lowest target magnitude is **M** 2.3. When assuming a constant velocity, the stress drops show an increasing trend with magnitude that is in good agreement with that obtained by Novakovic et al. (2018) for induced earthquakes in Oklahoma, as shown in Figure 3.9. The Novakovic et al. study used regression to a seismological model to find the average value of stress parameter that is consistent with ground-motion amplitude data and its scaling with magnitude. To enable comparison with our results, their values of stress parameter were converted to corner frequency, then to the values of stress drop consistent with the conventions and physical constants used in this study (Madariaga's k and $\beta = 3200 \text{ m}\cdot\text{s}^{-1}$).

Table 3.1. Comparison between moment magnitudes obtained from displacement spectra and moment magnitudes from published moment tensor analyses.

Event ID	Date and Time	Moment Magnitude (this study)	Published Moment Tensor Magnitude
3	2014/08/04 17:17:24	4.41	4.0 ¹
4	2014/08/09 15:28:48	3.60	3.6 ¹
15	2015/01/14 16:06:23	3.71	3.5 ¹
18	2015/01/23 06:49:18	3.73	3.7 ¹
29	2015/06/13 23:57:52	4.18	4.1 ¹
31	2015/08/17 20:15:00	4.02	4.40 ²
51	2016/01/12 18:27:22	4.06	4.07 ²
60	2016/11/10 03:05:54	2.82	3.04 ²
63	2016/11/25 05:31:24	3.27	3.31 ²
64	2016/11/25 21:24:00	3.43	3.39 ²
67	2016/11/29 10:15:25	3.45	3.51 ²
70	2016/12/06 01:05:05	3.19	3.18 ²
71	2016/12/07 10:11:37	3.26	3.25 ²
80	2017/06/25 22:56:32	3.41	3.33 ²
87	2017/08/03 00:57:30	3.15	3.02 ²

¹Zhang et al. (2016), ²Wang et al. (2018). A depth of 4 km is assumed for all earthquakes. The Event ID column refers to the Target ID column in Table S3.1. The Date and Time column is given in the format yyyy/mm/dd hh:mm:ss.

3.5 Discussion

There have been two previous studies investigating stress-drop values for the WCSB. Clerc et al. (2016) studied induced earthquakes (M 1.8–4.6) near Fox Creek using the spectral ratio method and determined a range of stress-drop values between 0.1 and 149 MPa. Zhang et al. (2016) studied eight of the largest induced earthquakes in WCSB (M 3.2–4.4) by modeling individual earthquake spectra directly with Brune’s displacement spectral model and found stress drops within the 2–90 MPa range. We have six events in common with Zhang et al. (2016) and our stress-drop values are on average 1.8 times larger. Ide et al. (2003) compared stress drops obtained from single event spectral analysis versus those obtained using spectral ratios and reported that the EGF estimates tend to produce higher corner frequencies and stress drops. Kwiatek et al. (2014) compared the two methods and found that single event spectral analysis resulted in a larger scatter of stress drops. Both papers attribute the difference in results to trade-offs between path and site effects and corner frequency. Methods based on analysis of single spectra are more sensitive to the assumptions on path and site effects, which is what the EGF method aims to avoid. Our results fall within the general range of stress-drop values reported by both Clerc et al. (2016) and Zhang et al. (2016). However, it should be noted that these are large ranges, and they are typical for stress-drop studies in many regions (e.g., Huang et al., 2017). Furthermore, the large ranges observed could be due to limitations of the analysis, including uncertainty in the assumed source model, the limited frequency bandwidth, or the quality of the EGF earthquakes (e.g., Abercrombie, 2014; Van Houtte and Denolle, 2018).

Induced earthquakes in Oklahoma contain more high-frequency energy in their observed ground motions in comparison to their counterparts in the WCSB (Kaski and Atkinson, 2017; M. Novakovic et al., unpublished manuscript, 2019). It has been speculated that this may represent primarily site effects, as the WCSB tends to contain softer sites (Farrugia et al., 2017), which dampens ground motions at higher frequencies (e.g., Van Houtte et al., 2011). It has also been suggested that the shallower depth of WCSB events relative to those in Oklahoma may play a role (M. Novakovic et al., unpublished manuscript, 2019). Wu et al. (2018) used the spectral ratio method to compute corner

frequencies and stress drops for four induced seismicity clusters in Oklahoma. For the corresponding magnitudes, our corner frequencies are comparable to theirs, indicating that the relatively low high-frequency content in WCSB ground motions are probably not a source property, but rather a propagation or site property of the region.

Stress drop scales with the cubed velocity, as can be seen from Equations (3.9) and (3.10). Because shear-wave velocity increases with depth, stress-drop estimates are sensitive to the assumed earthquake focal depth. The available station coverage in the WCSB (for public stations) has large azimuthal gaps and is too sparse for reliable hypocenter determination – more than 90% of our target earthquakes did not have any stations within 30 km. Because the most common depth for induced earthquakes in the WCSB is between 3 and 4 km (e.g., Eaton et al., 2018; Wang et al., 2018), we assumed a constant depth of 4 km for all studied events. Based on the Chen et al. (2015) velocity model derived for central Alberta using shear-wave velocity inversion, and later modified by Wang et al. (2018) to provide more detail at shallow depths, we assumed S-wave velocity and density values of $3200 \text{ m}\cdot\text{s}^{-1}$ and $2600 \text{ kg}\cdot\text{m}^{-3}$, respectively. These assumed constants are embedded in the average stress-drop estimate of 7.8 MPa. If we instead assign a depth of 3 km for all earthquakes, we would assume $\beta = 2300 \text{ m}\cdot\text{s}^{-1}$ and $\rho = 2400 \text{ kg}\cdot\text{m}^{-3}$ and the corresponding average stress drop would be only 2.7 MPa, if we also revise the estimated moments to be consistent with these values (i.e., Equation 3.6). Hence, the value of stress drop is highly sensitive to the assumed velocity at the hypocenter, which is in turn highly sensitive to focal depth. Even if we had an ideal velocity model and incorporated local model variations for the different WCSB regions, unbiased stress drops would be difficult to obtain because the event depths are not known with sufficient accuracy. A rationale for our choice of 4 km for the average focal depth is that it provided better agreement between our moment magnitudes and the published values based on regional moment-tensor solutions; the difference between our moment magnitudes and published values is 0.02 units for the assumed depth of 4 km but would increase to 0.29 units if we revised the velocity to that corresponding to a depth of 3 km.

On the other hand, it is common for moment magnitudes to be obtained from other sources in EGF studies such as published catalogs or focal mechanism studies (e.g.,

Courboux et al., 2016; Ruhl et al., 2017; Wu et al., 2017). As a further exercise, we assume our moments computed using the 4 km depth velocity and density are correct (because they agree with regional moment tensors) and only change the velocity used in the stress-drop computation to the 3 km equivalent. In this case, the average stress drop increases from 7.8 to 21.0 MPa.

The dramatic variations in values obtained for the stress drop depending on the assumed velocity-depth model provide further support for the argument that the absolute values of the obtained stress drops are not meaningful. We suggest that corner frequency should be taken as the basic source parameter that is being determined. Therefore, if stress-drop values are to be compared across studies, they should first be converted to the equivalent corner-frequency values, using the physical parameters and constants that apply to each study being referenced. Likewise, if stress-drop values are used to predict ground motions, the prediction model needs to implement internally consistent conventions in linking spectral amplitude to stress drop through the corner frequency. It should be noted that rupture radius is also sensitive to the assigned value for hypocentral velocity. However, this sensitivity is not pronounced, if corner frequency is taken as the reference parameter, because the radius for a given value of f_c scales as the product of hypocentral velocity and the constant k (Equation 3.10).

We identified 19 earthquakes with complex source properties such as double source pulses in the RSTF and deviations from the ideal spectral ratio shape (Equation 3.2). Wang et al. (2018) related the non-double couple (non-DC) components of moment tensors for events in WCSB to fluid-related mechanisms and/or complexity in the fault structure. They suggested that the orientation of the non-DC components could represent either a crack opening during the rupture, or a secondary fault system being triggered. Following this logic, it could be suggested that each DC and non-DC component generates a source pulse visible in the STF, thus explaining why we observe two source pulses for some of our complex targets. Induced earthquakes with multiple subevents have also been observed in other source studies (López-Comino and Cesca, 2018; Moschetti et al., 2019). Interestingly, 15 of our 19 complex events displayed directivity. This could be explained by two subevents that are spatially and temporally separated; if the first subevent triggers

the second subevent after it has travelled some distance along the fault, their waves will reach stations located in the forward rupture direction at the same time and superimpose constructively; by contrast, stations located in the opposite direction will see the two pulses as temporally separated, creating a wider STF and possibly two separate pulses. López-Comino and Cesca (2018) studied the fluid-induced 2016 **M** 5.1 Fairview, Oklahoma, earthquake and found two clear subevents within the rupture. In this case, the subevents ruptured in opposite directions, making rupture directivity difficult to detect.

It is noteworthy that the target earthquake with the largest stress drop (event 51, 390 MPa) was found to have ruptured two subfaults in opposite directions (Eyre et al., 2019), similar to the **M** 5.1 Fairview earthquake. Eyre et al. (2019) used a dense local borehole array and identified a complex north–south fault system for event 51. The earthquake ruptured both a northern north–south-oriented fault strand and a southern north–northeast–south–southwest-fault strand, originating on the southern tip of the north–south fault and rupturing bilaterally. The regional stations that had EGF earthquakes were primarily located to the north and south, which led to mostly forward rupture directivity being observed (see Figure 3.10). The sparse and limited azimuthal distribution of stations may explain the high corner frequency and large stress drop computed for this event. In our study, event 51 was given a directivity index = 2 (no directivity observed) because there was no apparent variation in corner frequency. This is consistent with a bilateral rupture and limited station distribution. Moreover, the subgroup of events with directivity index = 2 had the highest average stress drop; which could be explained by bilateral rupture in opposite directions for some of the earthquakes. This highlights the limitations imposed by large azimuthal gaps in station coverage in crucial directions, especially with complex earthquakes.

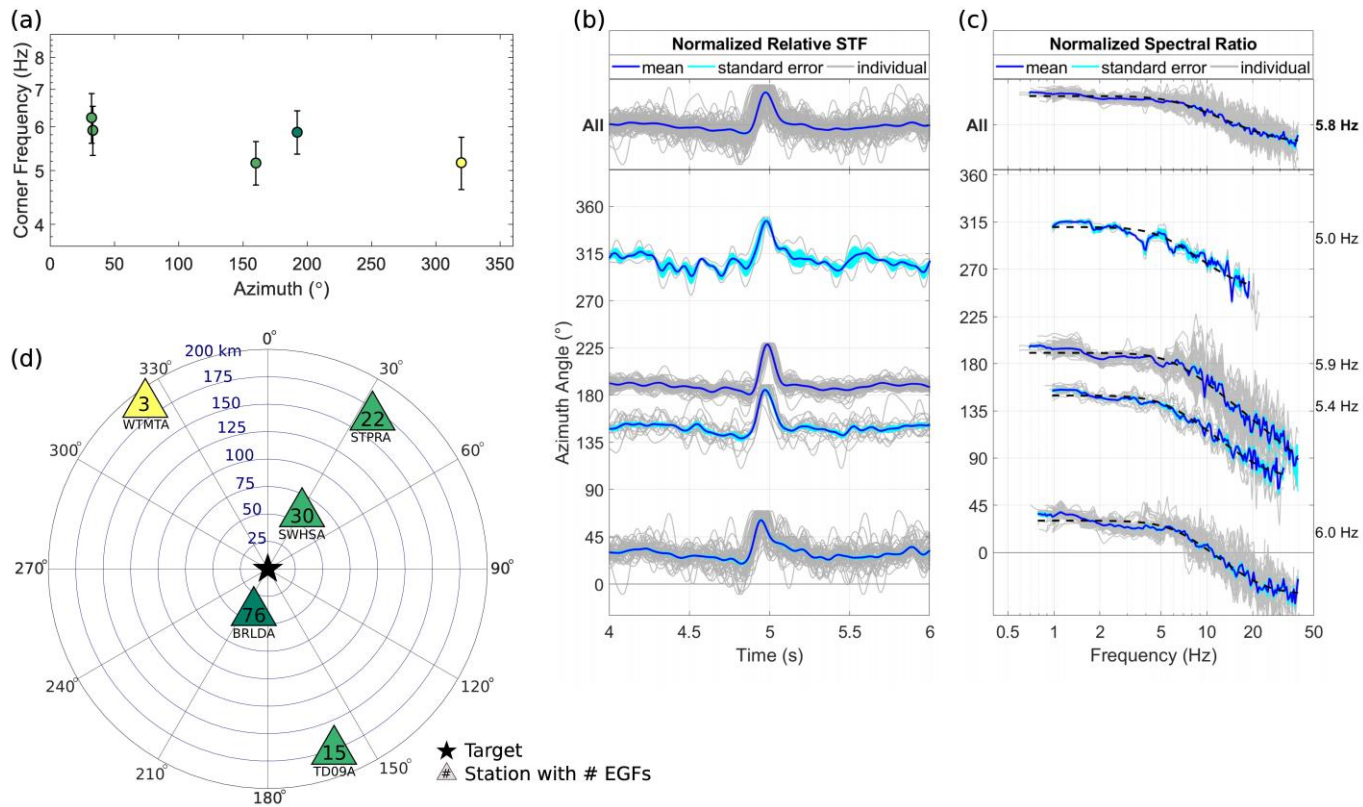


Figure 3.10. Target earthquake (event 51) with large stress drop of 370 MPa. (a) Corner frequency plotted against station azimuth with vertical error bars. Circles are darker if there are more EGF earthquakes for that station. (b) Normalized RSTFs and (c) spectral ratios are shown varying with station azimuth binned by intervals of 20°. Dashed black lines are the fitted spectral ratios, with the resultant corner frequencies displayed on the right. (d) Polar plot of the station coverage with distance, with the target earthquake as a star and the stations as triangles. The colors are the same as in (a), and the number of EGF earthquakes are given in the triangles.

There are other possible explanations of the complex spectral shapes observed for some events. Uchide and Imanishi (2016) examined stacked spectral ratios of earthquakes from Japan and found that a significant fraction of the earthquakes that seemed complex deviated from the typical omega-square model in terms of the high-frequency fall-off rate ($n = 2$). Kaneko and Shearer (2014) found that n varies between 1.5 and 3.3 depending on the takeoff angle of the seismic waves from the fault. Another model that deviates from the omega-square shape is the double-corner-frequency model (Gusev, 1983; Boatwright, 1988; Boore and Atkinson, 1992; Atkinson, 1993; Archuleta et al., 2016). The model arose to explain the sag often seen in source spectra of large earthquakes at intermediate frequencies. The two corner frequencies have been described in different ways; the first corner is usually related to the earthquake rupture time; the second corner has been related to either asperities or barriers within the fault (Gusev, 1983), or to earthquake rise time (Archuleta et al., 2016).

Some studies found that letting the corner frequency of the EGF ($f_{c,EGF}$) be a free parameter can introduce bias in the estimate of the target earthquake's corner ($f_{c,T}$) (Baltay et al., 2010; Shearer et al., 2019), especially if $f_{c,EGF}$ is outside the frequency bandwidth. To test the potential influence of $f_{c,EGF}$ on $f_{c,T}$, we choose several trial events with sufficient bandwidth to cover both $f_{c,T}$ and $f_{c,EGF}$. We then consider the impact of limiting the bandwidth to exclude $f_{c,EGF}$ by just considering the frequencies below the midpoint (in log space) between our initial estimates of $f_{c,T}$ and $f_{c,EGF}$; we call this frequency f_{mid} . We fix $f_{c,EGF}$ at either its lowest or highest reasonable value relative to the initial $f_{c,EGF}$ solution and investigate how the resultant $f_{c,T}$ varies. The lowest reasonable value is taken as being half-way between f_{mid} and the initial $f_{c,EGF}$ (so $\frac{3}{4}$ of the distance in log space from $f_{c,T}$ to $f_{c,EGF}$). The highest reasonable value is taken as two times the initial $f_{c,EGF}$. We found that $f_{c,T}$ does not vary by more than 10% of its value if we fix $f_{c,EGF}$ anywhere within the range from its minimum to maximum reasonable value. Considering that our $f_{c,T}$ uncertainties from the variance check of Equation (3.2) are usually between 10% and 15%, the uncertainties already include the possible variation in $f_{c,T}$ due to the influence of $f_{c,EGF}$. Moreover, in our study, both $f_{c,T}$ and $f_{c,EGF}$ lie within the resolvable bandwidth for 77%

of our events. Therefore, the values of $f_{c,T}$ for the target events are robust with respect to $f_{c,EGF}$ variability, although they may vary from station to station.

One of the largest induced earthquakes to date in the WCSB occurred in November 2018, estimated at **M** 4.6 (Mahani et al., 2019). This event is included in our analysis (event 112). No clear EGFs were found when we searched the closest (public) station over the time window of ± 2 months. However, because of its size and its importance, we lowered the initial CC limit from 0.8 to 0.65 for this event, which resulted in 10 detected EGFs, which were then used to compute spectral ratios. The event shows some azimuthal variation in corner frequency, as shown in Figure 3.11. Using a Haskell model, we obtained a corner frequency of 2.3 ± 0.1 Hz. If no azimuthal variation is assumed and equal stacking is performed over all azimuths, our corner frequency increases to 3.0 ± 0.3 Hz. Our computed moment magnitude for the event based on the displacement spectra is **M** 4.3, giving a stress drop between 54 and 120 MPa for the observed range of corner-frequency estimates – if we assume crustal constants corresponding to a depth of 4 km. If we instead assume the event is **M** 4.6 at a depth of 2 km, as reported by Mahani et al. (2019), the associated stress-drop values are very high, from 528 to 1170 MPa. Again, this points to the high sensitivity of stress-drop values to underlying physical constants, and the reason why corner frequency should be considered as the more fundamental source parameter. Rupture radius has similar issues as a source parameter, though not to the same degree (e.g., see Equation 3.10). Finally, we note that the spectral ratios for this target earthquake are of lower quality than those for all other targets studied here, because we relaxed the correlation criteria. This is apparent in the large standard error of the spectral ratios and the lack of a clear pulse shape in the RSTF (Figure 3.11). Therefore, the corner-frequency and stress-drop estimates for this event are considered less reliable.

Earthquake directivity effects, observed in more than one-third of the study events, have implications for the strength and frequency content of ground motions, and thus impact the associated hazard. In general, ground motions will have shorter duration, higher

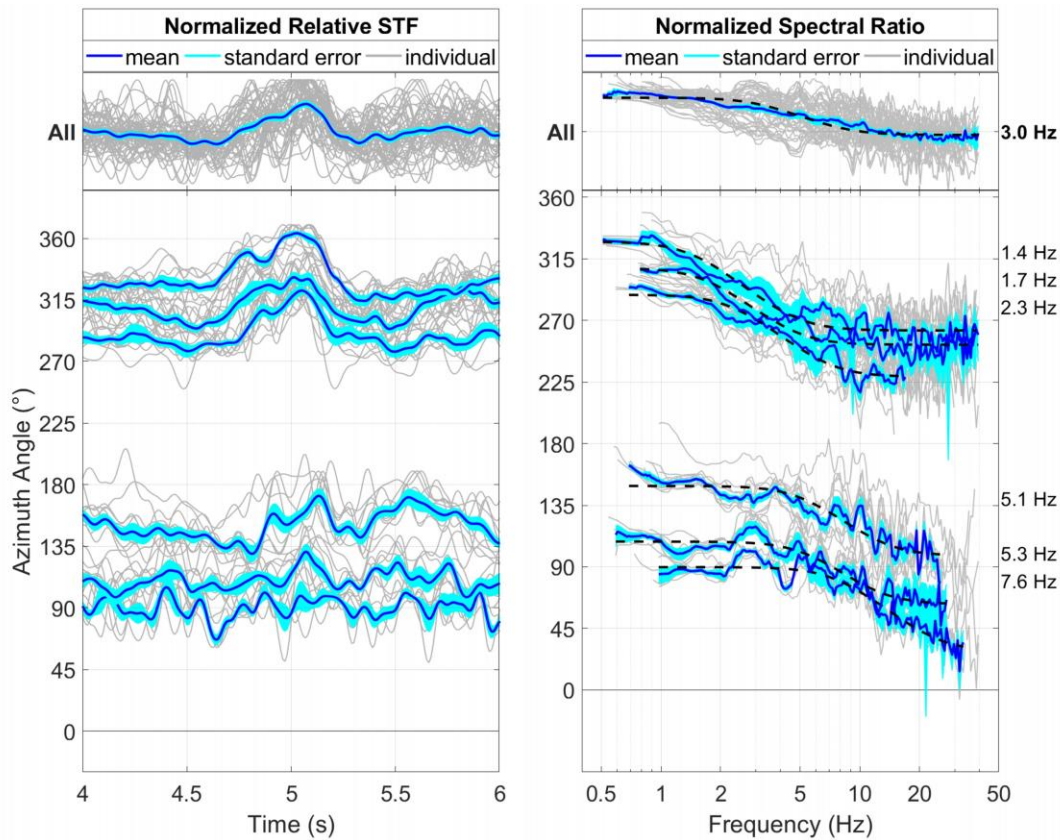


Figure 3.11. The November 2018 Fort St. John earthquake (event 112). (a) Normalized RSTFs and (b) spectral ratios are shown varying with station azimuth. The azimuths are binned by intervals of 20° . The top stack shows all the individual records stacked. The average over each azimuthal interval is shown as a dark line with its standard error width indicated by a lighter shaded line behind. Dashed black lines are the fitted spectral ratios, with the resultant corner frequencies displayed on the right.

corner frequency, and stronger high-frequency content in the forward propagation direction (e.g., Spudich et al., 2008, 2014; Wang et al., 2017). This means that ground motions could be significantly higher than the median at some azimuths, especially at high frequencies. Because such effects are difficult to predict deterministically in advance of events, they are accommodated in ground-motion prediction equations (GMPEs) through their impact on both the median amplitudes and their aleatory variability (e.g., Spudich et al., 2014). Future study of GMPEs for induced events can examine whether the expected effects of directivity

can be observed in ground-motion amplitudes; these effects would be manifested as an azimuthal variability in within-event residuals and/or their variability.

3.6 Conclusion

We use the EGF method to compute corner frequencies and stress drops of 87 induced earthquakes in the WCSB. We find that the corner frequencies are similar to those of induced events in Oklahoma, calculated using comparable techniques, for the magnitude range M 2.3-4.4. More than one-third of the earthquakes show evidence of rupture directivity; fitting them to a unilateral Haskell source yields rupture azimuths primarily oriented approximately north-south. These fault orientations can be linked to either the region's current north-east-southwest S_{Hmax} , or for cases where there are local stress field variations, subsurface pore pressure increase from fluid injections (Zhang et al., 2019). Corner frequency for a single event may vary with station azimuth by more than a factor of 4, emphasizing the importance of having good azimuthal coverage for the determination of source properties. Moreover, the relationship between corner frequency and stress drop is highly dependent on the assumed physical constants and equation conventions, and thus absolute values of stress drop are less significant than relative values within a single study. We therefore consider the corner frequency to be a more fundamental and useful source parameter.

Chapter 4

4 Reconciling Ground Motions and Stress Drops for Induced Earthquakes in the Western Canada Sedimentary Basin³

Chapter 4 examines the usage of Brune stress drop as the input stress parameter model in a ground-motion prediction equation, and later checks the equivalency stress drop and stress parameter as measures of the high-frequency content of ground motion.

4.1 Introduction

The earthquake source parameter widely referenced as the stress drop ($\Delta\sigma$) is plagued by many definitions and many conventions for its determination, see Section 1.2.2. It became a parameter of interest in the development of ground-motion prediction equations (GMPEs, also called ground-motion models) from the 1980s (Hanks, 1979; Hanks et al., 1981; Boore, 1983; Toro et al., 1987; Atkinson and Boore, 1997; Campbell, 2003; Atkinson et al., 2006). Many approaches to the development of GMPEs, including the stochastic approach (e.g., Boore, 2003) and the hybrid empirical approach (e.g., Campbell, 2003; Pezeshk et al., 2018), tie the amplitude of the high-frequency ground motions to the Brune (1970) source model (see Section 1.3.2).

There are several definitions and conventions for determining stress drop. Issues arise when differing definitions of stress drop are used interchangeably because they are not equivalent (Atkinson and Beresnev, 1997). As discussed in Chapter 3, one common approach to determine the stress drop relates the far-field value of f_c to the fault dimensions (e.g. Allmann and Shearer, 2009; Huang et al., 2016; Abercrombie et al., 2017; Sumy et

³ A version of this has been accepted for publication. Holmgren, J. M., G. M. Atkinson, and H. Ghofrani (2020). "Reconciling Ground Motions and Stress Drops for Induced Earthquakes in the Western Canada Sedimentary Basin," *Bulletin of the Seismological Society of America*

al., 2017), where f_c is most often determined from an Empirical Green's Function (EGF) approach. We denote this definition of the stress drop as $\Delta\sigma_{drop}$. Another well-known definition comes from the engineering seismology perspective (Hanks, 1979; Hanks et al., 1981), wherein it stress drop is determined from the high-frequency spectral amplitudes of observed ground motions ($f \gg f_c$). To distinguish it from the definition based on dimensional source attributes inferred from an EGF analysis, the stress defined in this way is often referred to as the stress parameter (e.g., Boore, 2003; Atkinson et al., 2006), which we denote $\Delta\sigma_{par}$ herein.

There are a few reasons why $\Delta\sigma_{drop}$ and $\Delta\sigma_{par}$ may differ from each other even if their definitions are entirely consistent. Specifically, $\Delta\sigma_{drop}$ is typically inferred from an EGF analysis conducted in the Fourier domain, whereas $\Delta\sigma_{par}$ describes the ground-motion amplitudes in the response spectral domain. As described in Section 1.3.1, Fourier and response spectra are not linearly related (Bora et al., 2016); they scale similarly at low frequencies but at high frequencies the response spectrum is dependent on both the high- and low-frequency sections of the corresponding Fourier spectrum. Moreover, there are a number of methods and conventions for determining both parameters, which further complicate comparisons.

Holmgren et al. (2019) determined corner frequencies and stress drops of 116 earthquakes in the Western Canada Sedimentary Basin (WCSB) using the EGF approach, largely following the methods of Abercrombie et al. (2017). The EGF method is seen by many researchers as an advantageous way to retrieve the source spectrum (e.g. Baltay et al., 2010; Onwuemeka et al., 2018; Yoshimitsu et al., 2019). The advantage of the EGF approach is that it avoids the trade-offs involved in simultaneously determining source, path, and site effects by using spectral division of the target earthquake by a smaller, collocated earthquake (an EGF earthquake). The spectral division effectively removes the path and site components from the recorded spectrum of the target earthquake, provided that the EGF earthquake shares the same focal mechanism, propagation path, and site effect as the target record. These conditions are commonly satisfied by requiring a high cross-correlation coefficient between the target and EGF earthquakes (e.g. Abercrombie, 2015).

Holmgren et al. (2019) observed large station-to-station variability in $\Delta\sigma_{drop}$ estimates for many of the studied earthquakes in the WCSB, which they attributed to the sparse station coverage coupled with significant rupture directivity effects. Directivity results in larger apparent values of f_c and $\Delta\sigma$ in the forward rupture direction, and lower values in the backward direction, see Section 1.2.3. The directivity effects may average out if the earthquake is recorded over many azimuths, but directivity will increase the variability and can lead to bias of $\Delta\sigma_{drop}$ if the station distribution is sparse.

Hanks (1979) and Hanks and McGuire (1981) advanced a method to determine $\Delta\sigma_{par}$ from ground motions using random vibration theory to relate the root-mean-square acceleration (a_{rms}) of the acceleration spectrum to peak ground acceleration (PGA). This approach was extended to interpret both peak ground motions and response spectra in the context of the stochastic ground motion model (Boore, 1983, 2003; Boore et al., 2010), and has been widely applied in the development of stochastic GMPEs (e.g., Toro et al., 1987; Atkinson et al., 2006). Boore et al. (2010) showed that the value of $\Delta\sigma_{par}$ is very sensitive to the geometric spreading model assumed. Yenier and Atkinson (2015a) attempted to avoid the trade-off between the source and path parameters in their generic GMPE approach by using the shape of the observed spectrum to determine $\Delta\sigma_{par}$, instead of its absolute amplitude. Atkinson et al. (2015) followed a similar approach, but also removed site effects using simultaneous regression to the generic GMPE form.

From a methodological perspective, the EGF approach is the preferred way to obtain information on the source spectrum, because it clearly separates the source effect from those of path and site. However, EGF studies are subject to restrictive data requirements due to their reliance on small collocated earthquakes to use as EGFs. Moreover, if the intended use of the source information is for the prediction of engineering measures of ground motion (i.e. peak amplitudes and response spectra), then it is not clear whether the results of EGF studies are directly applicable. The GMPE approach, by contrast, is versatile and practical, linking its measure of stress directly to ground motion amplitudes.

In this study, we investigate the use of $\Delta\sigma_{drop}$ as a proxy for $\Delta\sigma_{par}$. The study serves several useful purposes: (i) it defines a region-specific GMPE for the WCSB; (ii) it reconciles models of $\Delta\sigma_{drop}$ with observed ground motion amplitudes at high frequency; (iii) it illustrates how published $\Delta\sigma_{drop}$ estimates from the literature can be used to aid in the development of GMPEs; and (iv) by comparing the estimates of $\Delta\sigma_{par}$ to the corresponding estimates of $\Delta\sigma_{drop}$ for individual earthquakes, we gain insight into the strengths and weaknesses of these alternative windows into high frequency ground motion processes.

4.2 Database

The study database is that of Holmgren et al. (2019), who used the EGF approach to obtain source parameters for induced earthquakes in the WCSB; we update it to include two recent events. We use only those earthquakes for which we were able to determine moment magnitude (\mathbf{M}). The database consists of earthquakes from April 2013 to June 2019, including 92 earthquakes with \mathbf{M} from 2.3 to 4.4, recorded on stations within 200 km epicentral distance. Most of the events occurred at very shallow depth (<5 km). On the basis of spatiotemporal correlations with proximate oil and gas operations, it is believed that most (~60%) of the events were triggered by hydraulic fracturing (Atkinson et al., 2016). Figure 4.1 shows an overview map of the region, along with the record distribution in magnitude and distance. The records are three-component broadband seismograms, recording velocity at 100 samples \cdot s⁻¹. The \mathbf{M} for each event was determined by fitting the low-frequency level of the displacement spectrum to a Brune (1970) source model, assuming bilinear geometrical spreading with a slope of -1.3 to 50 km, and -0.5 thereafter (Yenier et al., 2015b) and a frequency independent quality factor $Q = 1000$; we confirmed by analysis of residuals versus distance that this model fits the observed low-frequency attenuation trends.

We bandpass filter all records between 0.1 and 50 Hz using a two-pole, two-pass, Butterworth filter. Next, the signal-to-noise ratio (SNR) is checked by comparing five seconds of S-wave recording to pre-P noise. Records with $SNR \geq 3$ are retained for analysis. Each retained record is corrected to remove instrument response, converted to

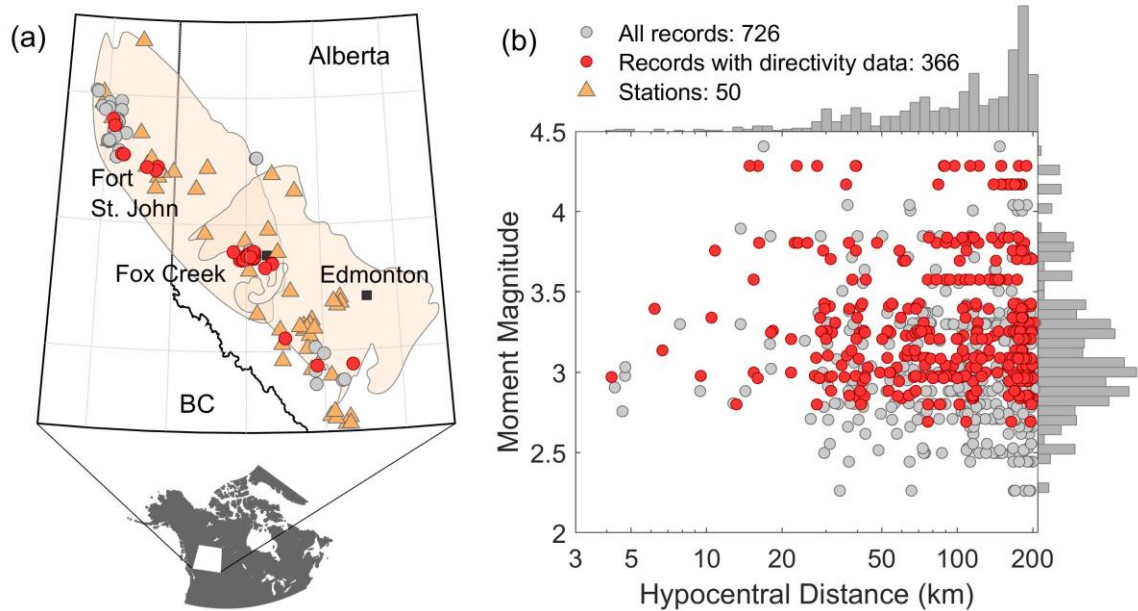


Figure 4.1. Database of study earthquakes and records. (a) Map of stations (triangles) and study earthquakes (light circles); those with resolvable directivity are shown as dark circles. Shaded region is the Western Canada Sedimentary Basin. (b) Record distribution by moment magnitude and distance.

acceleration, and windowed to start five seconds before the P-wave arrival and last for 85 seconds in total. We compute the 5% damped pseudo-spectral acceleration (PSA) from the accelerograms using the Nigam and Jennings (1969) algorithm. For records where both horizontal components passed the SNR check (almost all of the retained records), we compute the horizontal geometric mean response spectrum (geomean PSA). The retained database comprises 726 geomean PSA from 92 earthquakes, recorded on 50 stations. About half of the records come from earthquakes that Holmgren et al. (2019) determined to have resolvable directivity effects. Tables S4.1 and S4.2, available in the electronic supplement, contain the earthquake parameters and individual PSA records, respectively.

4.3 Generic GMPE

We use the generic GMPE method (Yenier et al., 2015a, 2015b) to develop a regionally-calibrated stochastic equivalent point source model for response spectral amplitudes. Our approach follows that of Novakovic et al. (2019), in using regression to determine source, path and site effects within the generic GMPE framework, wherein for each record:

$$\ln Y = F_E + F_Z + F_\gamma + F_S + C , \quad (4.1)$$

where Y is the recorded ground motion (in this case PSA at a specific frequency), F_E is the event term (a frequency-dependent source effect), F_Z is the geometrical spreading term (a frequency-independent path effect), F_γ is the anelastic attenuation (a frequency-dependent path effect), F_S is the site term (a frequency-dependent site effect), and C is a frequency-dependent regional calibration factor that encompasses any residual regional effects. F_E consists of two components, which model the source effects of magnitude and stress parameter on ground motions in the response domain:

$$F_E = F_M + F_{\Delta\sigma} . \quad (4.2)$$

F_M describes the magnitude-scaling effect for a Brune (1970) point-source model with constant stress drop of 100 bars, assuming high-frequency attenuation given by kappa (Anderson and Hough, 1984) of $\kappa_0 = 0.025$ s (see Yenier and Atkinson, 2015a, 2015b). $F_{\Delta\sigma}$ describes the stress parameter scaling effect for events with stress values higher or lower than the reference value of 100 bars. The idea behind Equation (4.2) is to separate the effects of magnitude and stress parameter on the scaling of response spectral amplitudes.

For simplicity, several of the GMPE components are adopted from previous studies. F_M does not depend on region, and is taken directly from Yenier and Atkinson (2015b). We assumed an initial model for $F_{\Delta\sigma}$ that was developed by fitting the Holmgren et al. (2019) WCSB $\Delta\sigma_{drop}$ versus magnitude to a simple two-segment line. Since the generic GMPE's $\Delta\sigma_{par}$ is in terms of bars and based on the Brune k -model (Yenier and Atkinson, 2015a), the $\Delta\sigma_{drop}$ were first converted accordingly. We scaled the initial best

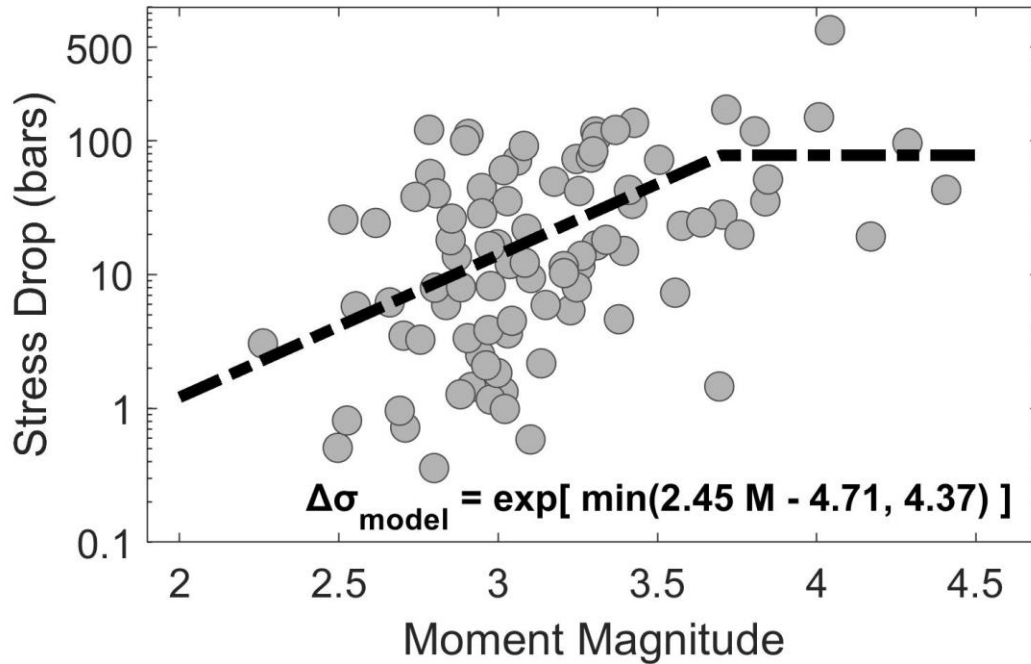


Figure 4.2. Input stress parameter model $\Delta\sigma_{model}$ (dashed line) compared to the WCSB stress drop values from the EGF study of Holmgren et al. (2019) (circles).

fit model for the $\Delta\sigma_{drop}$ values up slightly (by a factor of 1.3) because we found this was needed to ensure consistency on average between $\Delta\sigma_{drop}$ and the output $\Delta\sigma_{par}$; we return to this point later. Figure 4.2 shows the adopted $F_{\Delta\sigma}$ function. F_Z and F_γ were determined empirically for the WCSB by Novakovic et al. (2019). Table A4.1 contains the functional forms of these components, and Table S4.3, available in the electronic supplement, contains the coefficient values. For a detailed description of the methodology and its parameters, see Yenier and Atkinson (2015b) or Novakovic et al. (2018).

In order to fine-tune the generic GMPE to describe our WCSB database, we first convert the Novakovic (2018) anelastic attenuation parameter (γ) to the equivalent Q :

$$Q(f) = -\frac{\pi f}{\gamma\beta}, \quad (4.3)$$

where f is frequency in Hz and β is the shear-wave velocity in $\text{km} \cdot \text{s}^{-1}$. Multiple studies have reported source depths between 3-4 km for induced events in the WCSB (e.g. Schultz et al., 2017; Eaton et al., 2018; Wang et al., 2018). Therefore, following Holmgren et al. (2019), we assume a constant depth of 4 km and $\beta = 3.2 \text{ km} \cdot \text{s}^{-1}$ for all earthquakes (Chen et al., 2015; Wang et al., 2018). The regional seismic Q model can be expressed as:

$$Q(f) = \max(120, 271 f^{0.96}), \quad (4.4)$$

which is then converted back (i.e. through Equation 4.3) to provide a smoothed function for the γ factor. Figure 4.3 shows $\gamma(f)$ and $Q(f)$ for the WCSB in comparison to values for three other regions in North America as determined using the same methodology. Figure 4.4 displays Q values reported in other studies in the literature. The WCSB Q has the steepest slope out of the models compared, which could reflect large amounts of high-frequency attenuation in the area. However, while the reported Q -values are all based on similar geometrical spreading functions, their underlying methods are different. Only the YA15b and this Q model are developed using response spectra, which could explain why those slopes differ from the rest.

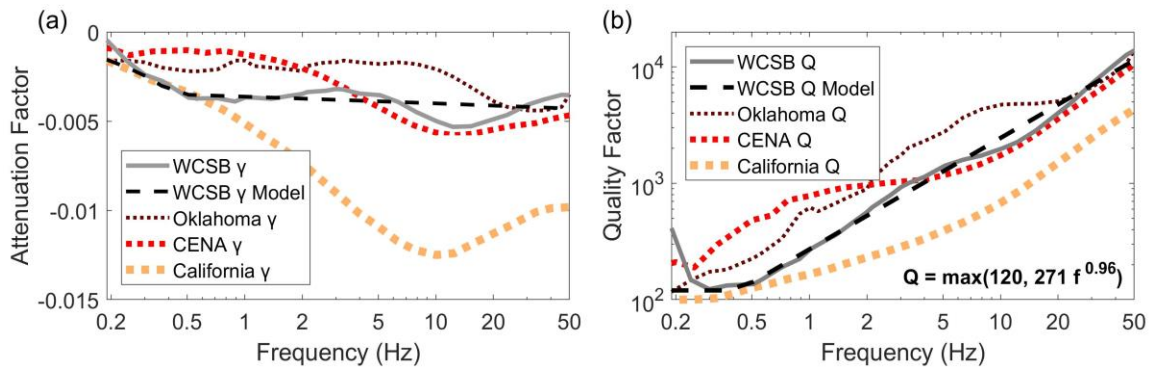


Figure 4.3. (a) Anelastic attenuation coefficient values γ (solid grey line) and the proposed smoothed model (dashed black line) for the Western Canada Sedimentary Basin (WCSB), in comparison to γ values from Oklahoma (dark dotted) (Novakovic et al., 2018), Central Eastern North America (CENA, medium dotted) (Yenier et al., 2015b), and California (light dotted) (Yenier et al., 2015b). (b) Quality factor as determined from γ using Equation (4.3) (same models); equation for the WCSB Q model is given.

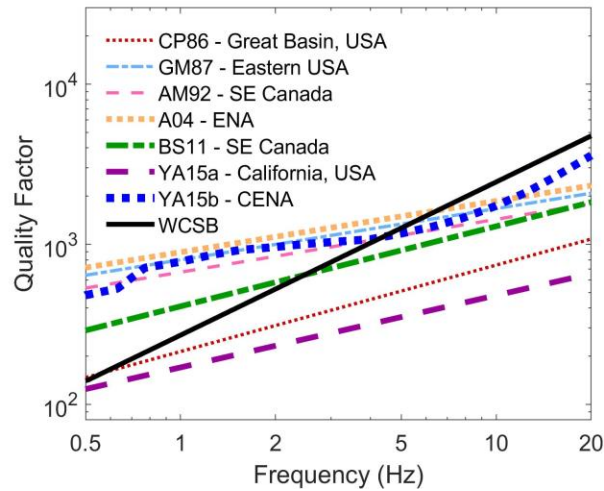


Figure 4.4. Western Canada Sedimentary Basin (WCSB) quality factor (black solid line) compared to Q -values in literature for different regions: CP86 – Chávez and Priestley (1986), Great Basin USA; GM87 – Gupta and McLaughlin (1987), eastern US; AM92 – Atkinson and Mereu (1992), southeastern Canada; A04 – Atkinson (2004), eastern North America; BS11 – Boatwright and Seekins (2011), southeastern Canada; YA15a – Yenier and Atkinson (2015a), California; YA15b – Yenier and Atkinson (2015b), central-eastern North America.

In order to obtain F_S and C , we compute the residuals of the horizontal geomean PSA (i.e. the difference between the observed and model PSA in natural logarithm units) after removing all other effects. The residual can be expressed as $F_S + C$:

$$F_S + C = \ln Y - (F_E + F_Z + F_Y). \quad (4.5)$$

For each station with ≥ 3 records, the average station residual is computed over all events. C is taken as the mean value of the average station residuals, to provide equal weighting to each station. When defined in this way, the factor C can be interpreted as the average regional difference between the site conditions at the stations and those embedded in the generic GMPE of Yenier and Atkinson (2015a, 2015b) and Novakovic et al. (2018). These differences are substantial, because most sites in the WCSB are on soil (Farrugia et al.,

2017), whereas the reference condition for the generic GMPE is B/C boundary site condition ($V_{S30} = 760$ m/s) with site high-frequency attenuation term $\kappa_0 = 0.025$ s. The station terms F_S provide the difference between the average station residual and C for each station. Figure 4.5 displays C and F_S for the 50 stations that passed the ≥ 3 record criterion. Table S4.4 (available in the electronic supplement) contains the individual station terms.

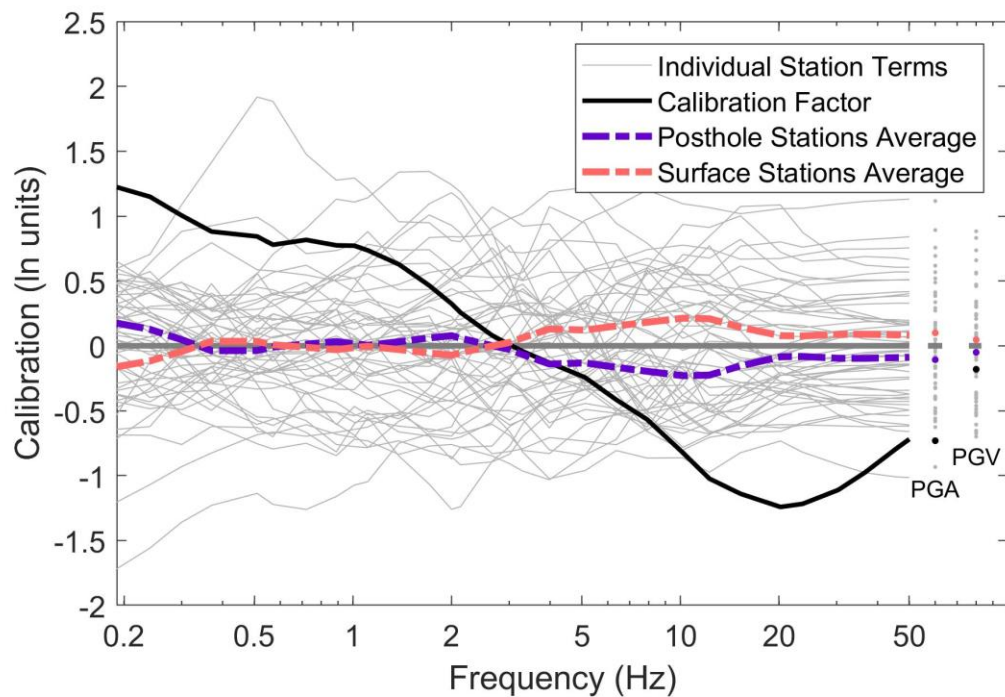


Figure 4.5. Calibration factor (C , heavy black line) and individual station terms (F_S , light lines) for the 50 stations in this study. The average all of the individual station terms (heavy grey line) is constrained to zero by definition and thus the calibration factor contains any average regional site response. The average posthole and station terms are shown in dark and light dashed lines, respectively.

4.4 Stress Parameter, $\Delta\sigma_{par}$

The stress parameter is contained in F_E , through its $F_{\Delta\sigma}$ component (Equation 3.2 and Table A4.1). Using the developed regional GMPE, we invert for the best-fitting value of $\Delta\sigma_{par}$ for each record using non-linear least squares, considering the known values of \mathbf{M} and distance, with the aim to compare them to the initial $\Delta\sigma_{drop}$ estimates. We compute the uncertainty in $\Delta\sigma_{par}$ by using a grid search technique to find the perturbation of the best-fit value that results in an increase of variance by 5%.

The stress parameter value can also be expressed in terms of the corresponding corner frequency. The underlying earthquake source model of the generic GMPE assumes a Brune (1970) source model in which $\Delta\sigma_{par}$ is related to the Brune corner frequency, f_c , through (Eshelby, 1957; Boore, 2003):

$$\Delta\sigma_{par} = \frac{7}{16} M_0 \left(\frac{f_c}{k_{Brune} \times 10^7 \beta} \right)^3 = M_0 \left(\frac{f_c}{4.9 \times 10^6 \beta} \right)^3 \quad (4.6)$$

where $\Delta\sigma_{par}$ is in bars, M_0 is the seismic moment in dyne·cm, f_c is in Hz, and k_{Brune} is a constant relating the rupture radius to f_c (where $k_{Brune} = 0.372$). As for Equation (4.3), we assume a constant focal depth of 4 km and $\beta = 3.2 \text{ km} \cdot \text{s}^{-1}$ for all earthquakes. Equation (4.6) can be used to convert the $\Delta\sigma_{par}$ values obtained by PSA inversion to f_c values for each record. In contrast to Chapter 3, where we followed the typical earthquake seismology approach and defined $\Delta\sigma$ in terms of MPa (1 MPa = 10 bars) and used the Madariaga k -model ($k = 0.21$), this chapter's $\Delta\sigma$ is defined following the engineering seismology approach using bars and the Brune k -model. Hence, before comparison, the $\Delta\sigma_{drop}$ and $\Delta\sigma_{par}$ need to be converted into equivalent measures.

Figure 4.6 shows two examples of the GMPE fitting process, in which we compare the GMPE for the best-fit stress parameter for a specific record to the observed ground-motion. The equivalent corner frequency for the specific record is also indicated. An interesting feature to note on Figure 4.6 is the relatively low high-frequency spectral amplitudes for typical records in the WCSB. This is reflected in the overall calibration

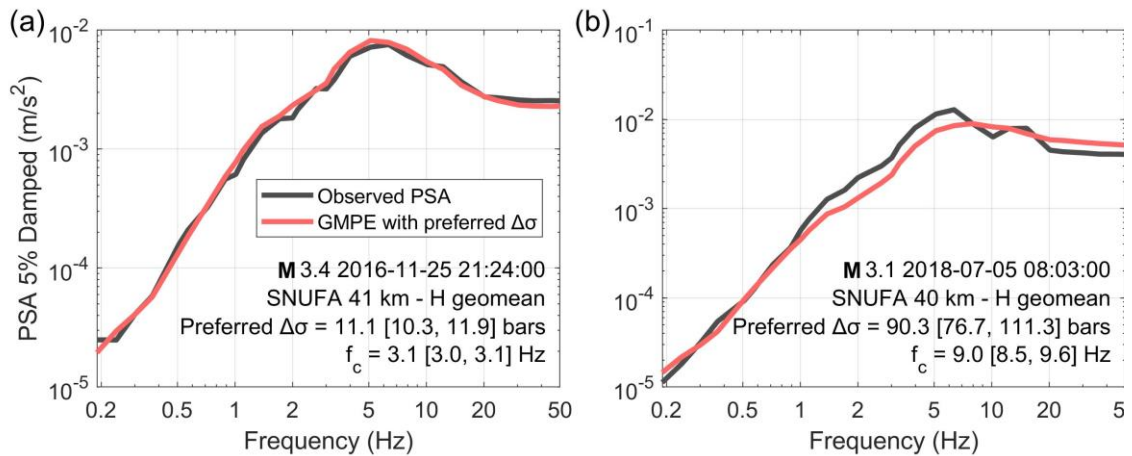


Figure 4.6. Examples of fitting the GMPE (light solid line) to observed data (dark solid line) at Station SNUFA for two specific events (details shown in figure panels). The numbers in brackets show error range on parameters.

constant C (Figure 4.5), which diminishes high-frequency amplitudes relative to those expected for the gradational B/C profile with $\kappa_0 = 0.025$ s that was the basis for the original generic GMPE formulation of Yenier and Atkinson (2015a). We infer a strong influence of high-frequency site attenuation for most sites in the region. Some of this may be due to the relatively soft soils on which many instruments are located. Moreover, many of the WCSB seismometers were installed in postholes at several meters depth, which may significantly dampen high-frequency amplitudes relative to surface installations (H elo ise et al., 2012; Hollender, 2019). This can occur due to destructive interference of the down-going wave (that has been reflected at the surface) with upcoming waves. Hollender (2019) compared the high-frequency amplitudes at a surface station to one buried at 3 m and found a de-amplification (factor of 0.7) at 15 Hz. This effect appears in the station terms F_S in Figure 4.5. When comparing the average F_S of all posthole stations to the average surface station F_S (darker and lighter dashed lines, respectively), it is seen that the postholes tend to have lower values at higher frequencies, indicating less high-frequency content. This will be discussed later.

Finally, we compute the stress parameter for each earthquake. To ensure equivalent comparisons between methods, corner frequency was treated as the basic source parameter. We take the geometric mean of the f_c values at all stations recording an event, then convert it back to $\Delta\sigma_{par}$ through Equation (4.6), to obtain the event-specific values of $\Delta\sigma_{par}$. Using the initial input stress model (solely based on the EGF $\Delta\sigma_{drop}$ values), the individual $\Delta\sigma_{drop}$ and $\Delta\sigma_{par}$ estimates differed on average by a factor of 1.3. Since we wanted a GMPE which produced, on average, $\Delta\sigma_{par}$ similar to $\Delta\sigma_{drop}$ in order to study their discrepancies, we ensured a 1:1 relationship by adjusting the input model by a factor of 1.3 (Figure 4.2). However, both these input stress models resulted in similar residuals. Thus, unless individual $\Delta\sigma_{par}$ estimates are of interest, there is no need to adjust the initial input stress model.

4.5 Results

4.5.1 GMPE Residuals and Directivity Effects

The final residuals for the modified WCSB GMPE are shown in Figure 4.7. No dependence on magnitude or distance is observed, with the possible exception of a sparsely-defined positive trend at high frequencies at very close distances. Holmgren et al. (2019) found that f_c varied significantly with station azimuth for about half of the earthquakes in the WCSB, despite their relatively small magnitude. In order to investigate the effect of directivity on response spectral amplitudes, we partition the residuals from Figure 4.7 into their corresponding between- and within-event terms. The between-event term represents the average difference between an event's source term and the median prediction of the GMPE, whereas the within-event term is each record's offset relative to the GMPE, after correcting for the between-event term (Al Atik et al., 2010), see Section 1.3.3. To study azimuthal effects, we are interested in the within-event component. As shown on Figure 4.8, we find that directivity effects are observable in response spectra residuals for these events for the higher oscillator frequencies. We note that no residual trends in azimuth were observed for frequencies <1.0 Hz (Figure 4.8 shows an example for 1.0 Hz; plots for lower frequencies look similar). For frequencies >5 Hz, stations located in the forward rupture direction (azimuth relative to rupture direction of $<90^\circ$) tend to have larger PSA values than

predicted by the GMPE, whilst the opposite is true for stations in the backward rupture direction ($\text{azimuth} > 90^\circ$). This effect is on average 0.38 ln units (i.e. a factor of 1.5) in the forward direction and -0.34 ln units in the backward direction. There is also a slight dependence on distance; for example records at ≤ 50 km had a larger forward directivity effect (factor of 1.8), in comparison to records at > 150 km (factor of 1.2). This may partially explain the slight positive trend in high-frequency residuals at close distances – they may be more influenced by directivity effects. Overall, we conclude that the residuals are higher in the forward rupture direction and lower in the opposite direction.

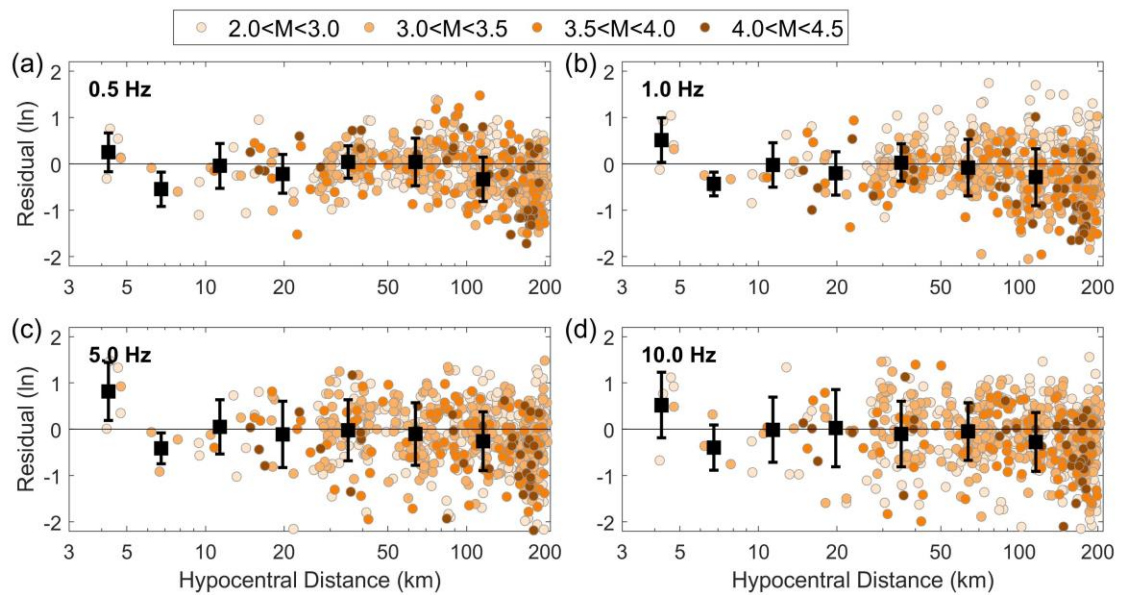


Figure 4.7. Final residuals for the WCSB GMPE for four oscillator frequencies: (a) 0.5 Hz; (b) 1.0 Hz; (c) 5.0 Hz; and (d) 10.0 Hz. The residuals are shaded based on magnitude, where darker circles are higher magnitude events. Squares show mean residuals and their standard deviation in log-spaced distance bins.

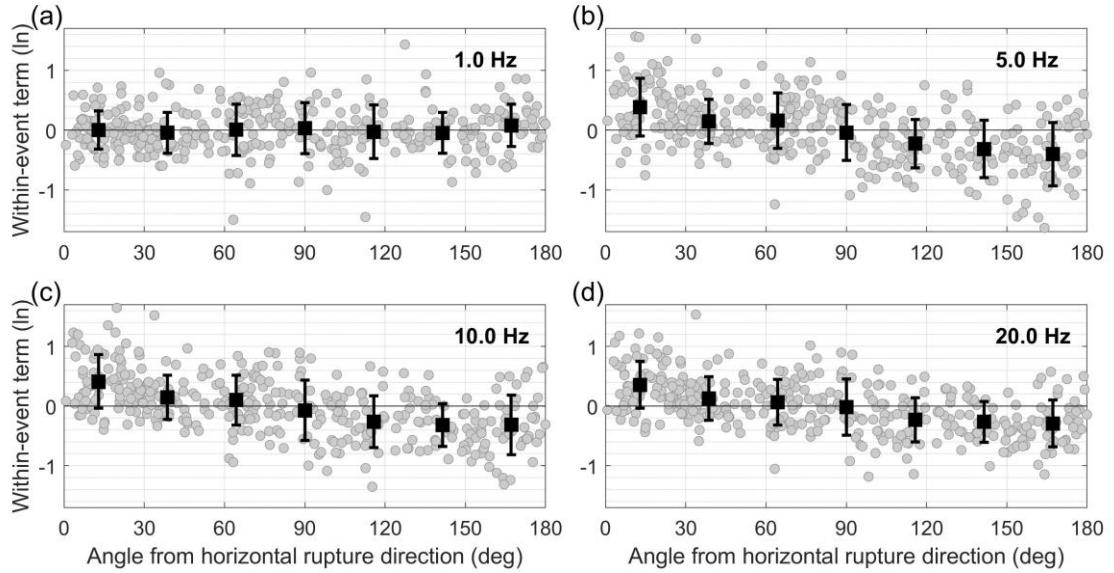


Figure 4.8. Within-event residuals (circles) for the 39 earthquakes with resolvable directivity effects. The residuals are sorted and plotted versus the relative angle with respect to the rupture direction, where 0° records are from stations in the forward rupture direction and 180° records are from stations in the backwards direction. Four oscillator frequencies are plotted: (a) 1.0 Hz, (b) 5.0 Hz, (c) 10.0 Hz, and (d) 20.0 Hz. The mean and standard deviations in azimuth bins are plotted as black squares and vertical horizontal bars.

4.5.2 Stress Parameter vs Stress Drop Values

Figure 4.9 displays the stress parameters for all events as obtained from the region-specific GMPE. In order to compare them directly, the $\Delta\sigma_{drop}$ estimates were converted into bars and defined using the Brune k -model instead of Madariaga k -model. On average, the stress parameters and corresponding stress drop values from the Holmgren et al. (2019) spectral ratio study follow a 1:1 trend (Figure 4.9b), albeit with significant event-to-event scatter. This correspondence is consistent with our defined input stress model to the GMPE development; recall that we defined the input stress model from the EGF stress drop values, scaled slightly so as to obtain a 1:1 trend on average (input model of Figure 4.2). Figure 4.9 also shows the recovered values of $\Delta\sigma_{par}$ in comparison with those of our input model ($\Delta\sigma_{model}$).

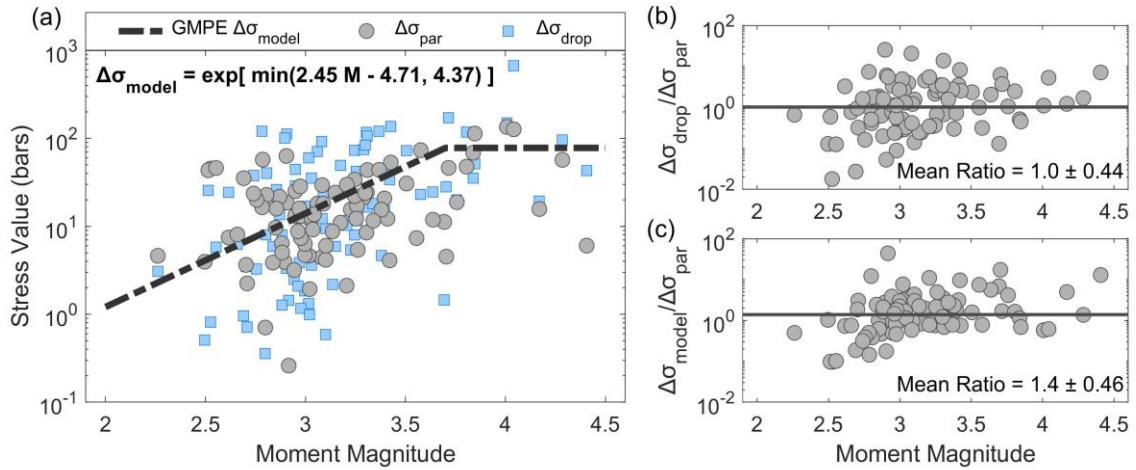


Figure 4.9. (a) Earthquake stress parameters plotted against moment magnitude (circles). The EGF stress drops from Holmgren et al. (2019) are also shown (squares), along with the stress model for WCSB GMPE ($\Delta\sigma_{model}$). (b) Ratios between EGF stress drops and GMPE stress parameters plotted against moment magnitude. (c) Ratios between $\Delta\sigma_{model}$ and the event-specific GMPE stress parameters plotted against moment magnitude. All stress measures have been converted into bars and are defined using the Brune k -model.

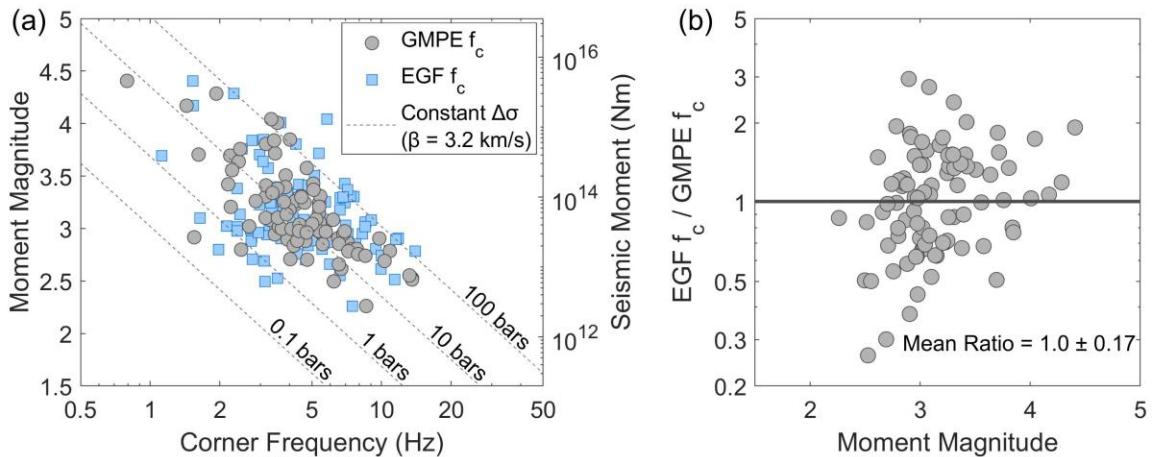


Figure 4.10. (a) Corner frequencies obtained through GMPE inversion (circles) and through the EGF method (squares), plotted against magnitude. Constant stress drop/parameter lines using Equation (4.6) are shown. Note that the values of the stress drop lines depend heavily on the convention used to link corner frequency to stress drop, as described in the text. (b) Ratios between the EGF and GMPE corner frequencies.

Figure 4.10 shows the Brune f_c values from the GMPE inversion compared to the EGF f_c results, plotted against magnitude. It can be seen that the EGF f_c values from Holmgren et al. (2019) tend to be broadly scattered over all corner frequencies, resulting in stress values between 0.1-200 bars. The GMPE f_c values are broadly scattered below 3.0 Hz, but appear to fall between a narrower band at higher frequencies (1-50 bars). We believe that this reflects the lack of ability of the GMPE approach to adequately recover high-frequency source attribute; the strong site effect issues noted at higher frequencies often obscure the corner frequency. Table S4.1 (available in the electronic supplement) contains the final earthquakes' EGF and GMPE f_c values.

4.6 Discussion

We developed a region-specific GMPE for the WCSB calibrated to response spectra data, assuming a Brune source model with attributes taken from an EGF study for the same region. Event-specific estimates of $\Delta\sigma_{par}$ obtained by fitting amplitudes to the GMPE are consistent with the corresponding values of $\Delta\sigma_{drop}$ from the EGF study, but there is significant scatter between estimates. This may partly reflect that $\Delta\sigma_{par}$ is dependent to some extent on both the low- and high-frequency portions of the Fourier spectra (Bora et al., 2016; Bindi et al., 2017), and thus the stress parameter does not have the same physical meaning as the stress drop. Another major difference between the two methods is that the EGF method accounts for the path and site effects through spectral division, whereas the GMPE method is based on empirically-determined average path and site effects in the region. Ide et al. (2003) compared stress drop estimates obtained from the EGF method to those obtained from single-event Fourier spectral fitting and found that the EGF tends to produce higher values of stress drop. They linked the mismatch between the two methods to the trade-off between source and attenuation models when fitting the Fourier spectra of individual events. Boore et al. (2010) also noted the dependence of the stress parameter values on attenuation models in their stochastic-modelling study. In the development of the WCSB GMPE in this study, we used the regional geometric spreading F_z and anelastic attenuation F_γ models from Novakovic et al. (2019). These were derived through empirical

analysis of WCSB earthquakes. Likewise, the final calibration factor C and station terms F_S were also derived empirically based on the residuals (Equation 4.5). The simultaneous solution for parameter coefficients is non-unique and represents only the gross average characteristics of the underlying processes. By contrast, the EGF method is more effective in isolating the source effects, although it does require a good selection of EGF events of appropriate mechanism, location and size. A lack of suitable EGF earthquakes can lead to biased estimates of f_c (e.g. Abercrombie, 2015; Wu and Chapman, 2017). For example, because EGF earthquakes are small, they have low SNR and may have significant bandwidth limitations. This limits the number of useable stations and may lead to large gaps in azimuthal coverage (Holmgren et al., 2019; Shearer et al., 2019). The GMPE method avoids this limitation because it does not require the availability of smaller EGF events; for the GMPE method, we require sufficient SNR only for the target earthquakes.

In order to further investigate how EGF $\Delta\sigma_{drop}$ and GMPE $\Delta\sigma_{par}$ differ, we compare the ratios between individual record EGF f_c and GMPE f_c . The ratios were divided into bins to examine different source parameters. Using the Student's t -test (Student, 1908), no statistical significance was found when comparing mean ratios for different magnitude bins, or different hypocentral distance bins. However, we observe differences in results related to the rupture direction when comparing EGF and GMPE f_c values. Figure 4.11 shows the ratio of EGF record f_c to GMPE f_c as a function of angle from rupture direction for the 39 earthquakes with resolvable directivity, color coded based on the relative station azimuth to the horizontal rupture direction (where 0° is the rupture direction). For stations located in the forward rupture direction ($0^\circ \pm 45^\circ$), the EGF method tends to produce higher f_c measurements, with a geomean and standard error of 1.6 ± 0.2 . On the other hand, for stations located in the backward rupture direction ($180^\circ \pm 45^\circ$), the two methods produced similar f_c values with a geomean and standard error of 0.9 ± 0.2 . This suggests that the GMPE method may underestimate corner frequency for records with enhanced high-frequency content due to forward directivity. The rich high-frequency content in the forward directivity azimuths is filtered by path and site effects in the GMPE method, making it difficult to obtain the true corner. The GMPE method does recover some indication of directivity (as seen by the within-event residuals in Figure 4.8), but it is

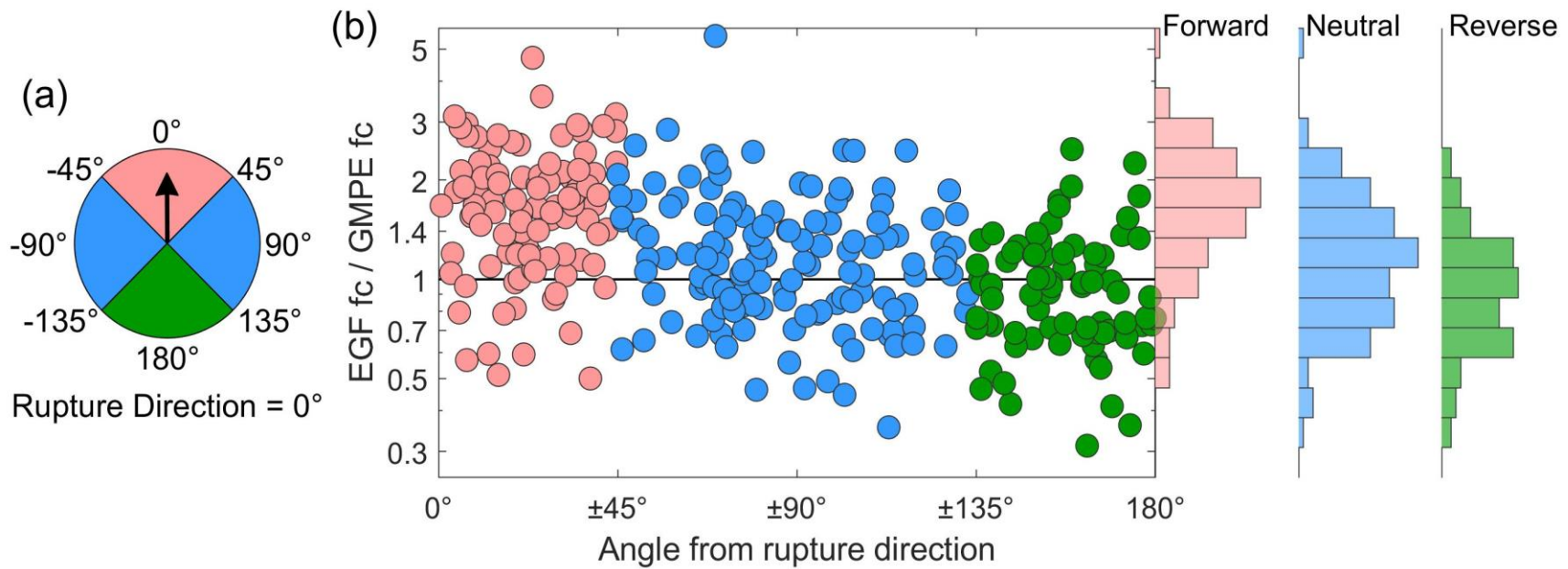


Figure 4.11. Comparison of f_c by record between the EGF method and the GMPE method. (a) Schematic view of the three schematic azimuth quadrants w.r.t. horizontal rupture direction: records within $0^\circ \pm 45^\circ$ are in the forward direction; records within $180^\circ \pm 45^\circ$ are in the backward direction; and remaining records are in the neutral direction. (b) Ratios of EGF f_c to GMPE f_c (circles) plotted as a function of horizontal angle away from rupture direction, shaded based on quadrant from (a). Histograms showing the ratio distributions can be seen on the right.

smearred out relative to that seen by the EGF method. We also investigate whether using only posthole or surface stations impacted the EGF-GMPE f_c ratios. No significant difference was found in the recovered values of corner frequency when subdivided based on station type, indicating that these effects were successfully removed through the station terms F_S .

Baltay et al. (2013) used natural earthquakes to compare stress drops obtained using the EGF method to a_{rms} stress parameters obtained from the acceleration Fourier spectrum. They found that the two methods produced comparable estimates of stress for earthquakes with $M \geq 3.0$ at close distances ($R \leq 20$ km). The a_{rms} method requires that the cutoff frequency f_{max} (Hanks, 1982) be sufficiently larger than f_c , which only occurs for relatively large earthquakes at close distances. Considering the sparse regional station coverage and lack of data within 20 km (30 records out of 643 in total), the a_{rms} method is not applicable for this region.

The variability in the values of $\Delta\sigma_{par}$ is slightly less than that for $\Delta\sigma_{drop}$, as seen in Figure 4.9. The $\Delta\sigma_{par}$ distribution has a standard deviation of 1.1 natural-log units, whereas the $\Delta\sigma_{drop}$ variability is 1.6 natural-log units. Cotton et al. (2013) compared $\Delta\sigma_{par}$ distributions from the between-event terms of GMPE studies to $\Delta\sigma_{drop}$ values from source studies that determined corner frequency, and found that the GMPE $\Delta\sigma_{par}$ variabilities were much lower than those for $\Delta\sigma_{drop}$ (0.3 to 0.6 ln units for $\Delta\sigma_{par}$ versus 0.6 to 1.8 for $\Delta\sigma_{drop}$). The larger variability for $\Delta\sigma_{drop}$ is partly due to its dependence on f_c^3 (Equation 4.6); a small error in f_c will lead to a large error in $\Delta\sigma_{drop}$. Our results are consistent with this finding. Our $\Delta\sigma_{par}$ variability is larger than that obtained by Cotton et al. (2013), perhaps because we compute stress parameter by fitting the GMPE to the entire response spectrum, whilst Cotton et al. (2013) used a single ground motion measure (i.e. PGA). Overall, we note that both our $\Delta\sigma_{drop}$ and $\Delta\sigma_{par}$ variabilities are large relative to those observed in other studies (e.g. Oth et al., 2017). This may reflect a combination of effects, including higher source variability in the attributes of events induced by hydraulic fracturing, and complex path and site effects, including directivity, that interact with a

sparse station distribution. Holmgren et al. (2019) noted that 21 out of 92 earthquakes displayed source complexity in the form of deviations from a typical Brune model, likely due to rupture of multiple faults (Wang et al., 2018; Eyre et al., 2019). Resolvable directivity was observed for 39 out of the 92 earthquakes, which led to an average f_c difference of a factor of 4 depending on azimuth (Holmgren et al., 2019). 40 of the 92 earthquakes did not have sufficient bias in the f_c estimates due to directivity effects, leading to large $\Delta\sigma_{drop}$ and $\Delta\sigma_{par}$ variability.

In this study, we developed our GMPE using a stress model that explicitly assumed a relationship between the values of the stress parameter and the EGF stress drop (Figure 4.2); the input stress model to the GMPE was slightly scaled (factor of 1.3) version of a line fit to the EGF stress drop values. We examined the sensitivity of results to this assumption. Interestingly, changing the initial stress model affects the final calibration factor C , but not the site terms F_S or the overall residuals between the GMPE and observed data. Any mismatch between the ideal form of the stress model and that assumed in the GMPE development is mapped entirely into C . This means that the stress model does not need to be known in advance of developing a regional-specific GMPE, but can either be obtained through fitting a model to stress drops from an existing source study in the region, or by simply assuming a constant 100 bars from the default source model (Yenier et al., 2015a). Specifically, we repeated the GMPE development assuming an input stress model of 100 bars for all events; the inversion returned the same site terms and residuals as reported here; only the calibration function and stress parameter values changed. If a stress model producing $\Delta\sigma_{par}$ similar to published $\Delta\sigma_{drop}$ is preferred, the stress model (starting initially with 100 bars, or with a $\Delta\sigma_{drop}$ model from EGF studies as was done here) can be iterated until $\Delta\sigma_{par}$ and $\Delta\sigma_{drop}$ are consistent.

4.7 Conclusion

We develop a region-specific GMPE for induced earthquakes in WCSB of M2.3-4.4 to distances of 200 km using published EGF stress drop estimates ($\Delta\sigma_{drop}$) as a proxy for an input stress parameter ($\Delta\sigma_{par}$) model. The use of the generic GMPE model ensures

reasonable scaling of motions to larger magnitudes (Yenier and Atkinson, 2015a). By constraining the input stress model to approximately follow the results from EGF source studies, we ensured agreement on average between the GMPE- and EGF-based values of stress. Moreover, our approach recognizes that EGF-based source parameters are inherently more robust (when available). We compared individual earthquake $\Delta\sigma_{par}$ estimates obtained by fitting response spectra to the GMPE to $\Delta\sigma_{drop}$ values in order to investigate differences between the parameters. Significant event-to-event variability is found, which we attribute to: (i) response spectra and Fourier spectra are not linearly related and thus $\Delta\sigma_{drop}$ and $\Delta\sigma_{par}$ values are not directly equivalent (Bora et al., 2016); (ii) GMPEs are non-unique due to trade-offs between parameters, which represent only average regional effects, and are thus inherently limited in their ability to resolve source parameters. In particular, we noted that the GMPE method returned lower f_c estimates than the EGF method in the forward rupture direction, whilst returning similar values in the backward direction.

When using estimates of stress drop to infer high-frequency amplitudes of ground motion, the conventions linking stress drop to corner frequency are critical. It is best to consider corner frequency as the fundamental ground-motion parameter controlling high-frequency content. Moreover, it should be noted that directivity effects can exert a profound effect on corner frequency, in both the EGF and GMPE approaches, and thus source parameters estimated from a sparse station distribution may be highly uncertain. Nonetheless, we have shown that $\Delta\sigma_{drop}$ from EGF studies can be used as an input $\Delta\sigma_{par}$ model in GMPE development. This also allows the possibility of using a distribution of $\Delta\sigma_{drop}$ values from published studies available in the literature when developing region-specific GMPEs.

Chapter 5

5 Conclusions and Future Studies

5.1 Summary and Conclusions

In this thesis, I examined how source parameters of induced earthquakes affect the high-frequency content of ground motions and the variability of ground-motion prediction equations (GMPEs).

In Chapter 2, I analyzed how the aleatory uncertainty (sigma, σ) is affected by small perturbations in the source parameters (magnitude and location) for induced earthquakes in Central United States (CUS). Sigma plays a large role in hazard assessment; large uncertainties in GMPEs leads to larger ranges of possible outcomes to be considered. Therefore, reducing sigma has been a topic of interest for numerous studies (e.g., Rhoades, 1997; Atkinson, 2006; Bindi et al., 2006; Derras et al., 2016). We set out to minimize sigma by finding the ground-motion center (GMC) for each earthquake studied, where the GMC was defined as the location and magnitude that results in the smallest residuals and thus the lowest sigma. The GMC is essentially the location and magnitude preferred by the GMPE. First, to reduce the epistemic uncertainty, a zero-biased GMPE was developed by applying a distance-correction term and station terms to the Atkinson (2015) GMPE. Next, we used a grid search technique to iteratively find each earthquake's GMC. The total sigma and its components, the between- (τ) and within-event (ϕ) terms, were analyzed for both initial and final residuals. We found that sigma could be reduced on average by 61%, which is a significant decrease in aleatory uncertainty. More specifically, τ and ϕ decreased by 84% and 25%, respectively, on average. In other words, a change in magnitude led to larger sigma reductions than a change in location. The difference could reflect other source parameters not included in the GMPE that influence the ground motion amplitudes, like stress drop/stress parameter. The GMC magnitude implicitly includes stress drop effects.

In Chapter 3, we narrowed the focus to study the source parameter stress drop and its model components. We performed a broad-scale Empirical Green's Function (EGF)

study in the Western Canada Sedimentary Basin (WCSB) in order to analyze the source properties of its induced earthquakes from the Brune (1970, 1971) source perspective. The EGF approach is generally seen as advantageous compared to other source modelling methods because it does not require prior knowledge of the path and site effects in the region (e.g., Ide et al., 2003). Instead, path and site components are removed through spectral division by a smaller, collocated earthquake. We were able to retrieve corner frequencies and stress drops for 87 earthquakes in the WCSB. Clear azimuthal variation of corner frequencies was observed between records. In the traditional EGF approach, azimuthal variations are assumed to cancel out (e.g. Abercrombie, 2015). However, the station distribution for the WCSB was not sufficient to follow this approach. Instead, we used the Haskell (1964) directivity model to estimate the corner frequencies of earthquakes. We found that 37 earthquakes exhibited rupture directivity patterns, 13 earthquakes had no apparent azimuthal variation, and 37 earthquakes had too few records to determine azimuthal variation. For the 37 earthquakes with resolvable directivity, we determined the azimuth of the rupture and were able to match them to focal mechanism solutions (Figure 3.8), demonstrating that corner frequencies from a range of station azimuths can be used to determine fault planes from auxiliary planes. Furthermore, from the shapes of the spectral ratios and source time functions, we were able to detect 19 complex induced earthquakes that deviated from the typical models. A majority of these also exhibited directivity, which could be explained as the rupture triggering multiple faults during its slip (e.g., López-Comino et al., 2018).

After converting the corner frequencies to stress drop assuming the Madariaga (1976) k -model, we obtained values ranging between 0.2-98 MPa with an outlier at 370 MPa. Tectonic earthquakes have similar stress drop ranges (0.1-100 MPa, e.g., Abercrombie, 1995); this very broad range reflects the large variability that is typical in source studies (e.g., Abercrombie, 2015; Kaneko et al., 2015), which can be attributed to many factors. We examined how the value obtained for stress drop is highly sensitive to the assumed focal depth by comparing stress drop values assuming a depth of 3 and 4 km, typical values for WCSB induced earthquakes (e.g., Eaton et al., 2018; Wang et al., 2018); these alternative depth assumptions result in average stress drops of 21.0 and 7.8 MPa, respectively.

In Chapter 4, we investigated how well stress drops ($\Delta\sigma_{drop}$) from an EGF study could be used as a proxy for stress parameter ($\Delta\sigma_{par}$) when developing a regional GMPE. First, using the database and results from Chapter 3, we defined a $\Delta\sigma_{par}$ model based on the $\Delta\sigma_{drop}$ estimates. Then, we followed the generic GMPE approach of Yenier and Atkinson (2015a, 2015b) to develop a WCSB region-specific GMPE. In order to investigate the effects of directivity on ground motions and response spectra, we analyzed the residuals between the GMPE and the ground motion data, with a focus on the earthquakes from Chapter 3 with resolvable directivity. We found that directivity has an effect on the within-event component of sigma.

Finally, we used the WCSB GMPE to estimate $\Delta\sigma_{par}$ for each record and earthquake in order to compare them to the equivalent $\Delta\sigma_{drop}$ values to see whether they provide similar measures of ground motion at high frequency. While the $\Delta\sigma_{drop}$ and $\Delta\sigma_{par}$ were on average the same because of how we defined the input stress model (see Figure 4.2), a large scatter was still observed. This scatter was partly associated with the fact that $\Delta\sigma_{drop}$ is measured in the Fourier domain and $\Delta\sigma_{par}$ is measured in the response domain, which are physically different (e.g., Bora et al., 2016). Another large contributor to the scatter is that GMPEs are non-unique and are subject to trade-offs between source and site models. As a last check, we investigated individual record corner frequencies obtained from both $\Delta\sigma_{drop}$ and $\Delta\sigma_{par}$, and found that while both methods show evidence of rupture directivity patterns, the GMPE corner frequency returned lower values of corner frequency in the forward rupture direction, probably due to the band-limiting influence of site or path effects. Nonetheless, once station corner frequencies were averaged over the event, the two methods provided similar values and thus both are good measures of the high-frequency content of earthquakes - subject to the caveats noted with regards to absolute values.

The most significant and novel conclusions of this thesis are:

- Much of the calculated GMPE variability may be attributed to uncertainty in source parameters with respect to values preferred by a GMPE. Provided that source parameter variability is already reflected in a GMPE's epistemic uncertainty, we

can remove the contributions that come from source parameters in the aleatory model and thereby reduce sigma.

- A change in magnitude has a larger effect on the overall sigma, than does a change in location.
- Directivity plays an important role in ground motion, even for small events ($M < 4$).
- Station corner frequencies varied on average by a factor of 4 between the forward and backward rupture directions, which may lead to either under- or overestimation of the earthquake's corner frequency for events that are not observed over a sufficient azimuthal range.
- For regions with sparse station coverage, the corner frequency can be estimated using a combination of the EGF method and the Haskell (1964) directivity method. This approach can lead to improved estimates of corner frequency and stress drop.
- Stress drop should not be considered as an absolute value because it is highly dependent on the assumed parameters and constants of the underlying physical models. Instead, corner frequency is a more fundamental and useful source parameter.
- Stress drops from EGF studies can be used as a proxy for stress parameters when developing regional GMPEs.
- The within-event term of earthquakes displaying directivity has azimuthal dependency in response spectra. PSA within-event residuals for frequencies above 5.0 Hz were on average 1.5 times higher in the forward rupture direction in comparison to those in the backward rupture direction.
- While the stress parameter derived from response spectra can detect directivity, the stress drop obtained from EGF studies is much more efficient at capturing the change in high-frequency content due to azimuth.

5.2 Suggestions for future study

The topic areas explored in this thesis could best be explored further using data from dense local arrays, which would allow more detailed examination of source properties. For example, numerous studies have found that fixing the exponent $n = 2$ of the Brune source model (see Equation 3.1) may exert significant influence on the obtained source parameters (e.g., Kaneko et al., 2014; Uchide et al., 2016; Trugman et al., 2017; Lin and Lapusta, 2018; Van Houtte and Denolle, 2018). It would be useful to redo the EGF study in Chapter 3, but with a denser array of local station data, to test the extent to which corner frequencies and stress drop results may be sensitive to this basic source model assumption. Similarly, differences between corner frequencies computed using the traditional EGF approach and corner frequencies from the Haskell directivity model approach could be compared in more detail with either a dense local array, or with the data from the Oklahoma array used in Chapter 2. Another source parameter that could be studied in more detail is source complexity, and whether it can be linked with non-double couple components as obtained in moment tensor studies (e.g. Wang et al., 2018).

A dense local data set would also allow one to explore the $a_{rms} \Delta\sigma_{par}$ (e.g., Baltay et al., 2013), and see how it relates to the GMPE $\Delta\sigma_{par}$. This could provide further insight as to how stress parameters should be chosen when developing GMPEs. Additionally, by computing $\Delta\sigma_{drop}$ using the same path- and site-models as the GMPE, it would be possible to further investigate how the Fourier and response domains affect the resultant stress values. A denser array would also make it possible to investigate spatial and temporal links between the induced earthquakes and the hydraulic fracturing operations. Such additional studies would require the availability of data from dense local arrays; these data have been recorded but are largely proprietary to date.

Finally, as a further investigation of rupture directivity, station records for which the rupture direction is known could be rotated into radial and tangential components, and these components could be compared to theoretical directivity models.

Bibliography

- Abercrombie, R. E. (1995). Earthquake Source Scaling Relationships from -1 to 5 ML Using Seismograms Recorded at 2.5-Km Depth. *J. Geophys. Res.*, 100(B12), 24015–24036.
- Abercrombie, R. E. (2014). Stress Drops of Repeating Earthquakes on the San Andreas Fault at Parkfield. *Geophys. Res. Lett.*, 41(24), 8784–8791.
- Abercrombie, R. E. (2015). Investigating Uncertainties in Empirical Green's Function Analysis of Earthquake Source Parameters. *J. Geophys. Res. Solid Earth*, 120(6), 4263–4277.
- Abercrombie, R. E., Bannister, S., Ristau, J., and Doser, D. I. (2017). Variability of Earthquake Stress Drop in a Subduction Setting, the Hikurangi Margin, New Zealand. *Geophys. J. Int.*, 208(1), 306–320.
- Abercrombie, R. E., and Leary, P. (1993). Source Parameters of Small Earthquakes Recorded at 2.5 Km Depth, Cajon Pass, Southern California: Implications for Earthquake Scaling. *Geophys. Res. Lett.*, 20(14), 1511–1514.
- Abercrombie, R. E., Poli, P., and Bannister, S. (2017). Earthquake Directivity, Orientation, and Stress Drop within the Subducting Plate at the Hikurangi Margin, New Zealand. *J. Geophys. Res. Solid Earth*, 122, 10,176–10,188.
- Abercrombie, R. E., and Rice, J. R. (2005). Can Observations of Earthquake Scaling Constrain Slip Weakening? *Geophys. J. Int.*, 162(2), 406–424.
- Abrahamson, N. A. (1988). Statistical Properties of Peak Ground Accelerations Recorded by the SMART 1 Array. *Bull. Seismol. Soc. Am.*, 78(1), 26–41.
- Abrahamson, N. A., and Silva, W. J. (1997). Empirical Response Spectral Attenuation Relations for Shallow Crustal Earthquakes. *Seismol. Res. Lett.*, 68(1), 94–127.
- Abrahamson, N. A., and Silva, W. J. (2007). Abrahamson & Silva NGA Ground Motion Relation for the Geometric Mean Horizontal Component of Peak and Spectral Ground Motion Parameters. In *Pacific Earthquake Research Center Report*. Berkeley.
- Abrahamson, N. A., Silva, W. J., and Kamai, R. (2014). Summary of the ASK14 Ground

- Motion Relation for Active Crustal Regions. *Earthq. Spectra*, 30(3), 1025–1055.
- Abrahamson, N. A., and Somerville, P. G. (1996). Effects of the Hanging Wall and Footwall on Ground Motions Recorded during the Northridge Earthquake. *Bull. Seismol. Soc. Am.*, 86(1B), S93–S99.
- Aki, K. (1967). Scaling Law of Seismic Spectrum. *J. Geophys. Res.*, 72(4), 1217–1231.
- Aki, K., and Richards, P. G. (1980). *Quantitative Seismology: Theory and Methods*. San Francisco, California: W. H. Freeman and Company.
- Al Atik, L., Abrahamson, N. A., Bommer, J. J., Scherbaum, F., Cotton, F., and Kuehn, N. M. (2010). The Variability of Ground-Motion Prediction Models and Its Components. *Seismol. Res. Lett.*, 81(5), 794–801.
- Allmann, B. P., and Shearer, P. M. (2009). Global Variations of Stress Drop for Moderate to Large Earthquakes. *J. Geophys. Res. Solid Earth*, 114(1), 1–22.
- Alt, R. C., and Zoback, M. D. (2017). In Situ Stress and Active Faulting in Oklahoma. *Bull. Seismol. Soc. Am.*, 107(1), 216–228.
- Ambraseys, N. N., Douglas, J., Sarma, S. K., and Smit, P. M. (2005). Equations for the Estimation of Strong Ground Motions from Shallow Crustal Earthquakes Using Data from Europe and the Middle East: Horizontal Peak Ground Acceleration and Spectral Acceleration. *Bull. Earthq. Eng.*, 3(1), 1–53.
- Anderson, E. M. (1905). The Dynamics of Faulting. *Trans. Edinburgh Geol. Soc.*, 8(3), 387–402.
- Archuleta, R. J., and Ji, C. (2016). Moment Rate Scaling for Earthquakes $3.3 \leq M \leq 5.3$ with Implications for Stress Drop. *Geophys. Res. Lett.*, 43(23), 12,004–12,011.
- Assatourians, K., and Atkinson, G. M. (2010). Database of Processed Time Series and Response Spectra Data for Canada: An Example Application to Study of 2005 M_w 5.4 Riviere Du Loup, Quebec, Earthquake. *Seismol. Res. Lett.*, 81(6), 1013–1031.
- Atkinson, G. M. (1993). Earthquake Source Spectra in Eastern North America. *Bull. Seismol. Soc. Am.*, 83(6), 1778–1798.
- Atkinson, G. M. (2004). Empirical Attenuation of Ground-Motion Spectral Amplitudes in

- Southeastern Canada and the Northeastern United States. *Bull. Seismol. Soc. Am.*, 94(3), 1079–1095.
- Atkinson, G. M. (2006). Single-Station Sigma. *Bull. Seismol. Soc. Am.*, 96(2), 446–455.
- Atkinson, G. M. (2008). Ground-Motion Prediction Equations for Eastern North America from a Referenced Empirical Approach: Implications for Epistemic Uncertainty. *Bull. Seismol. Soc. Am.*, 98(3), 1304–1318.
- Atkinson, G. M. (2013). Empirical Evaluation of Aleatory and Epistemic Uncertainty in Eastern Ground Motions. *Seismol. Res. Lett.*, 84(1), 130–138.
- Atkinson, G. M. (2015). Ground-Motion Prediction Equation for Small-to-Moderate Events at Short Hypocentral Distances, with Application to Induced-Seismicity Hazards. *Bull. Seismol. Soc. Am.*, 105(2), 981–992.
- Atkinson, G. M., and Assatourians, K. (2017). Are Ground-Motion Models Derived from Natural Events Applicable to the Estimation of Expected Motions for Induced Earthquakes? *Seismol. Res. Lett.*, 88(2), 430–441.
- Atkinson, G. M., Assatourians, K., Cheadle, B., and Greig, D. W. (2015). Ground Motions from Three Recent Earthquakes in Western Alberta and Northeastern British Columbia and Their Implications for Induced-Seismicity Hazard in Eastern Regions. *Seismol. Res. Lett.*, 86(3), 1022–1031.
- Atkinson, G. M., and Beresnev, I. A. (1997). Don't Call It Stress Drop. *Seismol. Res. Lett.*, 68(1), 3–4.
- Atkinson, G. M., and Boore, D. M. (1997). Stochastic Point-Source Modeling of Ground Motions in the Cascadia Region. *Seismol. Res. Lett.*, 68(1), 74–85.
- Atkinson, G. M., and Boore, D. M. (2006). Earthquake Ground-Motion Prediction Equations for Eastern North America. *Bull. Seismol. Soc. Am.*, 96(6), 2181–2205.
- Atkinson, G. M., Eaton, D. W., Ghofrani, H., Walker, D., Cheadle, B., Schultz, R., ... Kao, H. (2016). Hydraulic Fracturing and Seismicity in the Western Canada Sedimentary Basin. *Seismol. Res. Lett.*, 87(3), 631–647.
- Atkinson, G. M., Ghofrani, H., and Assatourians, K. (2015). Impact of Induced Seismicity

- on the Evaluation of Seismic Hazard: Some Preliminary Considerations. *Seismol. Res. Lett.*, 86(3), 1009–1021.
- Atkinson, G. M., Hassani, B., Singh, A., Yenier, E., and Assatourians, K. (2015). Estimation of Moment Magnitude and Stress Parameter from ShakeMap Ground-Motion Parameters. *Bull. Seismol. Soc. Am.*, 105(5), 2572–2588.
- Atkinson, G. M., and Mereu, R. F. (1992). The Shape of Ground Motion Attenuation Curves in Southeastern Canada. *Bull. Seismol. Soc. Am.*, 82(5), 2014–2031.
- Bakun, W. H., and Bufe, C. G. (1975). Shear-Wave Attenuation Along the San Andreas Fault Zone in Central California. *Bull. Seismol. Soc. Am.*, 65(2), 439–459.
- Baltay, A. S., Hanks, T. C., and Abrahamson, N. A. (2017). Uncertainty, Variability, and Earthquake Physics in Ground-Motion Prediction Equations. *Bull. Seismol. Soc. Am.*, 107(4), 1754–1772.
- Baltay, A. S., Hanks, T. C., and Abrahamson, N. A. (2019). Earthquake Stress Drop and Arias Intensity. *J. Geophys. Res. Solid Earth*, 124(4), 3838–3852.
- Baltay, A. S., Hanks, T. C., and Beroza, G. C. (2013). Stable Stress-Drop Measurements and Their Variability: Implications for Ground-Motion Prediction. *Bull. Seismol. Soc. Am.*, 103(1), 211–222.
- Baltay, A. S., Prieto, G. A., and Beroza, G. C. (2010). Radiated Seismic Energy from Coda Measurements and No Scaling in Apparent Stress with Seismic Moment. *J. Geophys. Res. Solid Earth*, 115(8), 1–12.
- Bao, X., and Eaton, D. W. (2016). Fault Activation by Hydraulic Fracturing in Western Canada. *Science (80-.)*, 354(6318), 1406–1409.
- Benioff, H. (1934). The Physical Evaluation of Seismic Destructiveness. *Bull. Seismol. Soc. Am.*, 24(4), 398–403.
- Benioff, H. (1955). Mechanism and Strain Characteristics of the White Wolf Fault as Indicated by the Aftershock Sequence, Earthquakes in Kern County, California during 1955. *Bull. Calif. Div. Mines Geol.*, 171, 199–202.
- Bindi, D., Luzi, L., Pacor, F., Franceschina, G., and Castro, R. R. (2006). Ground-Motion

- Predictions from Empirical Attenuation Relationships versus Recorded Data: The Case of the 1997-1998 Umbria-Marche, Central Italy, Strong-Motion Data Set. *Bull. Seismol. Soc. Am.*, 96(3), 984–1002.
- Bindi, D., Parolai, S., Grosser, H., Milkereit, C., and Durukal, E. (2007). Empirical Ground-Motion Prediction Equations for Northwestern Turkey Using the Aftershocks of the 1999 Kocaeli Earthquake. *Geophys. Res. Lett.*, 34(8), L08305.
- Bindi, D., Spallarossa, D., and Pacor, F. (2017). Between-Event and between-Station Variability Observed in the Fourier and Response Spectra Domains: Comparison with Seismological Models. *Geophys. J. Int.*, 210(2), 1092–1104.
- Biot, M. A. (1941). A Mechanical Analyzer for the Prediction of Earthquake Stresses. *Bull. Seismol. Soc. Am.*, 31(2), 151–171.
- Boatwright, J. (1980). A Spectral Theory for Circular Seismic Sources; Simple Estimates of Source Dimension, Dynamic Stress Drop, and Radiated Seismic Energy. *Bull. Seismol. Soc. Am.*, 70(1), 1–27.
- Boatwright, J. (1988). The Seismic Radiation from Composite Models of Faulting. *Bull. Seismol. Soc. Am.*, 78(2), 489–508.
- Boatwright, J. (2007). The Persistence of Directivity in Small Earthquakes. *Bull. Seismol. Soc. Am.*, 97(6), 1850–1861.
- Boatwright, J., and Boore, D. M. (1982). Analysis of the Ground Accelerations Radiated by the 1980 Livermore Valley Earthquakes for Directivity and Dynamic Source Characteristics. *Bull. Seismol. Soc. Am.*, 72(6), 1843–1865.
- Boatwright, J., and Seekins, L. (2011). Regional Spectral Analysis of Three Moderate Earthquakes in Northeastern North America. *Bull. Seismol. Soc. Am.*, 101(4), 1769–1782.
- Bommer, J. J., and Abrahamson, N. A. (2006). Why Do Modern Probabilistic Seismic-Hazard Analyses Often Lead to Increased Hazard Estimates? *Bull. Seismol. Soc. Am.*, 96(6), 1967–1977.
- Boore, D. M. (1983). Stochastic Simulation of High-Frequency Ground Motions Based on

- Seismological Models of the Radiated Spectra. *Bull. Seismol. Soc. Am.*, 73(6), 1865–1894.
- Boore, D. M. (1986). Short-Period P- and S-Wave Radiation from Large Earthquakes: Implications for Spectral Scaling Relations. *Bull. Seismol. Soc. Am.*, 76(1), 43–64.
- Boore, D. M. (2003). Simulation of Ground Motion Using the Stochastic Method. *Pure Appl. Geophys.*, 160(3–4), 635–676.
- Boore, D. M., and Atkinson, G. M. (1987). Stochastic Prediction of Ground Motion and Spectral Response Parameters at Hard-Rock Sites in Eastern North America. *Bull. Seismol. Soc. Am.*, 77(2), 440–467.
- Boore, D. M., and Atkinson, G. M. (1992). Source Spectra for the 1988 Saguenay, Quebec, Earthquakes. *Bull. Seismol. Soc. Am.*, 82(2), 683–719.
- Boore, D. M., Azari Sisi, A., and Akkar, S. (2012). Using Pad-Stripped Acausally Filtered Strong-Motion Data. *Bull. Seismol. Soc. Am.*, 102(2), 751–760.
- Boore, D. M., Campbell, K. W., and Atkinson, G. M. (2010). Determination of Stress Parameters for Eight Well-Recorded Earthquakes in Eastern North America. *Bull. Seismol. Soc. Am.*, 100(4), 1632–1645.
- Boore, D. M., and Joyner, W. B. (1991). Estimation of Ground Motion at Deep-Soil Sites in Eastern North America. *Bull. Seismol. Soc. Am.*, 81(6), 2167–2185.
- Boore, D. M., Stewart, J. P., Seyhan, E., and Atkinson, G. M. (2014). NGA-West2 Equations for Predicting PGA, PGV, and 5% Damped PSA for Shallow Crustal Earthquakes. *Earthq. Spectra*, 30(3), 1057–1085.
- Bora, S. S., Scherbaum, F., Kuehn, N. M., and Stafford, P. J. (2014). Fourier Spectral- and Duration Models for the Generation of Response Spectra Adjustable to Different Source-, Propagation-, and Site Conditions. *Bull. Earthq. Eng.*, 12(1), 467–493.
- Bora, S. S., Scherbaum, F., Kuehn, N. M., and Stafford, P. J. (2016). On the Relationship between Fourier and Response Spectra: Implications for the Adjustment of Empirical Ground-Motion Prediction Equations (GMPEs). *Bull. Seismol. Soc. Am.*, 106(3), 1235–1253.

- Bosman, K., Baig, A., Viegas, G., and Urbancic, T. (2016). Towards an Improved Understanding of Induced Seismicity Associated with Hydraulic Fracturing. *First Break*, 34(7).
- Boyd, O. S., McNamara, D. E., Hartzell, S. H., and Choy, G. L. (2017). Influence of Lithostatic Stress on Earthquake Stress Drops in North America. *Bull. Seismol. Soc. Am.*, 107(2), 856–868.
- Brillinger, D. R., and Preisler, H. K. (1984). An Exploratory Analysis of the Joyner-Boore Attenuation Data. *Bull. Seismol. Soc. Am.*, 74(4), 1441–1450.
- Brown, M. R. M., Ge, S., Sheehan, A. F., and Nakai, J. S. (2017). Evaluating the Effectiveness of Induced Seismicity Mitigation: Numerical Modeling of Wastewater Injection near Greeley, Colorado. *J. Geophys. Res. Solid Earth*, 122(8), 6569–6582.
- Brune, J. N. (1970). Tectonic Stress and the Spectra of Seismic Shear Waves from Earthquakes. *J. Geophys. Res.*, 75(26), 4997–5009.
- Brune, J. N. (1971). Correction. *J. Geophys. Res.*, 76(20), 5002.
- Campbell, K. W. (1985). Strong Motion Attenuation Relations: A Ten-Year Perspective. *Earthq. Spectra*, 1(4), 759–804.
- Campbell, K. W. (2003). Prediction of Strong Ground Motion Using the Hybrid Empirical Method and Its Use in the Development of Ground-Motion (Attenuation) Relations in Eastern North America. *Bull. Seismol. Soc. Am.*, 93(3), 1012–1033.
- Campbell, K. W., and Bozorgnia, Y. (2014). NGA-West2 Ground Motion Model for the Average Horizontal Components of PGA, PGV, and 5% Damped Linear Acceleration Response Spectra. *Earthq. Spectra*, 30(3), 1087–1115.
- Chávez, D. E., and Priestley, K. F. (1986). Measurement of Frequency Dependent L g Attenuation in the Great Basin. *Geophys. Res. Lett.*, 13(6), 551–554.
- Chen, Y., Gu, Y. J., Dokht, R. M. H., and Sacchi, M. D. (2015). Crustal Imprints of Precambrian Orogenesis in Western Laurentia. *J. Geophys. Res. Solid Earth*, 120, 6993–7012.
- Clerc, F., Harrington, R. M., Liu, Y., and Gu, Y. J. (2016). Stress Drop Estimates and

- Hypocenter Relocations of Induced Seismicity near Crooked Lake, Alberta. *Geophys. Res. Lett.*, 43(13), 6942–6951.
- Cotton, F., Archuleta, R. J., and Causse, M. (2013). What Is Sigma of the Stress Drop? *Seismol. Res. Lett.*, 84(1), 42–48.
- Courboux, F., Vallée, M., Causse, M., and Chounet, A. (2016). Stress-Drop Variability of Shallow Earthquakes Extracted from a Global Database of Source Time Functions. *Seismol. Res. Lett.*, 87(4), 912–918.
- Dahm, T., Krüger, F., Stammler, K., Klinge, K., Kind, R., Wylegalla, K., and Grasso, J.-R. (2007). The 2004 Mw 4.4 Rotenburg, Northern Germany, Earthquake and Its Possible Relationship with Gas Recovery. *Bull. Seismol. Soc. Am.*, 97(3), 691–704.
- Derras, B., Bard, P.-Y., and Cotton, F. (2016). Site-Condition Proxies, Ground Motion Variability, and Data-Driven GMPEs: Insights from the NGA-West2 and RESORCE Data Sets. *Earthq. Spectra*, 32(4), 2027–2056.
- Douglas, J. (2017). *Ground motion prediction equations 1964-2017*.
- Drouet, S., and Cotton, F. (2015). Regional Stochastic GMPEs in Low-Seismicity Areas: Scaling and Aleatory Variability Analysis—Application to the French Alps. *Bull. Seismol. Soc. Am.*, 105(4), 1883–1902.
- Eaton, D. W. (2018). *Passive Seismic Monitoring of Induced Seismicity*. Cambridge University Press.
- Eaton, D. W., Igonin, N., Poulin, A., Weir, R., Zhang, H., Pellegrino, S., and Rodriguez, G. (2018). Induced Seismicity Characterization during Hydraulic-Fracture Monitoring with a Shallow-Wellbore Geophone Array and Broadband Sensors. *Seismol. Res. Lett.*, 89(5), 1641–1651.
- Edwards, B., and Fäh, D. (2013). A Stochastic Ground-Motion Model for Switzerland. *Bull. Seismol. Soc. Am.*, 103(1), 78–98.
- Efron, B. (1979). Bootstrap Methods: Another Look at the Jackknife. *Ann. Stat.*, 7, 1–26.
- Ellsworth, W. L. (2013). Injection-Induced Earthquakes. *Science* (80-.), 341(1225942).
- Eshelby, J. D. (1957). The Determination of the Elastic Field of an Ellipsoidal Inclusion,

- and Related Problems. *Proc. R. Soc.*, 241(1226), 376–396.
- Eyre, T. S., Eaton, D. W., Zecevic, M., D’Amico, D., and Kolos, D. (2019). Microseismicity Reveals Fault Activation before Mw 4.1 Hydraulic-Fracturing Induced Earthquake. *Geophys. J. Int.*, 218(1), 534–546.
- Farrugia, J. J., Molnar, S., and Atkinson, G. M. (2017). Noninvasive Techniques for Site Characterization of Alberta Seismic Stations Based on Shear-Wave Velocity. *Bull. Seismol. Soc. Am.*, 107(6), 2885–2902.
- Folesky, J., Kummerow, J., Shapiro, S. A., Häring, M., and Asanuma, H. (2016). Rupture Directivity of Fluid-Induced Microseismic Events: Observations from an Enhanced Geothermal System. *J. Geophys. Res. Solid Earth*, 121(11), 8034–8047.
- Foulger, G. R., Wilson, M. P., Gluyas, J. G., Julian, B. R., and Davies, R. J. (2018). Global Review of Human-Induced Earthquakes. *Earth-Science Rev.*, 178, 438–514.
- Grigoli, F., Cesca, S., Priolo, E., Rinaldi, A. P., Clinton, J. F., Stabile, T. A., ... Dahm, T. (2017). Current Challenges in Monitoring, Discrimination, and Management of Induced Seismicity Related to Underground Industrial Activities: A European Perspective. *Rev. Geophys.*, 55(2), 310–340.
- Gupta, A., Baker, J. W., and Ellsworth, W. L. (2017). Assessing Ground-Motion Amplitudes and Attenuation for Small-To-Moderate Induced and Tectonic Earthquakes in the Central and Eastern United States. *Seismol. Res. Lett.*, 88(5), 1379–1389.
- Gupta, I. N., and McLaughlin, K. L. (1987). Attenuation of Ground Motion in the Eastern United States. *Bull. Seismol. Soc. Am.*, 77(2), 366–383.
- Gusev, A. A. (1983). Descriptive Statistical Model of Earthquake Source Radiation and Its Application to an Estimation of Short-period Strong Motion. *Geophys. J. R. Astron. Soc.*, 74(3), 787–808.
- Hanks, T. C. (1979). B Values and Ω - γ Seismic Source Models: Implications for Tectonic Stress Variations along Active Crustal Fault Zones and the Estimation of High-frequency Strong Ground Motion. *J. Geophys. Res.*, 84(B5), 2235–2242.

- Hanks, T. C. (1982). F_{max} . *Bull. Seismol. Soc. Am.*, 72(6), 1867–1879.
- Hanks, T. C., and Kanamori, H. (1979). A Moment Magnitude Scale. *J. Geophys. Res. B Solid Earth*, 84(B5), 2348–2350.
- Hanks, T. C., and McGuire, R. K. (1981). The Character of High-Frequency Strong Ground Motion. *Bull. Seismol. Soc. Am.*, 71(6), 2071–2095.
- Hardebeck, J. L., and Aron, A. (2009). Earthquake Stress Drops and Inferred Fault Strength on the Hayward Fault, East San Francisco Bay, California. *Bull. Seismol. Soc. Am.*, 99(3), 1801–1814.
- Harrington, R. M., and Brodsky, E. E. (2009). Source Duration Scales with Magnitude Differently for Earthquakes on the San Andreas Fault and on Secondary Faults in Parkfield, California. *Bull. Seismol. Soc. Am.*, 99(4), 2323–2334.
- Hartzell, S. H. (1978). Earthquake Aftershocks as Green's Functions. *Geophys. Res. Lett.*, 5(1), 1–4.
- Haskell, N. A. (1964). Total Energy and Energy Spectral Density of Elastic Wave Radiation from Propagating Faults. *Bull. Seismol. Soc. Am.*, 54(6), 1811–1841.
- Hatch, R. L., Abercrombie, R. E., Ruhl, C. J., and Smith, K. D. (2018). Earthquake Interaction, Fault Structure, and Source Properties of a Small Sequence in 2017 near Truckee, California. *Bull. Seismol. Soc. Am.*, 108(5), 2580–2593.
- Héloïse, C., Bard, P.-Y., and Rodriguez-Marek, A. (2012). Site Effect Assessment Using KiK-Net Data: Part 1. A Simple Correction Procedure for Surface/Downhole Spectral Ratios. *Bull. Earthq. Eng.*, 10(2), 421–448.
- Higley, D. K., Gaswirth, S. B., Abbott, M. M., Charpentier, R. R., Cook, T. A., Ellis, G. S., ... Schenk, C. J. (2011). Assessment of Undiscovered Oil and Gas Resources of the Anadarko Basin Province of Oklahoma, Kansas, Texas, and Colorado, 2010. In *USGS Publication: Digital Data Series 69-EE*.
- Hollender, F. (2019). *Improvement of practices for a more robust site-specific seismic hazard assessment*. Université Grenoble Alpes.
- Holmgren, J. M., Atkinson, G. M., and Ghofrani, H. (2019). Stress Drops and Directivity

- of Induced Earthquakes in the Western Canada Sedimentary Basin. *Bull. Seismol. Soc. Am.*, 109(5), 1635–1652.
- Hough, S. E. (2014). Shaking from Injection-Induced Earthquakes in the Central and Eastern United States. *Bull. Seismol. Soc. Am.*, 104(5), 2619–2626.
- Hough, S. E., and Page, M. (2015). A Century of Induced Earthquakes in Oklahoma? *Bull. Seismol. Soc. Am.*, 105(6), 2863–2870.
- Howell, B. F. J. (1981). On the Saturation of Earthquake Magnitudes. *Bull. Seismol. Soc. Am.*, 71(5), 1401–1422.
- Hua, W., Chen, Z., and Zheng, S. (2013). Source Parameters and Scaling Relations for Reservoir Induced Seismicity in the Longtan Reservoir Area. *Pure Appl. Geophys.*, 170(5), 767–783.
- Hua, W., Fu, H., Chen, Z., Zheng, S., and Yan, C. (2015). Reservoir-Induced Seismicity in High Seismicity Region—a Case Study of the Xiaowan Reservoir in Yunnan Province, China. *J. Seismol.*, 19(2), 567–584.
- Huang, Y., Beroza, G. C., and Ellsworth, W. L. (2016). Stress Drop Estimates of Potentially Induced Earthquakes in the Guy-Greenbrier Sequence. *J. Geophys. Res. Solid Earth*, 121, 1–11.
- Huang, Y., Ellsworth, W. L., and Beroza, G. C. (2017). Stress Drops of Induced and Tectonic Earthquakes in the Central United States Are Indistinguishable. *Sci. Adv.*, 3(8), 1–7.
- Ide, S., Beroza, G. C., Prejean, S. G., and Ellsworth, W. L. (2003). Apparent Break in Earthquake Scaling Due to Path and Site Effects on Deep Borehole Recordings. *J. Geophys. Res. Solid Earth*, 108(B5), ESE 16-1-13.
- Izutani, Y. (2005). Radiated Energy from the Mid Niigata, Japan, Earthquake of October 23, 2004, and Its Aftershocks. *Geophys. Res. Lett.*, 32(21), 1–4.
- Joyner, W. B., and Boore, D. M. (1981). Peak Horizontal Acceleration and Velocity from Strong-Motion Records Including Records from the 1979 Imperial Valley, California, Earthquake. *Bull. Seismol. Soc. Am.*, 71(6), 2011–2038.

- Kanamori, H. (1977). The Energy Release in Great Earthquakes. *J. Geophys. Res.*, 82(20), 2981–2987.
- Kanamori, H. (1983). Magnitude Scale and Quantification of Earthquakes. *Tectonophysics*, 93(3–4), 185–199.
- Kanamori, H. (1993). Locating Earthquakes with Amplitude: Application to Real-Time Seismology. *Bull. Seismol. Soc. Am.*, 83(1), 264–268.
- Kaneko, Y., and Shearer, P. M. (2014). Seismic Source Spectra and Estimated Stress Drop Derived from Cohesive-Zone Models of Circular Subshear Rupture. *Geophys. J. Int.*, 197(2), 1002–1015.
- Kaneko, Y., and Shearer, P. M. (2015). Variability of Seismic Source Spectra, Estimated Stress Drop, and Radiated Energy, Derived from Cohesive-Zone Models of Symmetrical and Asymmetrical Circular and Elliptical Ruptures. *J. Geophys. Res. Solid Earth*, 120(2), 1053–1079.
- Kao, H., Visser, R., Smith, B., and Venables, S. (2018). Performance Assessment of the Induced Seismicity Traffic Light Protocol for Northeastern British Columbia and Western Alberta. *Lead. Edge*, 37(2), 117–126.
- Kaski, K. M., and Atkinson, G. M. (2017). A Comparison of Ground-Motion Characteristics from Induced Seismic Events in Alberta with Those in Oklahoma. *Seismol. Res. Lett.*, 88(6), 1570–1585.
- Kettlety, T., Verdon, J. P., Werner, M. J., and Kendall, J. M. (2020). Stress Transfer From Opening Hydraulic Fractures Controls the Distribution of Induced Seismicity. *J. Geophys. Res. Solid Earth*, 125(1).
- Kotha, S. R., Bindi, D., and Cotton, F. (2016). Partially Non-Ergodic Region Specific GMPE for Europe and Middle-East. *Bull. Earthq. Eng.*, 14(4), 1245–1263.
- Kuehn, N. M., and Abrahamson, N. A. (2017). The Effect of Uncertainty in Predictor Variables on the Estimation of Ground-Motion Prediction Equations. *Bull. Seismol. Soc. Am.*, 108(1), 358–370.
- Kwiatek, G., Bulut, F., Bohnhoff, M., and Dresen, G. (2014). High-Resolution Analysis of

- Seismicity Induced at Berlín Geothermal Field, El Salvador. *Geothermics*, 52, 98–111.
- Landwehr, N., Kuehn, N. M., Scheffer, T., and Abrahamson, N. A. (2016). A Nonergodic Ground-Motion Model for California with Spatially Varying Coefficients. *Bull. Seismol. Soc. Am.*, 106(6), 2574–2583.
- Lanza, V., Spallarossa, D., Cattaneo, M., Bindi, D., and Augliera, P. (1999). Source Parameters of Small Events Using Constrained Deconvolution with Empirical Green's Functions. *Geophys. J. Int.*, 137(3), 651–662.
- Lay, T., and Wallace, T. C. (1995). *Modern Global Seismology*. Elsevier.
- Lei, X., Huang, D., Su, J., Jiang, G., Wang, X., Wang, H., ... Fu, H. (2017). Fault Reactivation and Earthquakes with Magnitudes of up to Mw4.7 Induced by Shale-Gas Hydraulic Fracturing in Sichuan Basin, China. *Sci. Rep.*, 7(1), 1–12.
- Lei, X., Ma, S., Chen, W., Pang, C., Zeng, J., and Jiang, B. (2013). A Detailed View of the Injection-Induced Seismicity in a Natural Gas Reservoir in Zigong, Southwestern Sichuan Basin, China. *J. Geophys. Res. Solid Earth*, 118(8), 4296–4311.
- Lei, X., Wang, Z., and Su, J. (2019). The December 2018 ML 5.7 and January 2019 ML 5.3 Earthquakes in South Sichuan Basin Induced by Shale Gas Hydraulic Fracturing. *Seismol. Res. Lett.*, 90(3), 1099–1110.
- Lin, Y. Y., and Lapusta, N. (2018). Microseismicity Simulated on Asperity-Like Fault Patches: On Scaling of Seismic Moment With Duration and Seismological Estimates of Stress Drops. *Geophys. Res. Lett.*, 45(16), 8145–8155.
- Long, L. T. (2019). The Mechanics of Natural and Induced Shallow Seismicity: A Review and Speculation Based on Studies of Eastern U.S. Earthquakes. *Bull. Seismol. Soc. Am.*, 109(1), 336–347.
- López-Comino, J. A., and Cesca, S. (2018). Source Complexity of an Injection Induced Event: The 2016 Mw 5.1 Fairview, Oklahoma Earthquake. *Geophys. Res. Lett.*, 45(9), 4025–4032.
- Lui, S. K. Y., and Huang, Y. (2019). Do Injection-Induced Earthquakes Rupture Away

- from Injection Wells Due to Fluid Pressure Change? *Bull. Seismol. Soc. Am.*, 109(1), 358–371.
- Madariaga, R. (1976). Dynamics of an Expanding Circular Fault. *Bull. Seismol. Soc. Am.*, 66(3), 639–666.
- Madariaga, R. (1989). Seismic Source: Theory. In *Geophysics* (pp. 1129–1133). Boston, MA: Springer US.
- Mahani, A. B., Kao, H., Atkinson, G. M., Assatourians, K., Addo, K., and Liu, Y. (2019). Ground-Motion Characteristics of the 30 November 2018 Injection-Induced Earthquake Sequence in Northeast British Columbia, Canada. *Seismol. Res. Lett.*, 1457–1467.
- Mahani, A. B., Schultz, R., Kao, H., Walker, D., Johnson, J., and Salas, C. J. (2017). Fluid Injection and Seismic Activity in the Northern Montney Play, British Columbia, Canada, with Special Reference to the 17 August 2015 Mw 4.6 Induced Earthquake. *Bull. Seismol. Soc. Am.*, 107(2), 542–552.
- Mayeda, K., Malagnini, L., and Walter, W. R. (2007). A New Spectral Ratio Method Using Narrow Band Coda Envelopes: Evidence for Non-Self-Similarity in the Hector Mine Sequence. *Geophys. Res. Lett.*, 34(11), 1–5.
- McGarr, A. F., Simpson, D., and Seeber, L. (1994). Case Histories of Induced and Triggered Seismicity. In *International Handbook of Earthquake and Engineering Seismology* (pp. 647–661).
- McGuire, J. J., and Kaneko, Y. (2018). Directly Estimating Earthquake Rupture Area Using Second Moments to Reduce the Uncertainty in Stress Drop. *Geophys. J. Int.*, 214(3), 2224–2235.
- Montgomery, C. T., and Smith, M. B. (2010). Hydraulic Fracturing: History of an Enduring Technology. *J. Pet. Technol.*, 62(15), 26–40.
- Mori, J., and Frankel, A. (1990). Source Parameters for Small Events Associated With the 1986 North Palm Springs, California, Earthquake Determined Using Empirical Green Functions. *Bull. Seismol. Soc. Am.*, 80(2), 278–295.

- Moschetti, M. P., Hartzell, S. H., and Herrmann, R. B. (2019). Rupture Model of the M5.8 Pawnee, Oklahoma, Earthquake From Regional and Teleseismic Waveforms. *Geophys. Res. Lett.*, 46(5), 2494–2502.
- Moss, R. E. S. (2011). Reduced Sigma of Ground-Motion Prediction Equations through Uncertainty Propagation. *Bull. Seismol. Soc. Am.*, 101(1), 250–257.
- Mueller, C. S. (1985). Source Pulse Enhancement by Deconvolution of an Empirical Green's Function. *Geophys. Res. Lett.*, 12(1), 33–36.
- Nigam, N. C., and Jennings, P. C. (1969). Calculation of Response Spectra from Strong-Motion Earthquake Records. *Bull. Seismol. Soc. Am.*, 59(2), 909–922.
- Novakovic, M., and Atkinson, G. M. (2015). Preliminary Evaluation of Ground Motions from Earthquakes in Alberta. *Seismol. Res. Lett.*, 86(4), 1086–1095.
- Novakovic, M., Atkinson, G. M., and Assatourians, K. (2018). Empirically Calibrated Ground-Motion Prediction Equation for Oklahoma. *Bull. Seismol. Soc. Am.*, 108(5), 2444–2461.
- Novakovic, M., Atkinson, G. M., Assatourians, K., and Gu, Y. J. (2019). Empirical Characterization of Ground Motions for Induced Seismicity in Alberta. *12th Canadian Conference on Earthquake Engineering*. Quebec City.
- Onwuemeka, J., Liu, Y., and Harrington, R. M. (2018). Earthquake Stress Drop in the Charlevoix Seismic Zone, Eastern Canada. *Geophys. Res. Lett.*, 45(22), 12,226–12,235.
- Oth, A. P. H., Bindi, D., Parolai, S., and Di Giacomo, D. (2010). Earthquake Scaling Characteristics and the Scale-(in)Dependence of Seismic Energy-to-Moment Ratio: Insights from KiK-Net Data in Japan. *Geophys. Res. Lett.*, 37(19), 1–5.
- Oth, A. P. H., Miyake, H., and Bindi, D. (2017). On the Relation of Earthquake Stress Drop and Ground Motion Variability. *J. Geophys. Res. Solid Earth*, 122(7), 5474–5492.
- Park, S., and Ishii, M. (2015). Inversion for Rupture Properties Based upon 3-D Directivity Effect and Application to Deep Earthquakes in the Sea of Okhotsk Region. *Geophys. J. Int.*, 203(2), 1011–1025.

- Petersen, M. D., Mueller, C. S., Moschetti, M. P., Hoover, S. M., Llenos, A. L., Ellsworth, W. L., ... Rukstales, K. S. (2016). 2016 One-Year Seismic Hazard Forecast for the Central and Eastern United States from Induced and Natural Earthquakes. *USGS Open File Rep.*
- Petersen, M. D., Mueller, C. S., Moschetti, M. P., Hoover, S. M., Shumway, A. M., McNamara, D. E., ... Rukstales, K. S. (2017). 2017 One-Year Seismic-Hazard Forecast for the Central and Eastern United States from Induced and Natural Earthquakes. *Seismol. Res. Lett.*, 88(3), 772–783.
- Pezeshk, S., Zandieh, A., Campbell, K. W., and Tavakoli, B. (2018). Ground-Motion Prediction Equations for Central and Eastern North America Using the Hybrid Empirical Method and NGA-West2 Empirical Ground-Motion Models. *Bull. Seismol. Soc. Am.*, 108(4), 2278–2304.
- Pezeshk, S., Zandieh, A., and Tavakoli, B. (2011). Hybrid Empirical Ground-Motion Prediction Equations for Eastern North America Using NGA Models and Updated Seismological Parameters. *Bull. Seismol. Soc. Am.*, 101(4), 1859–1870.
- Porter, J. W., Price, R. A., and McCrossan, R. G. (1982). The Western Canada Sedimentary Basin. *Philos. Trans. R. Soc. A Math. Phys. Eng. Sci.*, 305(1489), 169–192.
- Prieto, G. A., Parker, R. L., and Vernon, F. L. (2009). A Fortran 90 Library for Multitaper Spectrum Analysis. *Comput. Geosci.*, 35(8), 1701–1710.
- Reiter, K., Heidbach, O., Schmitt, D., Haug, K., Ziegler, M., and Moeck, I. (2014). A Revised Crustal Stress Orientation Database for Canada. *Tectonophysics*, 636, 111–124.
- Rhoades, D. A. (1997). Estimation of Attenuation Relations for Strong-Motion Data Allowing for Individual Earthquake Magnitude Uncertainties. *Bull. Seismol. Soc. Am.*, 87(6), 1674–1678.
- Richter, C. F. (1935). An Instrumental Earthquake Magnitude Scale. *Bull. Seismol. Soc. Am.*, 25(1), 1–32.
- Ristau, J., Rogers, G. C., and Cassidy, J. F. (2007). Stress in Western Canada from Regional Moment Tensor Analysis. *Can. J. Earth Sci.*, 44(2), 127–148.

- Rivard, C., Lavoie, D., Lefebvre, R., Séjourné, S., Lamontagne, C., and Duchesne, M. (2014). An Overview of Canadian Shale Gas Production and Environmental Concerns. *Int. J. Coal Geol.*, 126, 64–76.
- Rodríguez-Pérez, Q., and Singh, S. K. (2016). Seismic Source Parameters of Normal-Faulting Inslab Earthquakes in Central Mexico. *Pure Appl. Geophys.*, 173(8), 2587–2619.
- Rubinstein, J. L., and Mahani, A. B. (2015). Myths and Facts on Wastewater Injection, Hydraulic Fracturing, Enhanced Oil Recovery, and Induced Seismicity. *Seismol. Res. Lett.*, 86(4), 1060–1067.
- Ruhl, C. J., Abercrombie, R. E., and Smith, K. D. (2017). Spatiotemporal Variation of Stress Drop During the 2008 Mogul, Nevada, Earthquake Swarm. *J. Geophys. Res. Solid Earth*, 122(10), 8163–8180.
- Sato, T., and Hirasawa, T. (1973). Body Wave Spectra from Propagating Shear Cracks. *J. Phys. Earth*, 21(4), 415–431.
- Savage, J. C., and Wood, M. D. (1971). The Relation between Apparent Stress and Stress Drop. *Bull. Seismol. Soc. Am.*, 61(5), 1381–1388.
- Schultz, R., Stern, V., and Gu, Y. J. (2014). An Investigation of Seismicity Clustered near the Cordell Field, West Central Alberta, and Its Relation to a Nearby Disposal Well. *J. Geophys. Res. Solid Earth*, 119, 3410–3423.
- Schultz, R., Wang, R., Gu, Y. J., Haug, K., and Atkinson, G. M. (2017). A Seismological Overview of the Induced Earthquakes in the Duvernay Play near Fox Creek, Alberta. *J. Geophys. Res. Solid Earth*, 122(1), 492–505.
- Seekins, L. C., and Boatwright, J. (2010). Rupture Directivity of Moderate Earthquakes in Northern California. *Bull. Seismol. Soc. Am.*, 100(3), 1107–1119.
- Shearer, P. M., Abercrombie, R. E., Trugman, D. T., and Wang, W. (2019). Comparing EGF Methods for Estimating Corner Frequency and Stress Drop From P Wave Spectra. *J. Geophys. Res. Solid Earth*, 124(4), 3966–3986.
- Shipman, T., MacDonald, R., and Byrnes, T. (2018). Experiences and Learnings from

- Induced Seismicity Regulation in Alberta. *Interpretation*, 6(2), SE15–SE21.
- Sibson, R. H. (1985). A Note on Fault Reactivation. *J. Struct. Geol.*, 7(6), 751–754.
- Somerville, P. G., Smith, N. F., Graves, R. W., and Abrahamson, N. A. (1997). Modification of Empirical Strong Ground Motion Attenuation Relations to Include the Amplitude and Duration Effects of Rupture Directivity. *Seismol. Res. Lett.*, 68(1), 199–222.
- Spudich, P., and Chiou, B. S. J. (2008). Directivity in NGA Earthquake Ground Motions: Analysis Using Isochrone Theory. *Earthq. Spectra*, 24(1), 279–298.
- Spudich, P., Rowshandel, B., Shahi, S. K., Baker, J. W., and Chiou, B. S. J. (2014). Comparison of NGA-West2 Directivity Models. *Earthq. Spectra*, 30(3), 1199–1221.
- Stern, V., Schultz, R., Shen, L., Gu, Y. J., and Eaton, D. W. (2018). *Alberta earthquake catalogue, version 6.0 (GIS data, point features)*. Alberta Energy Regulator, AER/AGS Digital Dataset 2013–0017.
- Strasser, F. O., Abrahamson, N. A., and Bommer, J. J. (2009). Sigma: Issues, Insights, and Challenges. *Seismol. Res. Lett.*, 80(1), 40–56.
- Student. (1908). The Probable Error of a Mean. *Biometrika*, 1–25.
- Sumy, D. F., Neighbors, C. J., Cochran, E. S., and Keranen, K. M. (2017). Low Stress Drops Observed for Aftershocks of the 2011 Mw 5.7 Prague, Oklahoma, Earthquake. *J. Geophys. Res. Solid Earth*, 122(5), 3813–3834.
- Taira, T., Dreger, D. S., and Nadeau, R. M. (2015). Rupture Process for Micro-Earthquakes Inferred from Borehole Seismic Recordings. *Int. J. Earth Sci.*, 104(6), 1499–1510.
- Tomic, J., Abercrombie, R. E., and do Nascimento, A. F. (2009). Source Parameters and Rupture Velocity of Small $M \leq 2.1$ Reservoir Induced Earthquakes. *Geophys. J. Int.*, 179(2), 1013–1023.
- Toro, G. R., and McGuire, R. K. (1987). An Investigation into Earthquake Ground Motion Characteristics in Eastern North America. *Bull. Seismol. Soc. Am.*, 77(2), 468–489.
- Trugman, D. T., and Shearer, P. M. (2017). Application of an Improved Spectral Decomposition Method to Examine Earthquake Source Scaling in Southern

- California. *J. Geophys. Res. Solid Earth*, 122(4), 2890–2910.
- Uchide, T., and Imanishi, K. (2016). Small Earthquakes Deviate from the Omega-Square Model as Revealed by Multiple Spectral Ratio Analysis. *Bull. Seismol. Soc. Am.*, 106(3), 1357–1363.
- Van Houtte, C., and Denolle, M. A. (2018). Improved Model Fitting for the Empirical Green's Function Approach Using Hierarchical Models. *J. Geophys. Res. Solid Earth*, 123(4), 2923–2942.
- Van Houtte, C., Drouet, S., and Cotton, F. (2011). Analysis of the Origins of κ (Kappa) to Compute Hard Rock to Rock Adjustment Factors for GMPEs. *Bull. Seismol. Soc. Am.*, 101(6), 2926–2941.
- Van Houtte, C., Larkin, T., and Holden, C. (2018). On Durations, Peak Factors, and Nonstationarity Corrections in Seismic Hazard Applications of Random Vibration Theory. *Bull. Seismol. Soc. Am.*, 108(1), 418–436.
- Vanmarcke, E. H., and Lai, S.-S. P. (1980). Strong-Motion Duration and RMS Amplitude of Earthquake Records. *Bull. Seismol. Soc. Am.*, 70(4), 1293–1307.
- Velasco, A. A., Ammon, C. J., and Lay, T. (1994). Empirical Green Function Deconvolution of Broadband Surface Waves: Rupture Directivity of the 1992 Landers, California (Mw= 7.3), Earthquake. *Bull. Seismol. Soc. Am.*, 84(3), 735–750.
- Viegas, G., Abercrombie, R. E., and Kim, W.-Y. (2010). The 2002 M5 Au Sable Forks, NY, Earthquake Sequence: Source Scaling Relationships and Energy Budget. *J. Geophys. Res. Solid Earth*, 115(7), 1–20.
- Visser, R., Smith, B., Kao, H., Mahani, A. B., Hutchinson, J., and McKay, J. E. (2017). A Comprehensive Earthquake Catalogue for Northeastern British Columbia and Western Alberta, 2014-2016. In *Geological Survey of Canada, Open File*.
- Wang, H., Wen, R., and Ren, Y. (2017). Simulating Ground-Motion Directivity Using Stochastic Empirical Green's Function Method. *Bull. Seismol. Soc. Am.*, 107(1), 359–371.
- Wang, R., Gu, Y. J., Schultz, R., and Chen, Y. (2018). Faults and Non-Double-Couple

- Components for Induced Earthquakes. *Geophys. Res. Lett.*, 45(17), 8966–8975.
- Wang, R., Gu, Y. J., Schultz, R., Zhang, M., and Kim, A. (2017). Source Characteristics and Geological Implications of the January 2016 Induced Earthquake Swarm near Crooked Lake, Alberta. *Geophys. J. Int.*, 210(2), 979–988.
- Wilson, M. P., Davies, R. J., Foulger, G. R., Julian, B. R., Styles, P., Gluyas, J. G., and Almond, S. (2015). Anthropogenic Earthquakes in the UK: A National Baseline Prior to Shale Exploitation. *Mar. Pet. Geol.*, 68, 1–17.
- Wu, Q., and Chapman, M. (2017). Stress-Drop Estimates and Source Scaling of the 2011 Mineral, Virginia, Mainshock and Aftershocks. *Bull. Seismol. Soc. Am.*, 107(6), 2703–2720.
- Wu, Q., Chapman, M., and Chen, X. (2018). Stress-Drop Variations of Induced Earthquakes in Oklahoma. *Bull. Seismol. Soc. Am.*, 108(3), 1107–1123.
- Yenier, E., and Atkinson, G. M. (2015a). An Equivalent Point-Source Model for Stochastic Simulation of Earthquake Ground Motions in California. *Bull. Seismol. Soc. Am.*, 105(3), 1435–1455.
- Yenier, E., and Atkinson, G. M. (2015b). Regionally Adjustable Generic Ground-Motion Prediction Equation Based on Equivalent Point-Source Simulations: Application to Central and Eastern North America. *Bull. Seismol. Soc. Am.*, 105(4), 1989–2009.
- Yong, A., Thompson, E. M., Wald, D., Knudsen, K. L., Odum, J. K., Stephenson, W. J., and Haefner, S. (2016). Compilation of VS30 Data for the United States: U.S. Geological Survey Data Series 978.
- Yoshimitsu, N., Ellsworth, W. L., and Beroza, G. C. (2019). Robust Stress Drop Estimates of Potentially Induced Earthquakes in Oklahoma: Evaluation of Empirical Green's Function. *J. Geophys. Res. Solid Earth*, 124, 1–13.
- Youngs, R. R., Abrahamson, N. A., Makdisi, F. I., and Sadigh, K. (1995). Magnitude-Dependent Variance of Peak Ground Acceleration. *Bull. Seismol. Soc. Am.*, 85(4), 1161–1176.
- Zafarani, H., Rahpeyma, S., and Mousavi, M. (2017). Regional Adjustment Factors for

Three NGA-West2 Ground-Motion Prediction Equations to Be Applicable in Northern Iran. *J. Seismol.*, 21(3), 473–493.

Zhang, H., Eaton, D. W., Li, G., Liu, Y., and Harrington, R. M. (2016). Discriminating Induced Seismicity from Natural Earthquakes Using Moment Tensors and Source Spectra. *J. Geophys. Res. Solid Earth*, 121, 972–993.

Zhang, H., Eaton, D. W., Rodriguez, G., and Jia, S. Q. (2019). Source-Mechanism Analysis and Stress Inversion for Hydraulic- Fracturing-Induced Event Sequences near Fox Creek, Alberta. *Bull. Seismol. Soc. Am.*, 109(2), 636–651.

Appendices

Table A2.1. Initial and final variability terms for each PSA (5% damped) frequency and peak ground acceleration (PGA) and peak ground velocity (PGV), for all records within 70 and 10 km, for the vertical component.

PSA	0.5 Hz	1 Hz	3.3 Hz	10 Hz	PGA	PGV	Average
Vertical Component							
<i>R_{hypo}</i> ≤ 70 km (initial)							
Total Sigma	0.406	0.394	0.360	0.403	0.399	0.374	0.389
Between-event	0.316	0.305	0.287	0.315	0.311	0.285	0.303
Within-event	0.256	0.249	0.217	0.251	0.251	0.243	0.244
<i>R_{hypo}</i> ≤ 70 km (final)							
Total Sigma	0.285	0.256	0.210	0.239	0.253	0.217	0.243
Between-event	0.154	0.135	0.092	0.107	0.131	0.094	0.119
Within-event	0.240	0.218	0.189	0.214	0.217	0.196	0.212
<i>R_{hypo}</i> ≤ 10 km (initial)							
Total Sigma	0.456	0.423	0.412	0.474	0.466	0.433	0.444
Between-event	0.385	0.351	0.364	0.415	0.416	0.375	0.384
Within-event	0.245	0.236	0.192	0.228	0.209	0.217	0.221
<i>R_{hypo}</i> ≤ 10 km (final)							
Total Sigma	0.322	0.276	0.237	0.254	0.313	0.263	0.277
Between-event	0.224	0.182	0.169	0.181	0.269	0.200	0.204
Within-event	0.232	0.207	0.166	0.177	0.160	0.171	0.185

Table A2.2. Initial and final variability terms for each PSA (5% damped) frequency and peak ground acceleration (PGA) and peak ground velocity (PGV), for all records within 70 and 10 km, for the geometric mean of the horizontal components.

PSA	0.5 Hz	1 Hz	3.3 Hz	10 Hz	PGA	PGV	Average
Horizontal Component							
$R_{hypo} \leq 70$ km (initial)							
Total Sigma	0.422	0.374	0.368	0.379	0.375	0.373	0.382
Between-event	0.309	0.301	0.275	0.292	0.290	0.283	0.292
Within-event	0.288	0.222	0.244	0.242	0.237	0.244	0.246
$R_{hypo} \leq 70$ km (final)							
Total Sigma	0.321	0.271	0.273	0.277	0.278	0.275	0.283
Between-event	0.161	0.171	0.138	0.151	0.134	0.143	0.150
Within-event	0.278	0.211	0.235	0.232	0.244	0.234	0.239
$R_{hypo} \leq 10$ km (initial)							
Total Sigma	0.470	0.413	0.418	0.445	0.433	0.417	0.433
Between-event	0.311	0.347	0.362	0.379	0.372	0.366	0.356
Within-event	0.352	0.225	0.209	0.234	0.222	0.199	0.240
$R_{hypo} \leq 10$ km (final)							
Total Sigma	0.410	0.334	0.306	0.345	0.364	0.324	0.347
Between-event	0.247	0.267	0.246	0.264	0.299	0.266	0.265
Within-event	0.328	0.201	0.181	0.223	0.206	0.185	0.221

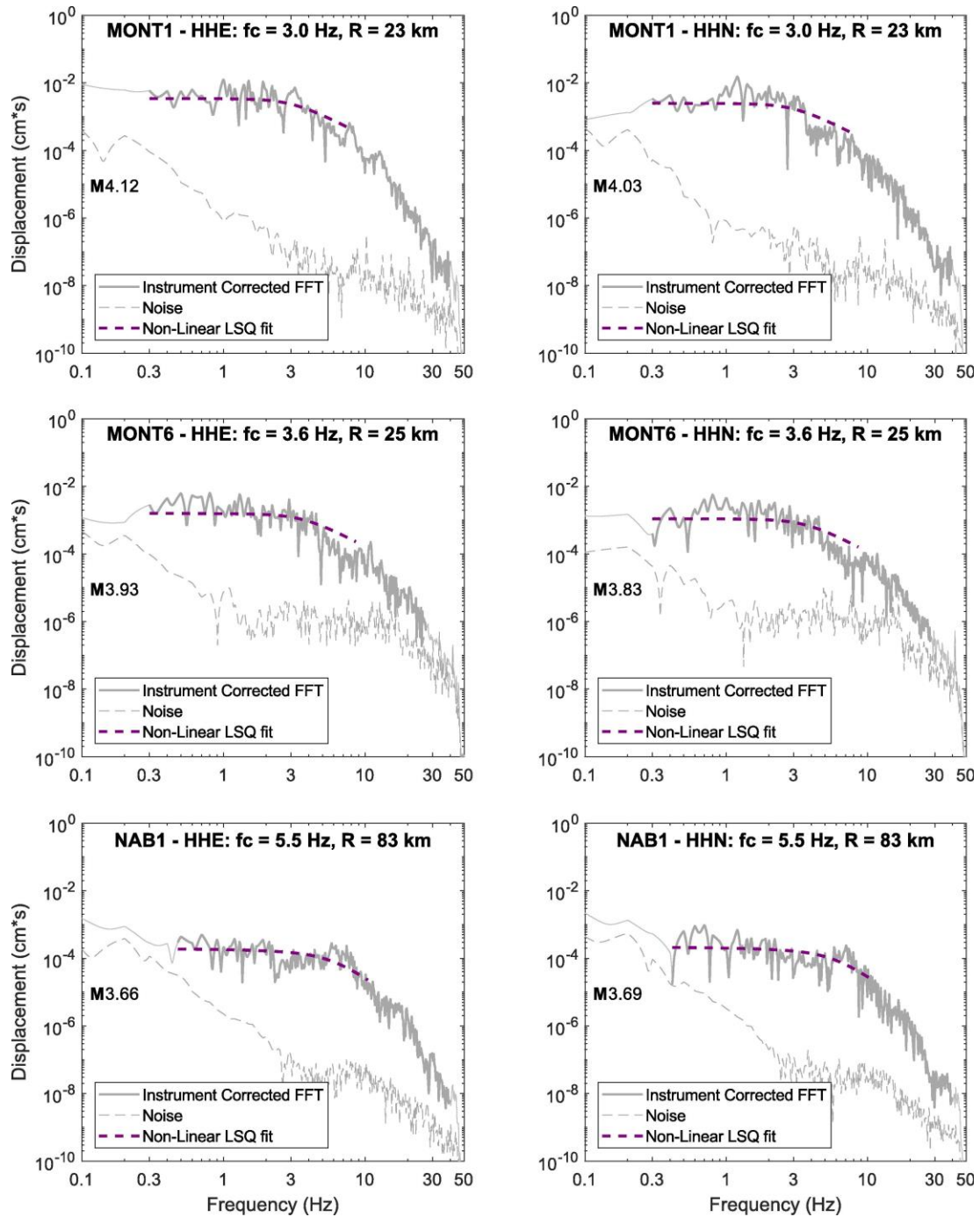


Figure A3.1. Magnitude computation example of target event #114 **M 3.81** 2018-11-30 02:15:01 and three of its stations within 100 km. The left column shows HHE components, and the right shows HHN components. Signal (solid line), noise (light dashed line), and low-frequency best fit of Equation (3.5) (dark dashed line) are shown for each station and component. The bold spectra lines represent frequency range over which $\text{SNR} > 3$.

Table A4.1. The generic GMPE components.

Component	Functional Form	Parameters and References
Magnitude Effect, F_M	$F_M = \begin{cases} e_0 + e_1(\mathbf{M} - \mathbf{M}_h) + e_2(\mathbf{M} - \mathbf{M}_h)^2, & \mathbf{M} \leq \mathbf{M}_h \\ e_0 + e_3(\mathbf{M} - \mathbf{M}_h), & \mathbf{M} > \mathbf{M}_h \end{cases}$	<p>\mathbf{M} – moment magnitude</p> <p>\mathbf{M}_h – hinge magnitude (YA15b*)</p> <p>e_{0-3} – frequency dependent coefficients (YA15b*)</p>
Stress Adjustment, $F_{\Delta\sigma}$	$F_{\Delta\sigma} = e_{\Delta\sigma} \ln\left(\frac{\Delta\sigma_{par}}{100}\right)$ $e_{\Delta\sigma} = \begin{cases} s_0 + s_1\mathbf{M} + s_2\mathbf{M}^2 + s_3\mathbf{M}^3 + s_4\mathbf{M}^4, & \Delta\sigma_{par} \leq 100 \text{ bars} \\ s_5 + s_6\mathbf{M} + s_7\mathbf{M}^2 + s_8\mathbf{M}^3 + s_9\mathbf{M}^4, & \Delta\sigma_{par} > 100 \text{ bars} \end{cases}$ $\Delta\sigma_{par} = \exp[\min(2.45\mathbf{M} - 4.71, 4.37)], \quad 2 \leq \mathbf{M} \leq 4.5$	<p>$\Delta\sigma_{par}$ – stress parameter model (bars)</p> <p>$e_{\Delta\sigma}$ – rate of ground-motion scaling (YA15b*)</p> <p>s_{0-9} – frequency dependent coefficients (YA15b*)</p> <p>d – depth (km)</p>

* YA15b: Yenier and Atkinson (2015b)

Table A4.1. (cont'd)

Component	Functional Form	Parameters and References
Geometrical Spreading, F_Z	$F_Z = \ln(Z) + (b_4 + b_5 \mathbf{M}) \ln(R/R_{ref})$ $R = \sqrt{D_{rup}^2 + h^2}$ $R_{ref} = \sqrt{1 + h^2}$ $h = 10^{-0.405 + 0.235 \mathbf{M}}$ $Z = \begin{cases} R^{b_1} & R \leq 80 \text{ km} \\ 80^{b_1} \left(\frac{R}{80}\right)^{b_2} & 80 \text{ km} < R \leq 160 \text{ km} \\ 80^{b_1} \left(\frac{160}{80}\right)^{b_2} \left(\frac{R}{160}\right)^{b_3} & R > 160 \text{ km} \end{cases}$	<p>Z – geometrical spreading function</p> <p>b_{1-3} – geometrical spreading rates (NAAG19*)</p> <p>b_{4-5} – frequency dependent coefficients relating Fourier and response domains (YA15b*)</p> <p>R – effective distance (km)</p> <p>D_{rup} – closest distance to rupture (km)</p> <p>h – pseudodepth term (km)</p> <p>R_{ref} – reference effective distance (km)</p>
Anelastic Attenuation, F_γ	$F_\gamma = \gamma D_{rup}$	<p>γ – frequency dependent anelastic attenuation (NAAG19*)</p>

* YA15b: Yenier and Atkinson (2015b); NAAG19: Novakovic et al. (2019)

Electronic Supplement Description

The electronic supplement of this thesis contains five tables, described below:

Table S3.1. Parameters of the earthquakes studied in Chapter 3. The following columns are given: Earthquake ID number, origin time (yyyymmdd_HHMMSS), earthquake latitude (degrees), earthquake longitude (degrees), earthquake depth from original catalog (km), moment magnitude computed from the displacement spectrum, standard deviation of moment magnitudes from all stations used for each target earthquake, number of stations used for the target earthquake, number of target-EGF earthquake pairs in the final stack, target earthquake corner frequency (Hz), corner frequency error (Hz), earthquake stress drop (MPa), stress drop error (MPa), directivity index assigned to target earthquake (0 = unknown directivity; 1 = yes directivity; 2 = no directivity), rupture azimuth for target earthquakes with directivity observed (degrees), and complexity index (0 = no source complexity is observed; 1 = complexity is observed).

Table S4.1. Earthquake-specific information and corner frequency results for earthquakes studied in Chapter 4. The following columns are given: Event id, origin times (yyyymmdd_HHMMSS), earthquake latitude and longitude (degrees), moment magnitude, corner frequency (f_c) from the Holmgren et al. (2019) Empirical Green's Function (EGF) study (Hz), EGF $f_c \pm$ error (Hz), f_c using the GMPE method (Hz), negative GMPE f_c error (Hz), positive GMPE f_c error (Hz).

Table S4.2. PSA flatfiles for records used in Chapter 4. The following columns are given: Individual earthquake records' event id (referring to Table S4.1), station, moment magnitude, hypocentral distance (km), PSA at selected frequencies (cm/s^2), PGA (cm/s^2), and PGV (cm/s).

Table S4.3. Model coefficients of the WCSB GMPE used in Chapter 4, and whose equations are given in Table A4.1, given for geomean horizontal, 5% damped PSA reported at selected frequencies (natural logarithm cm/s^2), PGA (natural logarithm cm/s^2), and PGV

(natural logarithm cm/s). The following columns are given: Hinge magnitude (M_h), frequency dependent magnitude effect coefficients (e_0 - e_3), stress adjustment terms (s_0 - s_9), coefficients relating Fourier and response domain (b_4 - b_5), WCSB anelastic attenuation factor (γ), and the WCSB regional calibration factor (C) are given.

Table S4.4. Individual station terms to the WCSB GMPE. The following columns are given: Station name, station latitude and longitude (degrees), and station terms at selected frequencies, PGA and PGV (reported in natural logarithmic units).

Curriculum Vitae

Name: Joanna Holmgren

Post-secondary Education and Degrees: Luleå University of Technology
Luleå, Sweden
2009-2013 B.Sc.

Uppsala University
Uppsala, Sweden
2013-2015 M.Sc.

The University of Western Ontario
London, Ontario, Canada
2016-2020 Ph.D.

Honors and Awards: Faculty of Science Graduate Teaching Award
2019

Western University Robert B. Hodder Travel Bursary
2018

Western Graduate Research Scholarship (WGRS)
2016-2018

Related Work Experience Teaching Assistant
The University of Western Ontario
2016-2019

Research Assistant
The University of Western Ontario
2016-2019

Publications:

Holmgren J., Atkinson G., Ghofrani H., (2020). Reconciling Ground Motions and Stress Drops for Induced Earthquakes in the Western Canada Sedimentary Basin. *Bull. Seismol. Soc. Am.* (accepted)

Holmgren J., Atkinson G., Ghofrani H., (2019). Stress Drops and Directivity of Induced Earthquakes in the Western Canada Sedimentary Basin. *Bull. Seimol. Soc. Am.* 109(5): 1635-1652.

Holmgren J., Atkinson G. (2018). Effect of Uncertainty in Source Parameters on Ground-Motion Variability for Potentially Induced Earthquakes in the Central United States. *Seimol. Res. Lett.* 89(2A): 702-711.

Conference Proceedings:

SSA Seattle 2019, **Holmgren J.**, Atkinson G., Ghofrani H., Stress Drops and Directivity of Induced Earthquakes in Western Canada Sedimentary Basin, Poster presentation.

Banff Induced Seismicity Workshop 2018, **Holmgren J.**, Atkinson G., Ghofrani H., Stress Drops of Induced Earthquakes in the Western Canada Sedimentary Basin, Poster presentation.

CGU Niagara Falls 2018, **Holmgren J.**, Atkinson G., Ghofrani H., Stress Drop Investigation of Induced Earthquakes in Alberta using Empirical Green's Function Method, Oral presentation.

SSA Miami 2018, **Holmgren J.**, Atkinson G., Ghofrani H., Stress Drop Investigation of $M > 4$ Induced Earthquakes in Western Canada Using Empirical Green's Function Method, Poster presentation.

SSA Denver 2017, **Holmgren J.**, Atkinson G., The Contribution of Uncertainty in Magnitude and Location to Near-Distance Variability in Ground Motions for Potentially-Induced Earthquakes in Oklahoma, Poster presentation.